Theory of Electron Transport through a Single Molecule

Hanan Althobaiti

PhD Thesis in Physics

Department of physics, Lancaster University, UK

This Thesis is submitted in partial fulfilment of the requirements for degree of Doctor of Philosophy

2022

Declaration

I hereby declare that the thesis is my own work and effort and has not been submitted in substantially the same form for the award of a higher degree elsewhere. Other sources of information have been used, they have been acknowledged. This thesis documents work carried out between November 2019 and July 2022 at Lancaster University, UK, under the supervision of Prof. Colin J. Lambert and funded by Ministry of Higher Education Saudi Arabia and Taif University, KSA.

Hanan Althobaiti

2022

Acknowledgment

I would like to express deepest gratitude to Prof. Colin John Lambert who always put his students interests first. His kindness, patience and support are incredible. I am so grateful to have worked with such great physicist and human being. Also, many thanks to Theory of molecular-Scale groups especially Dr. Turki Alotaibi and Dr. Majed Alshammary.

Many thanks also go to the support I received during my PhD from the ministry of higher education in Saudi Arabia and Taif University.

I would like to thank the collaborating experimental groups. I also would like to thank all my friends and colleagues in Colin's group.

I would like to express a deep sense of gratitude to my loved parents, words are insufficient to express all my gratitude to them for their endless love--, care, support, encouragement and understanding. Also, I would like to give very special thanks to my husband (Awwadh) for his patience, tolerance, care and love for me. I am also grateful to my daughter (Lateen). My gratitude to her is beyond words.

Last but not the least, my warm thanks also go to my sister, my brothers and other family members for supporting me spiritually and virtually to follow my dream of getting this degree. Above all, my great thanks to ALLAH for his mercy and blessing.

Abstract

Understanding the orbital alignment of molecules sandwiched between metal electrodes is essential in the design of applicable molecular electronic devices. Orbital alignment is determined both by the molecular backbone structure and the molecule-electrode interface. This thesis presents a series of studies into the electronic and thermoelectric properties of 6 oligo (phenylene-ethynylene) OPE-based molecules trapped between the single-layer graphene (SLG) and a gold electrode to form an asymmetric junction. This study also employs 4 different anchor groups including thiol, pyridine, thioacetate and thioether.

In the first part of this thesis, the theoretical tools, employed to investigate electron-transport properties of molecular junctions, are described. In chapter 2, Density Functional Theory (DFT), which is implemented in the SIESTA code, will be discussed. This provides the ground state wave functions for molecules and the Hamiltonians for molecular junctions, which is the first step in the transport calculations. Chapter 3 presents the theoretical basis for calculating the electric and thermoelectric properties, based on the Green's function formalism, which is implemented in the quantum transport code GOLLUM. In chapter 3, I present solutions of Green's functions for infinite and semi-infinite chains and the transmission coefficient equation, which forms the theoretical basis of this code.

Chapter 4 is the first results chapter in this thesis, which demonstrates the transport properties of the six types of asymmetric junction modelled using a combination of density-functional theory and quantum transport theory. In this study, through a combined experimental and theoretical study, I show that the control of orbital alignment can be achieved by applying an external gate to six types of OPE-based molecules, which in turn control the electron transport within the HOMO-LUMO energy gap. I also demonstrate that the shape of the gold electrode (i.e., flat versus cluster) may affect the alignment of the HOMO and LUMO levels of the

junction with respect to the Fermi level of the electrodes. Atheoretical investigation into the Seebeck coefficient is performed in chapter 5 using the first principles quantum transport method. This is carried out for six OPE-based molecules with two different gold electrode geometries (i.e., flat and cluster).

List of Publications

1. Xintai Wang, **Hanan Althobaiti**, Shanglong Ning, Alaa Al-Jobory, Jan Girovsky, Hippolyte P.A.G. Astier, Luke J. O'Driscoll, Martin R. Bryce, Colin J. Lambert and Christopher J. B. Ford. Tuning Fermi Level Alignment In Large Scale Self-Assembled Oligo (phenylene-ethynylene) Derivatives. (*Submitted).*

In this paper, I modelled six types of asymmetric three-terminal junctions in which the top contact is single-layer graphene (SLG), divided into two electrodes (electrode 1 and electrode 2), whereas the bottom contact is Au (electrode 3). I calculated the binding energies as a function of distance between the contacts (i.e., Au and SLG) and the different anchor groups such as methyl sulfide (SMe), pyridyl (Py) and thiol (-SH), using the counterpoise method. I also studied the charge transport behaviour using a combination of density-functional theory and quantum transport theory for two different configurations of the gold electrode (i.e., flat surface and cluster). Furthermore, I investigated the Seebeck using the first principles quantum transport method. This is carried out for six OPE-based molecules with two different gold electrode geometries (i.e., flat and cluster).

2. Zhixin Chen, Maryam Alshahrani, Yaorong Chen, Lina Chen, **Hanan Althobaiti,** James O. Thomas, Zhiyu Zhu, Haiping, Xia, Colin Lambert and Wenjing. Hong Highly Conductive Single-molecule Junctions with Double N-Hetercyclic Carbene Anchors. (*Submitted).*

In this work, the single-molecule conductance of a series of air-stable N-heterocyclic carbene (NHC) compounds combining group IB metal (Cu, Ag, Au) with double NHC ligands and dibenzofulvene backbone is investigated. My contribution is to calculate the optimum binding distances between the electrodes and the different anchor groups using the counterpoise method. These molecules have several possible binding sites and therefore I scanned the whole molecule in 3D with a gold tip to find the strongest-binding contact points.

Table of contents

Chapter 1 24

1.1 Molecular electronics 24

1.2 Thesis Outline 28

1.3 Bibliography 31

Chapter 2 36

2. Density Functional Theory 36

2.1 Introduction 36

2.2 Many-body problem 37

2.3. Born- Oppenheimer approximation 38

2.4 The Hohenberg- Kohn theorem 39

2.5 The Kohn-Sham theorem 41

2.6 The Exchange Correlation functional 43

2.6.1 Local Density Approximation 43

2.6.2 Generalized Gradient Approximation 44

2.7 SIESTA 45

2.7.1 The Pseudopotential Approximation 45

2.7.2 SIESTA Basis Sets 46

2.7.3 Calculating binding energy using the counterpoise method 47

2.8 Calculation in Practice 48

2.9 Conclusion 50

2.10 Bibliography 51

Chapter 3 55

3. Theory of single particle transport 55

3.1 Introduction 55

3.2 Tight-binding model 56

3.2 One-dimensional (1-D) linear infinite chain 57

3.3 One-Dimensional Scattering Theory 59

3.3.1 Bond currents and conservation of probability 59

3.3.2 Transport for crystalline chain with a single impurity 62

3.4 The Landauer Formula 65

3.5 Green's Functions 68

3.5.1 Green's function of a doubly infinite chain 68

3.5.2 Green's function of a semi-infinite linear chain 71

3.5.3 Green's function of a finite one-dimensional chain 73

3.6 Transport through an arbitrary scattering region 74

3.7 Basic features of the transport curve 77

3.7.1 Breit-Wigner Resonance 78

3.7.2 Fano-Resonance 79

3.8 Conclusion 82

3.9 Bibliography 83

Chapter 4 85

Tuning Fermi Level Alignment in Large Scale Self-Assembled Oligo (phenylene-ethynylene) Derivatives 85

4.1 Motivation 86

4.2 Three-terminal junction 87

4.3 Molecular structure 89

4.4 Frontier orbitals 94
4.5 Binding energy 100
4.5.1 Binding energy on graphene sheet 101
4.5.2 Binding energy on gold surface 103
4.6 Optimised DFT structures of compounds within their junctions 107
4.7 The tilt angle (θ) 111
4.8 Model of three-terminal junction 116
4.9 Transport calculations in a three-terminal junction 117
4.9.1 Au flat surface 117
4.9.2 Au-cluster 126
4.10 Conclusion 133
4.11 Bibliography 134
Chapter 5 142
The thermoelectric properties of Oligo (phenylene-ethynylene) Derivatives 142
5.1 Introduction 142
5.2 Seebeck coefficient 143
5.2.1 Au-flat surface 144
5.2.2 Au-cluster 152
5.3 Conclusion 161
5.4 Bibliography 162
Chapter 6 165
6. Conclusion and Future Work 165

6.1 Conclusion 165

6.2 Future Work 167

6.3 Bibliography 168

List of Figures

Fig. 2.1: Schematic of the self-consistency process within SIESTA. 49

Fig. 3.1: Tight-binding model of a one-dimensional infinite crystalline chain with on-site energies εo and couplings $-\gamma$..... 58

Fig. 3.2: The dispersion relation of infinite linear chain. 59

Fig. 3.3: Tight-binding model of a one-dimensional chain, in which all the site energies and bonds are arbitrary. 60

Fig. 3.4: Tight-binding model of one-dimensional crystalline chain with a single impurity at site $j = 0$. 62

Fig. 3.5: A scattering region connected to two electrodes, which in turn are attached to two reservoirs with chemical potential μL and μR. 65

Fig. 3.6: Tight-binding representation of one-dimensional infinite chain with on-site energies εo and couplings $-\gamma$. 69

Fig. 3.7: A semi-infinite linear chain with site energies εo and hopping elements $-\gamma$**,** which terminates at site $j = l$. 71

Fig. 3.8: A finite one-dimensional chain with on-site energies εo and hopping elements $-\gamma$. 73

Fig. 3.9: Tight-binding representation of an arbitrary scattering region attached to (1-D) leads. 74

Fig. 3.10: The effect of varying the coupling on the width of resonance. 79

Fig. 3.11: The transmission coefficient for a symmetric molecule attached symmetrically to identical leads ($\Gamma 1 = \Gamma 2$). 79

Fig. 3.12: Tight binding model of Fano-resonance, where a doubly- infinite chain coupled to a pendant site εp by coupling integral $-\alpha$..... 80

Fig. 3.13: The transmission coefficient versus energy E for different values of α at εp= -0.5 81

Fig. 4.1: Three-terminal concept for nanoscale switch with source and drain and gate electrodes[30].....89

Fig. 4.2: Selected anchors groups used in the formation of OPE molecular junctions, for simplicity, anchors groups are shown attached to a benzene ring unless they already form part of the terminal aromatic system (e.g., pyridine derivatives)[35]. a: Thiol (-SH), b: Pyridine (-C_5H_4N), c: Thioacetate (-SAc), d: Thioether (-SMe), e: Carbazole-based tetrapod x=CH, N.91

Fig. 4.3: Chemical structures of molecules **1-6** studied in this chapter. 92

Fig. 4.4: Fully relaxed isolated molecules **1-6**. Key: C = grey, H = white, O = red, S = yellow, N=blue.....93

Fig. 4.5: Wave function for **1**. **Top panel**: Fully optimised geometry of **1**. **Lower panel**: HOMO, LUMO, HOMO–1 and LUMO+1 along with their energies. 94

Fig. 4.6: Wave function for **2**. **Top panel**: Fully optimised geometry of **2**. **Lower panel**: HOMO, LUMO, HOMO–1 and LUMO+1 along with their energies. 95

Fig. 4.7: Wave function for **3**. **Top panel**: Fully optimised geometry of **3**. **Lower panel**: HOMO, LUMO, HOMO–1 and LUMO+1 along with their energies. 96

Fig. 4.8 : Wave function for **4**. **Top panel**: Fully optimised geometry of **4**. **Lower panel**: HOMO, LUMO, HOMO–1 and LUMO+1 along with their energies. 97

Fig. 4. 9: Wave function for **5**. **Top panel**: Fully optimised geometry of **5**. **Lower panel**: HOMO, LUMO, HOMO–1 and LUMO+1 along with their energies. 98

Fig. 4.10: Wave function for **6**. **Top panel:** Fully optimised geometry of **6**. **Lower panel**: HOMO, LUMO, HOMO–1 and LUMO+1 along with their energies. 99

Fig. 4.11: Phenyl ring (molecule **1**) on a graphene surface (Right panel). Energy difference of phenyl anchor to graphene as a function of molecule-contact distance. The equilibrium distance corresponds to the energy minimum and is found to be approximately 2.4 Å (Left panel). . 102

Fig. 4.12: Pyridine anchor (molecule **2**) on a graphene surface (Right panel). Energy difference of pyridine anchor to graphene as a function of molecule-contact distance. The equilibrium distance is approximately 2.7 Å (Left panel). 102

Fig. 4.13: Thioacetate anchor (molecule **2**) on a graphene surface (Right panel). Energy difference of thioacetate anchor to graphene as a function of molecule-contact distance. The equilibrium distance is approximately 5.7 Å (Left panel). 103

Fig. 4.14: Pyridine anchor (molecule **2**) on a gold surface (Right panel). Energy difference of pyridine anchor to gold as a function of molecule-contact distance. The equilibrium distance is approximately 2.5 Å (Left panel). 104

Fig. 4.15: Thiol anchor (molecule **2**) on a gold surface (Right panel). The acetate group has been released. Energy difference of thiol anchor to gold as a function of molecule-contact distance. The equilibrium distance is approximately 0.27 nm (Left panel)..... 105

Fig. 4.16:Thioether anchor (molecule **6**) on a gold surface (Right panel). Energy difference of 4 thioether anchors to flat gold as a function of molecule-contact distance. The equilibrium distance is approximately 4.2 Å (Left panel). 105

Fig. 4.17: Schematic illustration of an asymmetric junction containing a single molecule **1**. The top contact is single-layer graphene (SLG) and the bottom contact is gold. Note: here the molecule is asymmetric as well as the contacts (i.e., Gr and Au)..... 108

Fig. 4.18: Schematic illustration of asymmetric molecular junctions for **a** and **b. a** and **b** show how the molecule **2** flips between the Gr sheet and Au. **a** is when Py is linked to the Gr and **b** is when thioacetate is linked to the Gr. (Note: **2a** and **2b** molecular junctions are doubly asymmetric)..... 109

Fig. 4.19: Schematic illustration of asymmetric molecular junctions for **a** and **b. a** and **b** show how the molecule **3** flips between the Gr sheet and Au. **a** is when Py is linked to the Gr and **b** is when thioacetate is linked to the Gr (again these molecular junctions are doubly asymmetric). 109

Fig. 4.20: Schematic illustration of an asymmetric junction containing a single molecule **4**. The top contact is single-layer graphene (SLG) and the bottom contact is gold. Note: here thiol is linked to Au (due to the cleavage of the thioacetate in the presence of Au), and thioacetate is linked to Gr. 110

Fig. 4.21: Schematic illustration of an asymmetric junction containing a single molecule **5**. The top contact is single-layer graphene (SLG) and the bottom contact is gold. Again, thiol here is linked to Au (due to the cleavage of the thioacetate in the presence of Au), and thioacetate is linked to Gr. 110

Fig. 4.22: Schematic illustration of an asymmetric junction containing a single molecule **6**. The top contact is single-layer graphene (SLG) and the bottom contact is gold. Here, 4 SMe are linked to Au and Py is linked to Gr..... 111

Fig. 4.23: Schematic representation of the tilt angle model θ, which varies between the graphene sheet and the substrate gold..... 112

Fig. 4.24: Schematic illustration of Au/**1**/SLG junction with a tilt angle $\theta \approx 40^{o}$ for molecule **1** between Gr sheet and gold..... 113

Fig. 4.25: Schematic illustration of Au/**2a** and **2b**/SLG junctions with tilt angles of $\theta \approx 40^{o}$ and 70^{o} respectively for **2a** and **2b** between Gr sheet and gold..... 114

Fig. 4.26: Schematic illustration of Au/**3a** and **3b**/SLG junctions with tilt angles of $\theta \approx 40^{o}$ and 15^{o} respectively for **3a** and **3b** between Gr sheet and gold..... 114

Fig. 4.27: Schematic illustration of Au/**4**/SLG junction with a tilt angle of $\theta \approx 40^{o}$ for molecule **4** between Gr sheet and gold..... 115

Fig. 4.28: Schematic illustration of Au/**5**/SLG junction with a tilt angle of θ ≈ 40° for molecule **5** between Gr sheet and gold. 115

Fig. 4.29: Schematic illustration of Au/**6**/SLG junction with a tilt angle of θ ≈ 42° for molecule **6** between Gr sheet and gold. 115

Fig. 4.30: Schematic illustration of a three-terminal junction with periodic boundary conditions along the *y*-axis. The direct path 1-2: electrons of energy *E* flow directly from electrode 1 to 2, path 1-3: electrons passing from the top-left electrode (lead 1) to the bottom electrode (lead 3), and path 2-3**:** electrons travelling from the top-right electrode (lead 2) to the bottom electrode (lead 3). 116

Fig. 4.31: Top panel: Schematic illustration of a three-terminal Au/**1**/SLG junction with periodic boundary conditions along the *y*-axis. The top contact is SLG and is divided into two electrodes (electrode 1 and electrode 2), whereas the bottom contact is Au (electrode 3). Bottom panel: An example of zero-bias transmission coefficient *T*(*E*) curves: 1-3 and 2-3 have an equal path length, and therefore have identical curves (black and blue lines). 118

Fig. 4.32: Top panel: Schematic illustration of a three-terminal Au/**1**/SLG junction with periodic boundary conditions along the *y*-axis, as in Fig. 4.31. Bottom panel: Zero-bias transmission coefficient *T*(*E*) averaged over the values for paths 1-3 and 2-3 shown in Fig. 4.31..... 119

Fig. 4.33: Top panel: Schematic illustration of a three-terminal Au/**2a** or **2b**/SLG junction with periodic boundary conditions along the *y*-axis. Bottom panel: Zero-bias transmission coefficients *T*(*E*) of molecule **2** as a function of energy. 120

Fig. 4.34: Top panel: Schematic illustration of a three-terminal Au/**3a** or **3b**/SLG junction with periodic boundary conditions along the *y*-axis. Bottom panel: Zero-bias transmission coefficients *T*(*E*) of molecule **3** as a function of energy. 121

Fig. 4.35: Top panel: Schematic illustration of a three-terminal Au/**4**/SLG junction with periodic boundary conditions along the *y*-axis. Bottom panel: Zero-bias transmission coefficient *T*(*E*) of molecule **4** as a function of energy. 122

Fig. 4.36: Top panel: Schematic illustration of a three-terminal Au/**5**/SLG junction with periodic boundary conditions along the *y*-axis. Bottom panel: Zero-bias transmission coefficient *T*(*E*) of molecule **5** as a function of energy. 123

Fig. 4.37: Top panel: Schematic illustration of a three-terminal Au/**6**/SLG junction with periodic boundary conditions along the *y*-axis. Bottom panel: Zero-bias transmission coefficient *T*(*E*) of molecule **6** as a function of energy. 124

Fig. 4. 38. **a:** Zero-bias transmission coefficient *T*(*E*) of molecules **1-5** as a function of energy. The HOMO resonance is predicted to be pinned near the DFT-predicted Fermi energy. **b:** For side-by-side comparison with the other transmission coefficients, this shows the zero-bias transmission coefficient *T*(*E*) of **6**, reproduced from Fig. 4.37. The LUMO resonance is predicted to be pinned near the DFT-predicted Fermi energy (flat Au substrate). Note: All the transmission curves here for a flat Au surface. 125

Fig. 4.39: Top panel: Schematic illustration of a three-terminal Au/**1**/SLG junction with periodic boundary conditions along the *y*-axis. The top contact is SLG and is divided into two electrodes (electrode 1 and electrode 2), whereas the bottom contact is an add-atom Au (electrode 3). Bottom panel**:** Zero-bias transmission coefficient *T*(*E*) of molecule **1** as a function of energy (insensitive case). 126

Fig. 4.40: Top panel: Schematic illustration of a three-terminal Au/**2a** or **2b**/SLG junction with periodic boundary conditions along the *y*-axis. The top contact is SLG, whereas the bottom contact is an add-atom Au. Bottom panel**:** Zero-bias transmission coefficient *T*(*E*) of molecule **2** as a function of energy (sensitive case). Note: the transmission curve is the average of **2a** and **2b** curves. 127

Fig. 4.41: Top panel: Schematic illustration of a three-terminal Au/**3a** or **3b**/SLG junction with periodic boundary conditions along the *y*-axis. The top contact is SLG, whereas the bottom contact is an add-atom Au. Bottom panel**:** Zero-bias transmission coefficient $T(E)$ of molecule **3** as a function of energy (sensitive case). Note: the transmission curve is the average of **3a** and **3b** curves. 128

F**ig. 4.42**: Top panel: Schematic illustration of a three-terminal Au/**4**/SLG junction with periodic boundary conditions along the *y*-axis. The top contact is SLG, whereas the bottom contact is an add-atom Au. Bottom panel: Zero-bias transmission coefficient $T(E)$ of molecule **4** as a function of energy (insensitive case). 129

Fig. 4.43: Top panel: Schematic illustration of a three-terminal Au/**5**/SLG junction with periodic boundary conditions along the *y*-axis. The top contact is SLG, whereas the bottom contact is an add-atom Au. Bottom panel: Zero-bias transmission coefficient $T(E)$ of molecule **5** as a function of energy (insensitive case). 130

Fig. 4.44: Top panel: Schematic illustration of a three-terminal Au/**6**/SLG junction with periodic boundary conditions along the *y*-axis. The top contact is SLG, whereas the bottom contact is an add-atom Au. Bottom panel: Zero-bias transmission coefficient $T(E)$ of molecule **6** as a function of energy (insensitive case). 131

Fig. 4.45. **a:** Zero-bias transmission coefficient $T(E)$ of molecules **1, 4** and **5** as a function of energy, the HOMO resonance is predicted to be pinned near the DFT-predicted Fermi energy. **b:** Zero-bias transmission coefficient $T(E)$ of **2, 3** and **6,** the LUMO resonance is predicted to be pinned near the DFT-predicted Fermi energy (add-atom Au substrate). 132

Fig. 5.1: Top panel: Schematic illustration of a three-terminal Au/**1**/SLG junction. The top contact is SLG, whereas the bottom contact is a flat Au. Bottom panel: the room-temperature Seebeck over a range of Fermi energies EF relative to the DFT-predicted Fermi energy $EDFT$ for molecule **1**. 145

Fig. 5.2: Top panel: Schematic illustration of a three-terminal Au/**2a** or **2b**/SLG junction. The top contact is SLG, whereas the bottom contact is a flat Au. Bottom panel: the room-temperature Seebeck over a range of Fermi energies EF relative to the DFT-predicted Fermi energy $EDFT$ for molecule **2**. 146

Fig. 5.3: Top panel: Schematic illustration of a three-terminal Au/**3a** or **3b**/SLG junction. The top contact is SLG, whereas the bottom contact is a flat Au. Bottom panel: the room-temperature Seebeck over a range of Fermi energies EF relative to the DFT-predicted Fermi energy $EDFT$ for molecule **3**. 147

Fig. 5. 4: Top panel: Schematic illustration of a three-terminal Au/**4**/SLG junction. The top contact is SLG, whereas the bottom contact is a flat Au. Bottom panel: the room-temperature Seebeck over a range of Fermi energies EF relative to the DFT-predicted Fermi energy $EDFT$ for molecule **4**. 148

Fig. 5.5: Top panel: Schematic illustration of a three-terminal Au/**5**/SLG junction. The top contact is SLG, whereas the bottom contact is a flat Au. Bottom panel: the room-temperature Seebeck over a range of Fermi energies EF relative to the DFT-predicted Fermi energy $EDFT$ for molecule **5.** 149

Fig. 5.6: Top panel: Schematic illustration of a three-terminal Au/**6**/SLG junction. The top contact is SLG, whereas the bottom contact is a flat Au. Bottom panel: the room-temperature Seebeck over a range of Fermi energies EF relative to the DFT-predicted Fermi energy $EDFT$ for molecule **6.** 150

Fig. 5.7: **a:** Room-temperature Seebeck coefficients over a range of Fermi energies EF relative to the DFT-predicted Fermi energy $EDFT$ of molecules **1-5**. A positive Seebeck coefficient is obtained at the DFT-predicted Fermi energy. **b:** Room-temperature Seebeck coefficient over a range of Fermi energies EF relative to the DFT-predicted Fermi energy $EDFT$ of molecule **6**.

A negative Seebeck coefficient is obtained at the DFT-predicted Fermi energy. (Note: Simulations here for a flat Au surface). 151

Fig. 5. 8: Top panel: Schematic illustration of a three-terminal Au/**1**/SLG junction. The top contact is SLG, whereas the bottom contact is an add-atom Au. Bottom panel: Room-temperature Seebeck over a range of Fermi energies EF relative to the DFT-predicted Fermi energy $EDFT$ for molecule **1** 153

Fig. 5. 9 : Top panel: Schematic illustration of a three-terminal Au/**2**/SLG junction. The top contact is SLG, whereas the bottom contact is an add-atom Au. Bottom panel: the average room-temperature Seebeck over a range of Fermi energies EF relative to the DFT-predicted Fermi energy $EDFT$ for molecule **2**..... 154

Fig. 5.10: Top panel: Schematic illustration of a three-terminal Au/**3**/SLG junction. The top contact is SLG, whereas the bottom contact is an add-atom Au. Bottom panel: the average room-temperature Seebeck over a range of Fermi energies EF relative to the DFT-predicted Fermi energy $EDFT$ for molecule **3**..... 155

Fig. 5.11: Top panel: Schematic illustration of a three-terminal Au/**4**/SLG junction. The top contact is SLG, whereas the bottom contact is an add-atom Au. Bottom panel: Room-temperature Seebeck over a range of Fermi energies EF relative to the DFT-predicted Fermi energy $EDFT$ for molecule **4**. 156

Fig. 5.12: op panel: Schematic illustration of a three-terminal Au/**5**/SLG junction. The top contact is SLG, whereas the bottom contact is an add-atom Au. Bottom panel: Room-temperature Seebeck over a range of Fermi energies EF relative to the DFT-predicted Fermi energy $EDFT$ for molecule **5**. 157

Fig. 5.13: Top panel: Schematic illustration of a three-terminal Au/**6**/SLG junction. The top contact is SLG, whereas the bottom contact is an add-atom Au. Bottom panel: Room-

temperature Seebeck over a range of Fermi energies EF relative to the DFT-predicted Fermi energy $EDFT$ for molecule **6**. 158

Fig. 5.14: **a:** Room-temperature Seebeck over a range of Fermi energies EF relative to the DFT-predicted Fermi energy $EDFT$ of molecules **1, 4** and **5**. A positive Seebeck coefficient is obtained at the DFT-predicted Fermi energy. **b:** Room-temperature Seebeck over a range of Fermi energies EF relative to the DFT-predicted Fermi energy $EDFT$ of molecules **2**, **3** and **6**. A negative Seebeck coefficient is obtained at the DFT-predicted Fermi energy. (Note: Simulations here for Au cluster). 159

List of Tables

Table 4.1: Summary of the energy-difference calculations (Figs. 4.11-4.16) for graphene-molecule (Gr-M) and gold-molecule (Au-M) contacts. *z* is the equilibrium distance and Δ(*z*) is the corresponding minimum energy difference. 106

Table 4.2: Experimental break-off distance (film thickness), and equivalent tilt angle (θ).. 113

Table 5. 1: Seebeck coefficient *S* at DFT-predicted Fermi E-E_F^{DFT}=0 eV for molecules **1-6**, which are bond to the flat Au and SLG. 152

Table 5. 2: Seebeck coefficient *S* at DFT-predicted Fermi E-E_F^{DFT}=0 eV for molecules **1-6**, which are bond to Au cluster and SLG. 160

Table 5. 3: Comparison of Seebeck coefficients *S* between Au-flat and cluster at DFT-predicted Fermi E-E_F^{DFT}=0 eV for molecules **1-6** 161

List of abbreviations

ME	Molecular electronics
DFT	Density Functional Theory
LDA	Local Density Approximation
GGA	Generalized Gradient Approximation
SCF	Self-Consistent Field
vdW	Van der Waals
DZ	Double-ξ basis set
DZP	Double- ξ polarized basis set
SIESTA	Spanish Initiative for Electronic Simulations with Thousands of Atoms
LCAOB	Linear Combination of Atomic Orbital Basis
BSSE	Basis set superposition error
CP	Counterpoise correction
TBM	Tight-binding model
$T(E)$	Transmission coefficient
$G(E)$	Electrical conductance
S	Seebeck coefficient
DOS	Density of States
STM	Scanning Tunnelling Microscopy
MCBJ	mechanically controlled break junction
EBJ	electromigration break junction
SAM	Self-Assembled Monolayer
SLG	single-layer graphene

OPE	Oligo (phenylene- ethynylene)
HOMO	Highest Occupied Molecular Orbital
LUMO	Lowest Occupied Molecular Orbital
EDL	Electrical double layer

Chapter 1

1.1 Molecular electronics

Molecular electronics (ME) is the field of science that investigates the electronic and thermal transport properties of circuits in which individual molecules (or assemblies of them) are used as basic building blocks[1]. This area of research has attracted significant attention both from the research community and industry, due to promising applications in nanoscale electronic devices such as transistors[2,3] , rectifies[4,5], sensors[6,7], and switches[8]. The idea of using single-molecule electronics, based on the bottom-up approach, is to assemble and design molecules to form more complex structures, active components and connecting wires. Molecular electronics offers enormous benefits for the research community and industry. For instance, the possibility to investigate electronic and thermal conduction at the smallest imaginable scale, where the typical size of molecules (between 1 and 10 nm) could lead to a higher packing density of devices with the subsequent advantages in cost, efficiency, and power consumption[1]. Another attractive feature is the intermolecular interactions which could be utilised in nanoscale self-assembly technology, potentially resulting in low-cost manufacturing. Furthermore, there is a huge diversity in the types of molecular structures that chemists can make, which means that properties of molecules can be rationally and systematically changed. Molecular junctions are also ideal systems to investigate the fundamental principles of electron transfer mechanisms[9–12]. These reasons and many others make molecular electronics a very attractive field of science.

The first suggestion of molecular electronics was put forward by Ratner and Aviram in 1974, when they proposed a theoretical molecular rectifier composed of donor and acceptor sites which are insulated from one another[13]. Research efforts have been devoted to exploring the properties and device opportunities of single molecules. However, the rapid development of molecular electronics only really took off during the past two decades in tandem with the rise of the nanoscience era and the availability of manipulation probes at the single molecule scale, such as the scanning tunnelling microscope (STM), mechanically controlled break junction (MCBJ) or electromigration break junction (EBJ) techniques[14–23]. First studies were carried out using STM which works by scanning a very sharp metal tip over a conducting surface within a range of several angstroms of it. When the tip is brought to such a close distance from the sample and a bias voltage is applied between the tip and the sample, a tunneling current flows through the vacuum gap that separates the two conductors, even though they are not in electrical contact[20]. STM has been used for many purposes, such as studying atomic and electronic structure of conductive surfaces, the dispersion relation between metallic surface states, and probing the electronic structure of highly correlated materials like high-TC superconductors. STM tip can be used to manipulate the positions of atoms and molecules on conductive surfaces. STM has been used to determine the vibrational and magnetic structure of several systems at the atomic scale and there have been many other useful uses of STM[24].

The second most used technique is the MCBJ developed by Muller et al in 1992. The principle of this method is a small piece of a metallic wire is fixed at two points on a flexible substrate, which can be called bending beam also. The cross section of the wire is reduced between two fixed points by making a notch near the middle of the wire. The bending substrate is fixed at both ends by counter supports. As the beam is bent, the sample wire starts to elongate between the two fixed

points, which results in the reduction of the cross section at the notch, and finally the wire completely raptures. After break the wire, two clean facing nano-electrodes were generated. The distance between the electrodes for both the opened and the closed directions was controlled by bending or relaxing the substrate, respectively. After integrating the molecules into the gap, they may bridge the two electrodes and the electronic properties of the molecules can be determined[25]. The MCBJ technique, as compared with the STM approach, allows control of the separation between two electrodes with extremely high stability and precision, which has attracted great interest with respect to its application in molecular charge-transport studies. On the other hand, although it is very useful for investigating the fundamental properties of electronic transport on the molecular scale, it might be less appropriate for the fabrication of highly integrated molecular electronics devices[25].

Simulations based on first principles density functional theory (DFT) emerged as an essential theoretical tool in tandem with these experimental methodologies, which allows the researchers to construct a quantitative picture of transport mechanisms and form predictions to quid further experimental studies.

It is worth noting that creating a single-molecule device is not an easy task, due to some challenges and limitations. First, due to the tiny dimensions of the molecule, it is typically impractical to place the molecule in the nanogap by direct manipulation. Instead, chemical interaction between the molecule and the electrode is needed for the positioning of a molecule in the gap between the electrodes. Second, since the electrodes are typically much larger than the molecules, it is an additional challenge to make sure that only a single molecule is placed in each functional device.

In addition to these challenges, other challenges such as device stability, uniformity and scalability are equally important[21,26–29].

Despite these challenges and limitations to both theory and experiment, great progress has been achieved in the development of molecular electronics, providing a valuable to roadmap for future electronics applications. This thesis covers basic concepts in the quantum transport theory required to describe fundamental aspects of molecular junctions in the nanoscale, including the density functional theory (DFT), which is implemented in the SIESTA code[30], and the non-equilibrium Green's function formalism of transport theory, which is implemented in the Gollum code[31].

The term molecular junction is an important concept in which a molecular cluster is placed between two electrodes, and electrons are transferred across it, and in many molecular junctions, a molecule is normally sandwiched between two electrodes. In this thesis, I will present my contributions to the field of molecular electronics, with a focus on the understanding of electron transport in three-terminal molecular junctions, where a single molecule is tethered between two contacting electrodes (source and drain), while a third electrode acts as a gate bias to control the conductance[32].

Building three-terminal junction is considered to be a critical step forward in molecular electronics. To achieve this goal, molecular junction systems must incorporate a gating electrode by applying a voltage on the gate, in which one can change the electrostatic potential of the molecule. Energy shifts of the molecular transport level are then induced, from which additional information about the molecule can be obtained such as the presence of vibrational modes and excited states and the

presence of vibrationally induced effects such as Franck–Condon blockade. The gate has also played a crucial role in studying Kondo Physics, and superconductivity. Three-terminal devices also enabled to read-out and driving of a single nuclear spin, which can be used as molecular quantum bit[3].

Compared with a two-terminal junction, a three-terminal device combines both the ability to form a stable single-molecule junction via the mechanically controllable break junction (MCBJ) technique and the ability to shift the energy levels of the molecule using a side-gate electrode in a noncontact configuration[33]. Moreover, the three-terminal molecular junction presents a new platform for fabricating highly stable single-molecule transistor junctions[19]. It should be noted that the construction of a three-terminal junction is not easy because it requires to (1) find a reliable method to bridge a single molecule to the source and drain electrodes and (2) place the gate electrode a few nanometers away from the molecule to achieve the required gate field.

In recent years, research labs around the world are aiming to create high-performance thermoelectric materials and devices, which can convert the waste heat back into electricity [24,34–39]. The Seebeck effect was discovered by the German physicist Thomas Johann Seebeck in 1821 and refers to the occurrence of a voltage difference. due to the temperature difference across the material. The voltage difference (ΔV) originates from the diffusion of majority charge carriers (electrons or holes) from the hot side to the cold side due to the applied temperature gradient (ΔT). The ratio of the developed voltage gradient to the temperature gradient is known as the Seebeck coefficient ($S = -\frac{\Delta V}{\Delta T}$) or the thermopower. The magnitude and sign of the Seebeck coefficient are related to an asymmetry of the electron distribution around the Fermi level[40–43]. It is worth

mentioning that there is a need for thermopowers of both positive and negative signs, so that materials with thermopowers of opposite signs can be organised in tandem to boost the thermovoltage[24].

1.2 Thesis Outline

The outline of this thesis can be summarised as follows; this chapter is followed by **chapter 2** which presents a brief overview of density functional theory (DFT), which is one of the main theoretical techniques that has been used in this thesis to study and understand the electronic properties of single-molecule junctions. **Chapter 3** describes the single particle transport theory. This chapter involves Green's functions for different transport regimes based on the scattering theory, and related topics such as the Landauer formula, with some examples of how to calculate the transmission coefficient for different systems using the Hamiltonian and Green's functions.

This is followed by my first results chapter which investigates the effects of orbital alignment in large-scale self-assembled monolayers (SAMs), with a single-layer graphene (SLG) as a top contact and gold as a bottom electrode. This study is a result of a collaboration between chemists from Durham University, experimental physicists from Cambridge University and myself in Lancaster. The SAMs are formed from oligo (phenylene-ethynylene) (OPE)-based molecular wires with different molecule-electrode contacts, including SAc, SMe and Py. In this work, I model the three-terminal junction, where the top contact is SLG, which is divided into two electrodes (electrode 1 and electrode 2), whereas the bottom contact is Au (electrode 3). The electronic properties of these SAMs were envisaged and assorted as either HOMO- or LUMO-dominated molecules. At the end of this chapter, the shape of the Au electrode is changed to investigate how this affects the Fermi level alignment and, thereby, the conductance. **Chapter 5,**

the second results chapter, presents the thermoelectric properties of the molecules that were studied in chapter 4. The influence of the shape of the Au electrode (i.e., flat and cluster) on the sign of the Seebeck coefficient is also investigated. **Chapter 6** summarises my conclusions and highlights some directions for future research in this topic.

1.3 Bibliography

(1) Cuevas, J. C.; Scheer, E. *Molecular Electronics: An Introduction to Theory and Experiment*; World Scientific series in nanoscience and nanotechnology; World Scientific: Singapore ; Hackensack, NJ, 2010.

(2) Martel, R.; Schmidt, T.; Shea, H. R.; Hertel, T.; Avouris, Ph. Single- and Multi-Wall Carbon Nanotube Field-Effect Transistors. *Appl. Phys. Lett.* **1998**, *73* (17), 2447–2449.

(3) Perrin, M. L.; Burzurí, E.; van der Zant, H. S. J. Single-Molecule Transistors. *Chem. Soc. Rev.* **2015**, *44* (4), 902–919.

(4) Saha, M.; Maiti, S. K. High Degree of Current Rectification at Nanoscale Level. *Phys. E Low-Dimens. Syst. Nanostructures* **2017**, *93*, 275–278.

(5) Batra, A.; Darancet, P.; Chen, Q.; Meisner, J. S.; Widawsky, J. R.; Neaton, J. B.; Nuckolls, C.; Venkataraman, L. Tuning Rectification in Single-Molecular Diodes. *Nano Lett.* **2013**, *13* (12), 6233–6237.

(6) Sadeghi, H.; Bailey, S.; Lambert, C. J. Silicene-Based DNA Nucleobase Sensing. *Appl. Phys. Lett.* **2014**, *104* (10), 103104.

(7) Sadeghi, H.; Algaragholy, L.; Pope, T.; Bailey, S.; Visontai, D.; Manrique, D.; Ferrer, J.; Garcia-Suarez, V.; Sangtarash, S.; Lambert, C. J. Graphene Sculpturene Nanopores for DNA Nucleobase Sensing. *J. Phys. Chem. B* **2014**, *118* (24), 6908–6914.

(8) Jan van der Molen, S.; Liljeroth, P. Charge Transport through Molecular Switches. *J. Phys. Condens. Matter* **2010**, *22* (13), 133001..

(9) Heath, James R., and Mark A. Ratner. *Molecular electronics*. The National Academies Press, Washington, 2003.

(10) Mathew, P. T.; Fang, F. Advances in Molecular Electronics: A Brief Review. *Engineering* **2018**, *4* (6), 760–771.

(11) Liu, R.; Ke, S.-H.; Baranger, H. U. Intermolecular Effect in Molecular Electronics. *J Chem Phys* **2005**, 5.

(12) Xin, N.; Guo, X. Catalyst: The Renaissance of Molecular Electronics. *Chem* **2017**, *3* (3), 373–376.

(13) Ratner, M. A Brief History of Molecular Electronics. *Nat. Nanotechnol.* **2013**, *8* (6), 378–381.

(14) Giessibl, F. J. Advances in Atomic Force Microscopy. *Rev Mod Phys* **2003**, *75* (3), 35.

(15) Taychatanapat, T.; Bolotin, K. I.; Kuemmeth, F.; Ralph, D. C. Imaging Electromigration during the Formation of Break Junctions. *Nano Lett.* **2007**, *7* (3), 652–656.

(16) Xiang, D. *Fabrication and Utilization of Mechanically Controllable Break Junction for Bioelectronics*; Schriften des Forschungszentrums Jülich Reihe Schlüsseltechnologien; Forschungszentrum Jülich: Jülich, 2012.

(17) Sakata, S.; Umeno, A.; Yoshida, K.; Hirakawa, K. Mechanism of Electromigration and Spontaneous Formation of Single Electron Transistors at Ultrasmall Copper Nano-Junctions. 2009.

(18) Wang, K.; Xu, B. Modulation and Control of Charge Transport Through Single-Molecule Junctions. *Top. Curr. Chem.* **2017**, *375* (1), 17.

(19) Xiang, D.; Wang, X.; Jia, C.; Lee, T.; Guo, X. Molecular-Scale Electronics: From Concept to Function. *Chem. Rev.* **2016**, *116* (7), 4318–4440.

(20) Hansma, P. K.; Tersoff, J. Scanning Tunneling Microscopy. *Journal of Applied Physics.* 1987, *61*(2), R1-R24.

(21) Tsutsui, M.; Taniguchi, M. Single Molecule Electronics and Devices. *Sensors* **2012**, *12* (6), 7259–7298.

(22) Zhao, Y.; Liu, W.; Zhao, J.; Wang, Y.; Zheng, J.; Liu, J.; Hong, W.; Tian, Z.-Q. The Fabrication, Characterization and Functionalization in Molecular Electronics. *Int. J. Extreme Manuf.* **2022**.

(23) Zhang, J. L.; Zhong, J. Q.; Lin, J. D.; Hu, W. P.; Wu, K.; Xu, G. Q.; Wee, A. T. S.; Chen, W. Towards Single Molecule Switches. *Chem. Soc. Rev.* **2015**, *44* (10), 2998–3022.

(24) Ismael, A. K. Towards Molecular-Scale Sensing and Thermoelectric Energy Harvesting. 179.

(25) Hong, W.; Valkenier, H.; Mészáros, G.; Manrique, D. Z.; Mishchenko, A.; Putz, A.; García, P. M.; Lambert, C. J.; Hummelen, J. C.; Wandlowski, T. An MCBJ Case Study: The Influence of π-Conjugation on the Single-Molecule Conductance at a Solid/Liquid Interface. *Beilstein J. Nanotechnol.* **2011**, *2*, 699–713.

(26) Visions for a Molecular Future. *Nat. Nanotechnol.* **2013**, *8* (6), 385–389.

(27) Enoki, T.; Kiguchi, M. Challenges for Single Molecule Electronic Devices with Nanographene and Organic Molecules. Do Single Molecules Offer Potential as Elements of Electronic Devices in the next Generation? *Phys. Scr.* **2018**, *93* (5), 053001.

(28) Vilan, A.; Cahen, D.; Aswal, D. K.; Debnath, A. K. Molecular Electronics—Current Challenges; Mumbai, (India), 2010; pp 30–33.

(29) Guo, X.; *AIMS Mater Sci,* **2014**, *1* (1), 11–14.

(30) Soler, J. M.; Artacho, E.; Gale, J. D.; García, A.; Junquera, J.; Ordejón, P.; Sánchez-Portal, D. The SIESTA Method for *Ab Initio* Order- *N* Materials Simulation. *J. Phys. Condens. Matter* **2002**, *14* (11), 2745–2779.

(31) Ferrer, J.; Lambert, C. J.; García-Suárez, V. M.; Manrique, D. Z.; Visontai, D.; Oroszlany, L.; Rodríguez-Ferradás, R.; Grace, I.; Bailey, S. W. D.; Gillemot, K.; Sadeghi, H.; Algharagholy, L. A. GOLLUM: A next-Generation Simulation Tool for Electron, Thermal and Spin Transport. *New J. Phys.* **2014**, *16* (9), 093029.

(32) Osorio, E. A.; Bjørnholm, T.; Lehn, J.-M.; Ruben, M.; van der Zant, H. S. J. Single-Molecule Transport in Three-Terminal Devices. *J. Phys. Condens. Matter* **2008**, *20* (37), 374121.

(33) Xiang, D.; Jeong, H.; Kim, D.; Lee, T.; Cheng, Y.; Wang, Q.; Mayer, D. Three-Terminal Single-Molecule Junctions Formed by Mechanically Controllable Break Junctions with Side Gating. *Nano Lett.* **2013**, *13* (6), 2809–2813.

(34) Wilkinson, L. A. Assembly, Structure and Thermoelectric Properties of 1,1′-Dialkynylferrocene 'Hinges.' *Chem. Sci.* **2022**, 8.

(35) Bennett, T. L. R. Multi-Component Self-Assembled Molecular-Electronic Films: Towards New High-Performance Thermoelectric Systems. *Chem. Sci.* **2022**, 10.

(36) Ismael, A. Molecular-Scale Thermoelectricity: As Simple as 'ABC.' **2020**, 6.

(37) Ismael, A. Tuning the Thermoelectrical Properties of Anthracene-Based Self-Assembled Monolayers. *Chem. Sci.* **2020**, 6.

(38) Yzambart, G.; Rincón-García, L.; Al-Jobory, A. A.; Ismael, A. K.; Rubio-Bollinger, G.; Lambert, C. J.; Agraït, N.; Bryce, M. R. Thermoelectric Properties of 2,7-Dipyridylfluorene Derivatives in Single-Molecule Junctions. *J Phys Chem C* **2018**, 7.

(39) Rincón-García, L.; Ismael, A. K.; Evangeli, C.; Grace, I.; Rubio-Bollinger, G.; Porfyrakis, K.; Agraït, N.; Lambert, C. J. Molecular Design and Control of Fullerene-Based Bi-Thermoelectric Materials. *Nat. Mater.* **2016**, *15*, 6.

(40) Ismael, A. K.; Grace, I.; Lambert, C. J. Increasing the Thermopower of Crown-Ether-Bridged Anthraquinones. *Nanoscale* **2015**, *7* (41), 17338–17342.

(41) Alshammari, M.; Al-Jobory, A. A.; Alotaibi, T.; Lambert, C. J.; Ismael, A. Orientational Control of Molecular Scale Thermoelectricity. *Nanoscale Adv.* **2022**, *4* (21), 4635–4638.

(42) Al-Khaykanee, M. K.; Ismael, A. K.; Grace, I.; Lambert, C. J. Oscillating Seebeck Coefficients in π-Stacked Molecular Junctions. *RSC Adv.* **2018**, *8* (44), 24711–24715.

(43) Ismael, A. K.; Rincón-García, L.; Evangeli, C.; Dallas, P.; Alotaibi, T.; Al-Jobory, A. A.; Rubio-Bollinger, G.; Porfyrakis, K.; Agraït, N.; Lambert, C. J. Exploring Seebeck-Coefficient Fluctuations in Endohedral-Fullerene, Single-Molecule Junctions. *Nanoscale Horiz.* **2022**.

Chapter 2

2. Density Functional Theory

Simulations based on density functional theory (DFT) have emerged as a powerful theoretical tool, that allows researchers to construct a quantitative picture of transport mechanisms and form predictions to guide further experimental studies. This chapter introduces the basic principles of DFT, and its implementation used in this thesis, namely the SIESTA code, which is applied to all studied electronic structure calculations.

2.1 Introduction

Density functional theory (DFT) is one of the most successful approaches to the calculation of the ground- state properties of quantum many-body problems such as atoms, molecules, solids and nuclear systems. It is a theory of electronic structure, based on the electron density distribution $\rho(r)$ as the carrier of all information in the molecular (or atomic) ground state, instead of the many-electron wave function $\psi(r_1, r_2, r_3, \ldots\ldots)$[1,2]. It overcomes the limitations of wave mechanics, by reducing the complexity (number of degrees of freedom) of the problem by dealing with electron density functionals. The history of this method can be traced back to the pioneering work of Hohenberg and Kohn, which implies that any ground- state expectation value can be written as a functional of the density alone[3]. Since then, DFT has stimulated a vast amount of work in electronic structure theory, as it provides a possible approach to calculate the ground-state properties of many-electron systems.

The purpose of this chapter is to give a brief summary of the DFT and its implementation in the SIESTA code (Spanish Initiative for Electronic Simulations with Thousands of Atoms)[4], which has been used as a theoretical tool to study the electronic properties of molecules that are the subject of the research in this thesis. I will introduce the general theoretical principles, that constitute the basis of the DFT approach, starting from the Born-Oppenheimer approximation of the nuclei, and the Hohenberg-Kohn theorem, followed by the Kohn-Sham theorem, which solves the intractable many-body problem of interacting electrons in an external potential by converting it into a tractable problem of non-interacting electrons in an effective potential. In addition, the idea of the pseudo-potentials and the basis set is presented to simplify the task of constructing electronic wave functions.

2.2 Many-body problem

The many-body problem is one of the most intractable problems of quantum physics. The great difficulty is that the motion of the electrons in atoms and molecules are correlated because of the strong Coulomb repulsion between their negative charges[5]. In a microscopic system consisting of charged nuclei surrounded by electron clouds, the interactions such as electron-electron, electron-nuclei and nuclei-nuclei are described via the Schrodinger equation:

$$H\,\psi_i\left(\vec{r}_1, \vec{r}_2, \dots, \vec{r}_N, \vec{R}_1, \vec{R}_2, \dots\dots, \vec{R}_M\right) = E_i\psi_i\left(\vec{r}_1, \vec{r}_2, \dots, \vec{r}_N, \vec{R}_1, \vec{R}_2, \dots\dots, \vec{R}_M\right) \quad (2.1)$$

Here H represents the time-independent Hamiltonian operator of the system consisting of N-electrons and M-nuclei which describes theses interactions, ψ_i is the wave function of the i^{th} state of the system and E_i is the numerical value of the energy of the i^{th} described by ψ_i .

In general, the Hamiltonian of many-body system can be written as:

$$H = -\frac{\hbar^2}{2m_e}\sum_i \nabla_i^2 - \frac{\hbar^2}{2m_I}\sum_I \nabla_I^2 + \frac{1}{8\pi\varepsilon_o}\sum_{i\neq j}\frac{e^2}{|r_i - r_j|} + \frac{1}{8\pi\varepsilon_o}\sum_{I\neq J}\frac{z_I z_J e^2}{|R_I - R_J|} - \frac{1}{4\pi\varepsilon_o}\sum_{iI}\frac{z_I e^2}{|r_i - R_I|} \qquad (2.2)$$

where

m_e and m_I are the mass of electron and nucleus, respectively.

r_i and R_I represent the position of electrons and nuclei, respectively.

e and z_I denote the electron and nuclear charge.

i and j represent the *N*-electrons while I and J represent a run over the *M*-nuclei in the system.

In equation (2.2), the first two terms represent the kinetic energy of electrons and nuclei, respectively. The third and fourth terms are the potential energy of electron and nuclei, respectively. The last term is electron-nuclei interactions. Obviously, for a simple system such as the hydrogen atom, the solving of the Schrodinger equation is obtainable. On the other hand, the exact solution for many-body systems with more than a view of electrons cannot be found unless some approximations are used. As a result of the fact that the nuclei are much heavier than an electron, the nuclear kinetic energy could be neglected to yield the Born- Oppenheimer approximation[6].

2.3. Born- Oppenheimer approximation

The Born-Oppenheimer approximation neglects the motion of the atomic nuclei when describing the electrons in a molecule[6]. The physical basis for this approximation is the fact that the mass of an atomic nucleus is much larger than the mass of an electron (more than 1000 times). Because of this difference, the nuclei move much more slowly than electrons, which means that the nuclear kinetic energy sums to zero and their potential energy is constant. Thus, the electronic Hamiltonian reduces to:

$$H = \underbrace{-\frac{\hbar^2}{2m_e}\sum_i \nabla_i^2}_{T_e} + \underbrace{\frac{1}{8\pi\varepsilon_o}\sum_{i\neq j}\frac{e^2}{|r_i - r_j|}}_{V_e} + \sum_i V_{ext}(r_i) \quad (2.3)$$

The first term of equation (2.3) T_e is the kinetic energy of all electrons, the second term V_e represents the interaction between electrons and the last term V_{ext} is the external potential due to nuclei and electron interaction, in addition to any external field.

Therefore, the corresponding time-independent Schrodinger equation can be written as:

$$H\,\psi_i(\vec{r}_1, \vec{r}_2, \dots, \vec{r}_i..) = E_i\psi_i(\vec{r}_1, \vec{r}_2, \dots, \vec{r}_i..) \quad (2.4)$$

ψ_i is a function of electron position $\vec{r}_i$ only.

Although, the size of the system has been reduced by using this approximation, it is still difficult to solve the Schrodinger equation. Therefore, density functional theory solves this problem by expressing the physical quantities in terms of the ground-state density $\rho_o(\vec{r})$, the electron density of a general many-body states characterized by a wave function $\psi(r_1, r_2, \dots\dots\dots r_N)$ is defined as:

$$\rho(\vec{r}) = N \int dr_2 dr_3 \dots dr_N \, |\psi(r_1, r_2, \dots\dots\dots r_N)|^2 \quad (2.5)$$

The factor N arises since all electrons are indistinguishable, and hence all the integrals evaluate to the same value.

2.4 The Hohenberg- Kohn theorem

The Hohenberg-Kohn theorems plays a fundamental role in density functional theory, which has become a basic tool for the study of electronic structure due its ability to determine the ground-state properties of a system and can be applied to any system of electrons moving in an external potential[7].

This approximation is primarily based on two theorems. The first theorem states that for any system of interacting particles in an external potential $V_{ext}(\vec{r})$, the potential $V_{ext}(\vec{r})$ is uniquely determined by the corresponding ground-state electronic density. The second theorem: the total energy of a system, which is a functional of the ground-state electron density, is minimized to the correct ground-state energy.

To prove the first theorem, suppose that there are two external potentials $V_1(\vec{r})$ and $V_2(\vec{r})$, that lead to the same ground state density $\rho_o(r)$. These potentials belong to different Hamiltonian, which are denoted $\widehat{H}_1$ and $\widehat{H}_2$.

The corresponding Schrodinger equations are given by:

$$\widehat{H}_1\,\psi_1 = E_1\,\psi_1$$

$$\widehat{H}_2\,\psi_2 = E_2\,\psi_2$$

As ψ_2 is not the ground state wavefunction of $\widehat{H}_1$,

$$E_1 = \langle\psi_1|\widehat{H}_1|\psi_1\rangle < \langle\psi_2|\widehat{H}_1|\psi_2\rangle \tag{2.6}$$

and similarly:

$$E_2 = \langle\psi_2|\widehat{H}_2|\psi_2\rangle < \langle\psi_1|\widehat{H}_2|\psi_1\rangle \tag{2.7}$$

Assuming that the ground states are non-degenerate[8,9], equation (2.6) can be rewritten as:

$$\begin{aligned}\langle\psi_2|\widehat{H}_1|\psi_2\rangle &= \langle\psi_2|\widehat{H}_2|\psi_2\rangle + \langle\psi_2|\widehat{H}_1 - \widehat{H}_2|\psi_2\rangle \\ &= E_2 + \langle\psi_2|V_1(\vec{r}) - V_2(\vec{r})|\psi_2\rangle \\ &= E_2 + \int dr\,[V_1(\vec{r}) - V_2(\vec{r})]\,\rho_o(r)\end{aligned} \tag{2.8}$$

and assuming that $|\psi_1\rangle$ has the same density $\rho_o(r)$ as $|\psi_2\rangle$

$$\langle\psi_1|\widehat{H}_2|\psi_1\rangle = E_1 + \int dr\,[V_2(\vec{r}) - V_1(\vec{r})]\,\rho_o(r) \tag{2.9}$$

Adding together the two equations (2.8) and (2.9) leads to,

$$E_1 + E_2 < E_1 + E_2 \tag{2.10}$$

The equation (2.10) shows a logical contradiction, hence it is clear that the two different external potentials cannot produce the same ground state density.

The second theorem can be realized in a similar way, which relates to the minimization of the total energy functional.

$$E[\rho] = T[\rho] + E_{int}[\rho] + \int dr\, V_{ext}(r)\, \rho(r) \tag{2.11}$$

The kinetic energy T and electron-electron interaction energy are only dependent on the charge density, and so are universal. The density $\rho(r)$ that minimizes the functional is the exact ground state density $\rho_o(r)$.

Although, the Hohenberg-Kohn theorems are extremely powerful, they do not the offer a way of computing the ground-state density of a system in practice. Therefore, Kohn-Sham devised a simple method for carrying-out DFT calculations, that retains the exact nature of DFT. This approximation will be discussed in the next section.

2.5 The Kohn-Sham theorem

The most successful way to implement the density functional theory is the method proposed by Kohn and Sham[10]. This formulation of the DFT has become the method of choice for the ground-state electronic-structure calculations across usually wide variety of field. In this approach, an interacting-electron system is replaced by a system of non-interacting electrons (fictious system) in an effective potential V_{eff}, in such a way that the density of this system is same as interacting one. This involves replacing the original Hamiltonian of interacting system with effective Hamiltonian of non-interacting particles in effective external potential[11,12].

The form of the energy functional of the Kohn-Sham is:

$$E_{KS}\ [\rho(r)] = T_{KS}\,[\rho(r)] + \int dr\ V_{ext}\,(r)\,\rho(r) + E_H\,[\rho(r)] + E_{xc}\,[\rho(r)] \tag{2.12}$$

Here, T_{ks} is the kinetic energy of non-interacting system, E_H represents the classical electrostatic energy (Hartree energy), which describes the electron-electron interaction of the classical charge distribution, using the Hartree-Fock[13,14] method and it is given by:

$$E_H\,[\rho(r)] = \frac{1}{2}\iint \frac{\rho(r)\,\rho(\acute{r})}{|r-\acute{r}|}\ dr\ d\acute{r} \tag{2.13}$$

The last term of equation (2.12) E_{xc} is the exchange and correlation energy[10], which is defined as the difference between the energy of the non-interacting and interacting system. In other words, E_{xc} represents the difference between the exact and approximated solutions to both the kinetic energy and the electron-electron interaction, that can be written as:

$$E_{xc}\,[\rho(r)] = (E_{int}\,[\rho(r)] - E_H\,[\rho(r)]) + (\,T\,[\rho(r)] - T_{KS}\,[\rho(r)]) \tag{2.14}$$

By taking the functional derivatives of the last three terms of equation (2.12), we can define an effective single particle potential V_{eff} as:

$$V_{eff}\,(r) = V_{ext}\,(r) + \frac{\partial}{\partial\rho}\,(E_H\,[\rho(r)] + E_{xc}\,[\rho(r)]) \tag{2.15}$$

Thus, we can write a single particle Hamiltonian as:

$$H_{KS}\ = T_{ks}[\rho] + V_{eff} \tag{2.16}$$

Then, the corresponding Schrodinger equation is given by:

$$H_{KS}\ \psi^{KS}\ = E\,\psi^{KS} \tag{2.17}$$

Equation (2.17) is known as Kohn-Sham equation.

2.6 The Exchange Correlation functional

As a result of applying the Kohn-Sham DFT, the quantum ground-state density of many-body system is reduced to one single-body problem. However, the exact form of the exchange-correlation energy is unknown, which is the biggest challenge of this approach. There are considerable proposed forms with varying level of accuracy for the exchange-correlation energy. However, the most used approximations are local density approximation (LDA)[15–17] and generalized gradient approximation (GGA)[18,19]. In what follows, I will present a brief overview to describe these approximations.

2.6.1 Local Density Approximation

The Local Density Approximation (LDA) is one of the first and most standard approximation for the exchange-correlation interaction. In the LDA, the density can be treated locally as a uniform electron gas, in which the energy depends on the density at the point where the functional is evaluated. The basic idea of this approximation is to divide the entire inhomogeneous electron region in the system into multiple small regions, and to approximate these small regions as a homogeneous electron gas[17]. Based on that, the LDA can be expressed as[17]:

$$E_{xc}^{LDA}[\rho] = \int \epsilon_{xc}^{hom}\left(\rho(r)\right)\rho(r)\,dr \tag{2.18}$$

where $\rho(r)$ is the electronic density at point r, and $\epsilon_{xc}^{hom}(\rho)$ stands for the exchange correlation energy of the homogeneous electron gas with density ρ, which is written as the sum of two separate contributions for exchange $\epsilon_x(\rho)$ and correlation $\epsilon_c(\rho)$ energies.

$$\epsilon_{xc}\big(\rho(r)\big) = \epsilon_x\big(\rho(r)\big) + \epsilon_c\big(\rho(r)\big) \tag{2.19}$$

The LDA is expected to be a good approximation for spatially slowly varying densities such as graphene and carbon nanotubes. Although this condition is hardly ever met for real electronic systems, LDA has proved to be remarkably accurate for a wide variety of systems.

2.6.2 Generalized Gradient Approximation

As mentioned before, the LDA treats all system as homogeneous. However, real systems are clearly inhomogeneous with spatially varying electric field, means that there is a need to find alternative approximation, which is the generalized gradient approximation (GGA). The gradient and the higher spatial derivatives of the total charge density were included in this approximation. In other words, the exchange-correlation functional depends on the density and its gradient[18,19]. There are different parameterizations that are utilized in this approximation. PBE functional is one of the most popular and reliable, which was proposed in 1996 by Perdew, Burke and Ernzherhof[18].

$$E_{xc}^{GGA}[\rho] = \int \epsilon_{xc}^{GGA}\left(\rho(r), \nabla\rho(r)\right) \rho(r)\, dr \tag{2.20}$$

where $\nabla\rho(r)$ is the gradient of the density at the point r, ϵ_{xc}^{GGA} is usually some analytic function with some free parameters that are either fitted to experiment or determined by some exact sum-rules.

LDA and GGA are the two most commonly utilised approximations for estimating exchange-correlation energies in the DFT. Several approximate exchange-correlation functionals have been proposed in the literature, which extend beyond GGA and LDA. Overall, there is no robust theory for the validity of these functionals. It is determined via testing the functional for various materials over a wide range of systems and comparing results with reliable experimental data.

2.7 SIESTA

SIESTA (Spanish Initiative for Electronic Simulations) is both a method and a computer programme implementation to perform efficient electronic structure calculations and ab initio molecular dynamics simulations of molecules and solids[4]. One of the main features of SIESTA is that it allows for the use of the standard Kohn-Sham self-consistent density functional method in the Local Density (LDA) and Generalized Gradient (GGA) Approximations, as well as in a non-local functional that includes Van der Waals (VDW) interactions. In addition, it employs norm-conserving pseudopotentials in their fully non-local form, and a linear combination of atomic orbitals (LCAO) basis set[20]. It is designed to perform efficient calculations on huge system consisting of thousands of atoms. In this thesis, all DFT calculations have been performed with SIESTA code. It is used to obtain the optimized geometries of the molecules and to explore their electronic characteristics.

2.7.1 The Pseudopotential Approximation

Even though the many-body interacting problem has been simplified into an effective non-interacting problem by utilising the Kohn-Sham equations, there is still a need for more simplification, which could be obtained by using the proposed pseudopotential approximation by Fermi in 1934 [21]. The distribution of electrons around the nucleus is generally categorised as core and valence electrons, the valence electrons occupy the outermost (partially filled) shells, but the core electrons lie within the innermost (filled) shells. It is well known that the most physical properties of solids are dependent on valence electrons to a much greater extent than on the core electrons. This can be attributed to the fact that the core electrons are spatially localised about the

nucleus, and there is a weak overlap of their wavefunctions with the core electron wavefunctions from neighbouring atoms. Therefore, the fundamental idea of the pseudopotential approximation is to remove the core electrons and replace them by an external potential known as a pseudopotential[22–24].This concept allows a significant reduction in computational efforts without missing the essential physics provided the interaction of core and valence electrons is well described by some effective Hamiltonian. The main advantage of this approach is serious reduction in the number of electrons in a system, as well as saving time and memory, which are especially important when studying compounds with a large number of core electrons such as transition metals.

2.7.2 SIESTA Basis Sets

Basis sets play an essential role in quantum physics and density functional theory, which are used to represent the electronic wavefunction. The goal of a basis set is to provide the best representation of the unknown molecular orbitals (or electron density), with as small a computational cost as possible[25]. For efficient calculations, SIESTA utilises a linear combination of atomic orbital (LCAO) basis sets, which are constrained to be zero outside of a certain radius (cut-off radius r_c)[26]. Consequently, a sparse form of the Hamiltonian is produced because the overlap between basis functions is reduced. Therefore, a minimum size basis set can create characteristics close to those of the studied system. The basis functions are constructed as a product of the numerical radial function and a spherical harmonic[4,27]. The single- ζ is considered to be the simplest form of the atomic basis set for an atom, which represents a single basis function per electron orbital, and is given as[27]:

$$\psi_{nlm}(r) = \phi_{nl}^{1}(r)\, Y_{lm}(\varphi, \vartheta) \tag{2.21}$$

Here, $n = 1,2, \ldots\ldots, l = 0, \ldots . n-1$ and $m = -l, \ldots\ldots l$ are quantum numbers, $\phi_{nl}^{1}(r)$ is the radial wavefunction and $Y_{lm}(\varphi, \vartheta)$ is a spherical harmonic wavefunction. In order to obtain a higher accuracy basis set, multiple-ζ can be included by adding another radial wavefunctions for each atomic orbital. Double-ζ basis sets (DZ) are constructed by using two basis functions for each atomic orbital. Further accuracy (multiple-ζ polarised) can be obtained by including wavefunctions with different angular momentum corresponding to orbitals, which are unoccupied in the atom[25].

2.7.3 Calculating binding energy using the counterpoise method

As mentioned above, the ground-state energy for different system configurations is calculated utilising the DFT approach, which is also used to calculate the binding energy between different parts of a system. However, performing such these calculations would not yield an accurate result, due to the localised nature of the LCOA basis sets, which are centred on the nuclei. When atoms are sufficiently close to each other, their basis functions are going to overlap. This effect, which is called the basis set superposition error (BSSE)[28–30], increases as the atoms orientate themselves closer, thereby creating an effectively varying basis set against the interatomic distance.

One obvious solution to the BSSE is the use of extremely large basis sets. This is, however, hardly feasible for the of the chemically interesting systems. The second approach is termed the counterpoise correction (CP), which is an approximate method proposed by Boys and Bernardi[30]. Assuming two molecular systems are denoted **A** and **B,** the energy of the interaction can be expressed as:

$$\Delta E(AB) = E^{AB} - (E^{A} + E^{B}) \tag{2.22}$$

where E^{AB} is the total energy for the dimer systems A and B, E^{A} and E^{B} are the energies of the isolated systems A and B. It is worth mentioning that to execute this correction in SIESTA, the ghost states (i.e., no nuclei and no electrons but empty basis set functions centred on them) have been used to evaluate the total energy of segregated systems A or B in dimer basis, with keeping the identical basis sets for three energies [31,32].

$$\Delta E(AB) = E_{AB}^{AB} - (E_{A}^{AB} + E_{B}^{AB}) \tag{2.23}$$

Where the superscript AB means the whole basis set is used, and the subscripts denote the geometry. E_{A}^{AB} and E_{B}^{AB} are the energies of systems A and B are evaluated in the basis of the dimer. This approach is an important method to eliminate the BSSE and provide reliable and realistic results for different systems[33].

2.8 Calculation in Practice

In this thesis, the SIESTA code is used to perform all the calculations, starting with constructing the geometrical configuration of the system, and choosing a suitable pseudopotential for each element, which can be distinctive for each exchange-correlation functional. Additionally, choosing an appropriate basis set for each element present in the calculation is a tradeoff between the speed of the calculation and the accuracy, which can be decided by the user. It is known that more accurate calculations need to be more computationally expensive, thus it takes a longer time and uses larger memory.

Since the energy functional can be fully calculated if the system's density is known, a trial electron density $\rho^{initial}(\vec{r})$ is considered as an initial guess at the beginning of the self-consistent field (SCF) cycle, as shown in Fig. 2.1. Then, the effective potential V_{eff} is determined, which is used

to solve the Kohn-Sham equation (2.17). This leads to find the Hamiltonian, which is then diagonalised to find the eigenfunctions and the new electron density $\rho^{\text{new}}(\vec{r})$. Hopefully, this $\rho^{\text{new}}(\vec{r})$ will be closer to the true ground state and is checked. In terms of self-consistency, if this new electron density $\rho^{\text{new}}(\vec{r})$ agrees numerically with the density $\rho^{\text{initial}}(\vec{r})$ used for constructing the Hamiltonian, then the end of the loop has been reached. The loop is then exited and all the desired converged quantities, such as the total energy, the electronic band structure, density of states etc. are calculated. Otherwise, if the new density $\rho^{\text{new}}(\vec{r})$ does not agree with the starting density $\rho^{initial}(\vec{r})$, a new input density is generated and starts another SCF cycle.

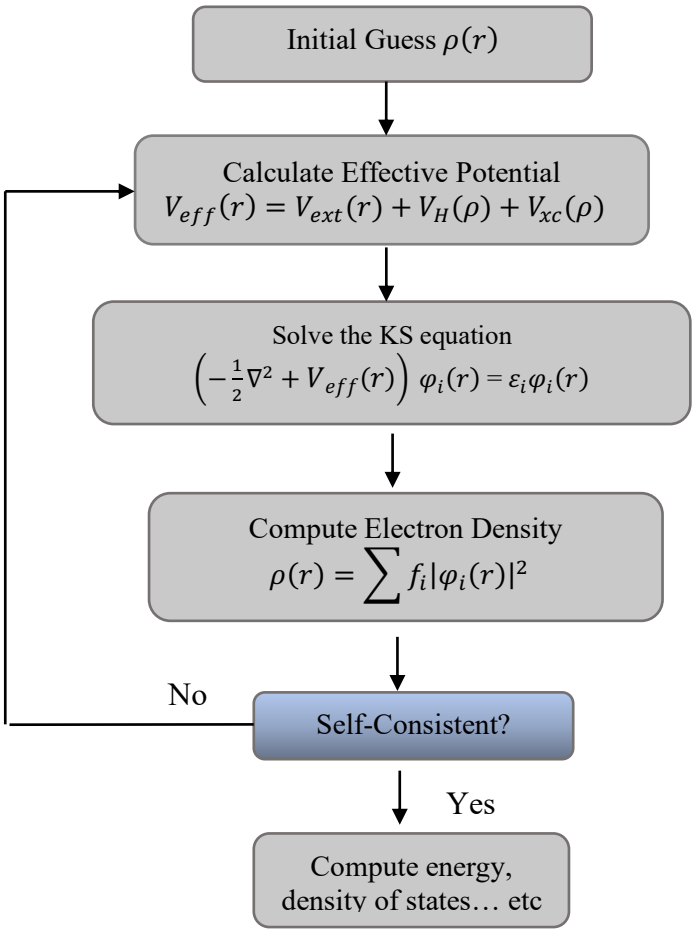

Fig. 2.1: Schematic of the self-consistency process within SIESTA.

2.9 Conclusion

I have discussed the theoretical background of density functional theory from the starting point of solving the Schrodinger equation, which was the major motivation for the development of the DFT. Besides the Born-Oppenheimer approximation of the nuclei, the two Hobenberg-Kohn theorems, and finally the Khan-Sham formalism. The functional forms of the exchange and correlation energy in the local density approximation and the generalised gradient approximation have been explained. Finally, the SIESTA implementation of DFT has been presented in some detail, and the SIESTA's components, such as the pseudopotentials approximation and Siesta basis set, have been illustrated.

2.10 Bibliography

(1) Naito, T.; Ohashi, D.; Liang, H. Improvement of Functionals in Density Functional Theory by the Inverse Kohn–Sham Method and Density Functional Perturbation Theory. *J. Phys. B At. Mol. Opt. Phys.* **2019**, *52* (24), 245003.

(2) Borgoo, A.; Godefroid, M. R.; Geerlings, P. Atomic Density Functions: Atomic Physics Calculations Analyzed with Methods from Quantum Chemistry. *ArXiv11021914 Phys.* **2011**.

(3) Bauer, G. E. W. General Operator Ground-State Expectation Values in the Hohenberg-Kohn-Sham Density-Functional Formalism. *Phys. Rev. B* **1983**, *27* (10), 5912–5918.

(4) Soler, J. M.; Artacho, E.; Gale, J. D.; García, A.; Junquera, J.; Ordejón, P.; Sánchez-Portal, D. The SIESTA Method for *Ab Initio* Order- *N* Materials Simulation. *J. Phys. Condens.*

(5) Christov, I. P. Time-Dependent Quantum Monte Carlo: Preparation of the Ground State. *New J. Phys.* **2007**, *9* (3), 70–70.

(6) Hagedorn, G. A. A Time Dependent Born-Oppenheimer Approximation. *Commun. Math. Phys.* **1980**, *77* (1), 1–19.

(7) Hohenberg, P.; Kohn, W. Inhomogeneous Electron Gas. *Phys. Rev.* **1964**, *136* (3B), B864–B871.

(8) Levy, M. Universal Variational Functionals of Electron Densities, First-Order Density Matrices, and Natural Spin-Orbitals and Solution of the *v* -Representability Problem. *Proc. Natl. Acad. Sci.* **1979**, *76* (12), 6062–6065.

(9) Burke, K. Perspective on Density Functional Theory. *J. Chem. Phys.* **2012**, *136* (15), 150901.

(10) Kohn, W.; Sham, L. J. Self-Consistent Equations Including Exchange and Correlation Effects. *Phys. Rev.* **1965**, *140* (4A), A1133–A1138.

(11) Levy, M. Electron Densities in Search of Hamiltonians. *Phys. Rev. A* **1982**, *26* (3), 1200–1208.

(12) Lieb, E. H. Thomas-Fermi and Related Theories of Atoms and Molecules. *Rev. Mod. Phys.* **1981**, *53* (4), 603–641.

(13) Slater, J. C. A Simplification of the Hartree-Fock Method. *Phys. Rev.* **1951**, *81* (3), 385–390.

(14) The Hartree-Fock Method from Self-consistency to Correct Symmetry.Webarchive.

(15) Langreth, D. C.; Perdew, J. P. Exchange-Correlation Energy of a Metallic Surface: Wave-Vector Analysis. *Phys. Rev. B* **1977**, *15* (6), 2884–2901.

(16) Bretonnet, J.-L.; Université de Lorraine, LCP-A2MC, EA 3469, 1 Bd. François Arago, Metz, F-57078, France. Basics of the Density Functional Theory. *AIMS Mater. Sci.* **2017**, *4* (6), 1372–1405.

(17) Entwistle, M. T.; Casula, M.; Godby, R. W. Comparison of Local Density Functionals Based on Electron Gas and Finite Systems. *Phys. Rev. B* **2018**, *97* (23), 235143.

(18) Perdew, J. P.; Burke, K.; Ernzerhof, M. Generalized Gradient Approximation Made Simple. *Phys. Rev. Lett.* **1996**, *77* (18), 3865–3868.

(19) Peverati, R.; Truhlar, D. G. Exchange–Correlation Functional with Good Accuracy for Both Structural and Energetic Properties While Depending Only on the Density and Its Gradient. *J. Chem. Theory Comput.* **2012**, *8* (7), 2310–2319.

(20) García, A.; Papior, N.; Akhtar, A.; Artacho, E.; Blum, V.; Bosoni, E.; Brandimarte, P.; Brandbyge, M.; Cerdá, J. I.; Corsetti, F.; Cuadrado, R.; Dikan, V.; Ferrer, J.; Gale, J.;

García-Fernández, P.; García-Suárez, V. M.; García, S.; Huhs, G.; Illera, S.; Korytár, R.; Koval, P.; Lebedeva, I.; Lin, L.; López-Tarifa, P.; Mayo, S. G.; Mohr, S.; Ordejón, P.; Postnikov, A.; Pouillon, Y.; Pruneda, M.; Robles, R.; Sánchez-Portal, D.; Soler, J. M.; Ullah, R.; Yu, V. W.; Junquera, J. S IESTA : Recent Developments and Applications. *J. Chem. Phys.* **2020**, *152* (20), 204108.

(21) Troullier, N.; Martins, J. L. Efficient Pseudopotentials for Plane-Wave Calculations. *Phys. Rev. B* **1991**, *43* (3), 1993–2006.

(22) Zunger, A.; Cohen, M. L. Self-Consistent Pseudopotential Calculation of the Bulk Properties of Mo and W. *Phys. Rev. B* **1979**, *19* (2), 568–582.

(23) Chelikowsky, J. R. The Pseudopotential-Density Functional Method Applied to Nanostructures. *J. Phys. Appl. Phys.* **2000**, *33* (8), R33–R50.

(24) Louie, S. G.; Froyen, S.; Cohen, M. L. Nonlinear Ionic Pseudopotentials in Spin-Density-Functional Calculations. *Phys. Rev. B* **1982**, *26* (4), 1738–1742.

(25) Atomic Orbital Basis Sets.Webarchive.

(26) Anglada, E.; Soler, J.; Junquera, J.; Artacho, E. Systematic Generation of Finite-Range Atomic Basis Sets for Linear-Scaling Calculations. *Phys. Rev. B* **2002**, *66* (20), 205101.

(27) Larsen, A. H.; Vanin, M.; Mortensen, J. J.; Thygesen, K. S.; Jacobsen, K. W. Localized Atomic Basis Set in the Projector Augmented Wave Method. *Phys. Rev. B* **2009**, *80* (19), 195112.

(28) Davidson, E. R.; Feller, D. Basis Set Selection for Molecular Calculations. *Chem. Rev.* **1986**, *86* (4), 681–696.

(29) Boese, A. D.; Jansen, G.; Torheyden, M.; Höfener, S.; Klopper, W. Effects of Counterpoise Correction and Basis Set Extrapolation on the MP2 Geometries of Hydrogen Bonded

Dimers of Ammonia, Water, and Hydrogen Fluoride. *Phys Chem Chem Phys* **2011**, *13* (3), 1230–1238.

(30) Haynes, P. D.; Skylaris, C.-K.; Mostofi, A. A.; Payne, M. C. Elimination of Basis Set Superposition Error in Linear-Scaling Density-Functional Calculations with Local Orbitals Optimised in Situ. *Chem. Phys. Lett.* **2006**, *422* (4–6), 345–349.

(31) Daza, M. C.; Dobado, J. A.; Molina, J. M.; Salvador, P.; Duran, M.; Villaveces, J. L. Basis Set Superposition Error-Counterpoise Corrected Potential Energy Surfaces. Application to Hydrogen Peroxide···X (X=F−, Cl−, Br−, Li+, Na+) Complexes. *J. Chem. Phys.* **1999**, *110* (24), 11806–11813.

(32) Sherrill, C. D. Counterpoise Correction and Basis Set Superposition Error. 6.

(33) van Duijneveldt, F. B.; van Duijneveldt-van de Rijdt, J. G. C. M.; van Lenthe, J. H. State of the Art in Counterpoise Theory. *Chem. Rev.* **1994**, *94* (7), 1873–1885.

Chapter 3

3. Theory of single particle transport

One of the significant issues in molecular electronics is how to connect the isolated molecule to semi-infinite leads. Such a system involves scattering processes either from the junction to leads or inside the molecule itself. There are different approaches to studying the electronic properties of such a junction. Here, I will describe the method used in the rest of this thesis based on scattering theory along with Green's function techniques.

3.1 Introduction

One of the fundamental goals of molecular electronics is to explore and understand the electronic and thermal properties of molecular junctions, which consist of a molecule attached to electrodes, so that ballistic transport takes place through its energy levels. To achieve this goal, there are some basic concepts that should be considered in order to understand the electronic properties of molecular junctions, such as the scattering process of the electrode-molecule-electrode structure. One of the most powerful methodologies to study the scattering process in the molecular bridge is the Green's function formalism.

This chapter begins with a brief overview of the tight-binding model (TBM) for the description of quantum systems. Followed by the study of one-dimensional scattering theory and Green's functions for different transport regimes. As an example, a one-dimensional structure with an arbitrary scattering region will be utilised to derive the most general formula for the transmission probability of electrons with energy E traversing from one electrode to another. In addition, the Landauer formula is presented, which is a simple expression relating the transmission probability

of the electron to the electronic conductance in a one-dimensional structure with two terminals. Finally, to understand the origin of resonances in the transmission curve, different types of resonances with different quantum interference patterns will be displayed.

3.2 Tight-binding model

The tight-binding model (TBM) or the linear combination of atomic orbitals (LCAO) method is an approach to the calculation of electronic band structure using an appropriate set of wave functions based on the superposition of wave functions of isolated atoms existing at each atomic site. The TBM assumes that electrons can interact with its nearest neighbour sites[1–3]. In reality, atomic wave function decays exponentially as distance increases. Therefore, it is a reasonable approximation to consider only the nearest neighbour interaction to describe the system. The time-dependent Schrodinger equation is given by

$$H(x)\,\Psi(x,t) = i\hbar\,\frac{\partial}{\partial t}\Psi(x,t) \tag{3.1}$$

where Ψ is the wave function of the quantum system, $\hbar$ is the reduced Planck constant ($\frac{h}{2\pi}$), and H is the Hamiltonian, which is given by:

$$H(x) = \frac{-\hbar^2}{2m}\,\nabla^2 + V(x) \tag{3.2}$$

We assume the wave function as a product of spatial and temporal terms

$$\Psi(x,t) = \phi(x)\,\theta(t) \tag{3.3}$$

The Schrodinger equation then becomes two ordinary differential equations:

$$\frac{1}{\theta(t)}\,\frac{d}{dt}\,\theta(t) = -\frac{iE}{\hbar} \tag{3.4}$$

and

$$H\,\phi(x) = E\,\phi(x) \tag{3.5}$$

The solution to equation (3.1) is

$$\Psi(x,t) = \phi(x)\, e^{\frac{-iEt}{\hbar}} \tag{3.6}$$

The most general solution is a linear combination of these solutions:

$$\Psi(x,t) = \sum_j \psi_j \ \phi_j(x)\, e^{\frac{-iEt}{\hbar}} \tag{3.7}$$

The wave function $\Psi(x)$ can be written as a linear superposition of the form:

$$\Psi(x) = \sum_j \psi_j \ \phi_j(x) \tag{3.8}$$

$\phi_j(x)$ is a localized basis function on a particular site j, and ψ_j is the time-independent amplitude of the wave function on site j, and the probability of finding an electron on site j is $\left|\psi_j\right|^2$.

The Hamiltonian matrix elements can be expressed as:

$$H_{ij} = \left\langle \phi_i(x) \middle| H \middle| \emptyset_j(x) \right\rangle = \int dx\ \phi_i^*(x) H\ \phi_j(x) \tag{3.9}$$

The following section describes the model of chain of atoms, with a single orbital on each atom. Since the electrons interact with its nearest neighbour sites, all terms $\langle \emptyset_i \mid H \mid \emptyset_j \rangle$ with $|i-j| > 1$ are small, and therefore neglected.

Picking a particular atom on site j, the time- dependent Schrodinger equation is then given by:

$$i\hbar\, \frac{\partial \psi_j}{\partial t} = \varepsilon_j\, \psi_j + H_{j,j-1}\psi_{j-1}(t) + H_{j,j+1}\psi_{j+1}(t) \tag{3.10}$$

where $\varepsilon_j = H_{jj}$ is the onsite energy of atomic orbital j.

3.2 One-dimensional (1-D) linear infinite chain

To get a qualitative understanding of electronic structure, I will start with a simple TBM, which is a one-dimensional infinite chain of identical atoms with on-site energies ε_o and real hopping parameters $-\gamma$, as illustrated in Fig. 3.1

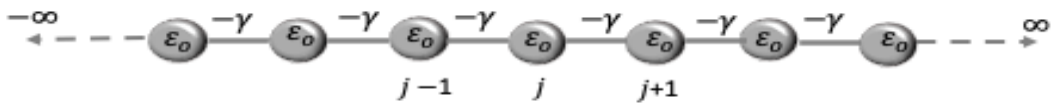

Fig. 3.1: Tight-binding model of a one-dimensional infinite crystalline chain with on-site energies ε_o and couplings $-\gamma$.

The time-independent Schrodinger equation can be written as follows:

$$H|\psi\rangle = E|\psi\rangle \tag{3.11}$$

$$\begin{pmatrix} -\infty & . & . & . & . & . & . & . & . \\ . & . & . & . & . & . & . & . & . \\ . & . & \varepsilon_\circ & -\gamma & 0 & 0 & 0 & . & . \\ . & . & -\gamma & \varepsilon_\circ & -\gamma & 0 & 0 & . & . \\ . & . & 0 & -\gamma & \varepsilon_\circ & -\gamma & 0 & . & . \\ . & . & 0 & 0 & -\gamma & \varepsilon_\circ & -\gamma & . & . \\ . & . & 0 & 0 & 0 & -\gamma & \varepsilon_\circ & . & . \\ . & . & . & . & . & . & . & . & . \\ . & . & . & . & . & . & . & . & +\infty \end{pmatrix} \begin{pmatrix} . \\ . \\ . \\ \psi_{j-1} \\ \psi_j \\ \psi_{j+1} \\ . \\ . \\ . \end{pmatrix} = E \begin{pmatrix} . \\ . \\ . \\ \psi_{j-1} \\ \psi_j \\ \psi_{j+1} \\ . \\ . \\ . \end{pmatrix} \tag{3.12}$$

Equivalently,

$$\sum_{l=-\infty}^{\infty} H_{jl}\psi_l = E\psi_j \tag{3.13}$$

The Schrodinger equation reduces to

$$\varepsilon_o\psi_j - \gamma\psi_{j+1} - \gamma\psi_{j-1} = E\psi_j \tag{3.14}$$

This equation is satisfied for all j from $-\infty$ to $+\infty$. By using Bloch's theorem, which states that the eigenstates of a crystalline chain are proportional to plane waves, we calculate the dispersion relation for this system by substituting a Bloch function $\psi_j = \frac{1}{\sqrt{v}} e^{ikj}$ (normalised eigenstate by its group velocity) into equation (3.14), which results in

$$E(k) = \varepsilon_o - 2\gamma \cos k \tag{3.15}$$

The group velocity can be obtained by:

$$v = \frac{1}{\hbar}\frac{\partial E}{\partial k} = \frac{2\gamma \sin k}{\hbar} \tag{3.16}$$

Since k is the wavenumber, which is a continuous variable between - π and π (to avoid including the linearly dependent eigenstates). The energy levels in the infinite system form a continuous band of energies, and the bandwidth is proportional to the hopping integral (4γ), as shown in Fig. 3.2.

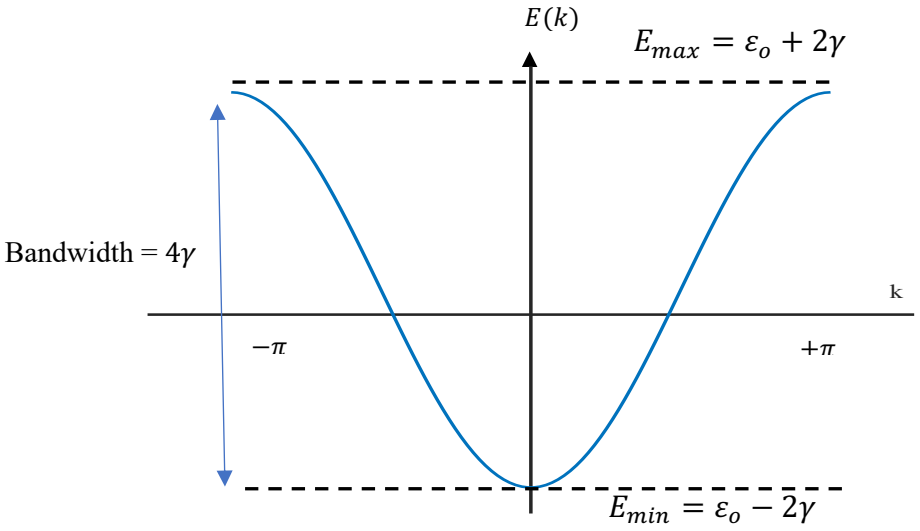

Fig. 3.2: The dispersion relation of infinite linear chain.

3.3 One-Dimensional Scattering Theory

This section starts with the bond current, which is the current passing through the bond between two atomic orbitals, and then goes to how to solve the Schrodinger equation by adding one impurity to the system, leading to the definition of the scattering matrix.

3.3.1 Bond currents and conservation of probability

Consider a one-dimensional infinite chain, in which all site energies ε_j and bonds $-\gamma_j$ are arbitrary, as shown in Fig. 3.3. In this case, the Hamiltonian matrix elements are $H_{jj} = \varepsilon_j$ and $H_{j,j+1} = -\gamma_j$.

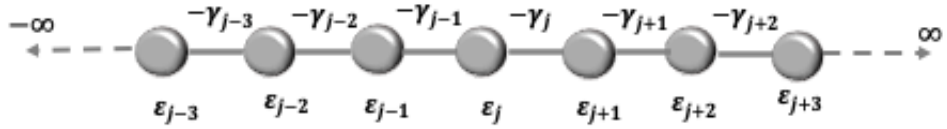

Fig. 3.3: Tight-binding model of a one-dimensional chain, in which all the site energies and bonds are arbitrary.

The time-dependent Schrodinger equation is:

$$i\hbar \frac{d}{dt}|\psi(t)\rangle = H|\psi(t)\rangle \tag{3.17}$$

Picking a particular atom at site j, equation (3.17) can be rewritten as:

$$i\hbar \frac{d}{dt}\psi_j(t) = \sum_i H_{ji}\psi_i(t)$$

Or equivalently

$$i\hbar \frac{d}{dt}\psi_j(t) = \varepsilon_j\, \psi_j(t) + H_{j,j-1}\psi_{j-1}(t) + H_{j,j+1}\psi_{j+1}(t) \tag{3.18}$$

The probability for finding an electron on this site in time t is:

$$P_j(t) = \left|\psi_j(t)\right|^2 = \psi_j(t)\psi_j^*(t) \tag{3.19}$$

In what follows, I will obtain the expression of the rate of change in occupation probability on site j at time t.

$$i\hbar \frac{d}{dt}\, P_j(t) = i\hbar \left[\psi_j(t)\, \frac{d}{dt}\psi_j^*(t) + \psi_j^*(t)\, \frac{d}{dt}\psi_j(t)\right] \tag{3.20}$$

Hence,

$$\frac{d}{dt}\, P_j(t) = J_{j-1\to j} - J_{j\to j+1} \tag{3.21}$$

where $J_{j-1\to j}$ is the bond current from site $j-1$ to site j, $J_{j\to j+1}$ is the bond current from site j to site $j+1$, which can be expressed as:

$$J_{j-1\to j} = \frac{i}{\hbar}\left[H^*_{j-1,j}\,\psi_j(t)\psi^*_{j-1}(t) - H_{j-1,j}\,\psi^*_j(t)\,\psi_{j-1}(t)\right] \tag{3.22}$$

$$J_{j\to j+1} = \frac{i}{\hbar}\left[H_{j,j+1}\,\psi^*_j(t)\,\psi_{j+1}(t) - H^*_{j,j+1}\,\psi_j(t)\psi^*_{j+1}(t)\right] \tag{3.23}$$

Equation (3.21) is a law of conservation of probability, which means that the rate of change of the site occupation probability is equal to the current in minus the current out.

Since $H^*_{j,j-1} = H_{j-1,j}$, equation (3.22) can be written as:

$$J_{j-1\to j} = \frac{i}{\hbar}\left[H_{j-1,j}\;\psi_j(t)\,\psi^*_{j-1}(t) - H^*_{j-1,j}\,\psi^*_j(t)\,\psi_{j-1}(t)\right] \tag{3.24}$$

By replacing j by $j-1$ in equation (3.23), the expression for $J_{j-1\to j}$ is obtained, which means equations (3.23) and (3.24) are mutually consistent. Since $H_{j,j+1} = -\gamma_j$, the bond current from site j to $j+1$ can be expressed as:

$$J_{j\to j+1} = \frac{2}{\hbar}\, Im\left[\gamma_j\psi^*_j(t)\,\psi_{j+1}(t)\right] \tag{3.25}$$

3.3.2 Transport for crystalline chain with a single impurity

It is useful to calculate the scattering matrix for a simple structure by adding a single impurity with on-site energy ε_1 between two semi-infinite one-dimensional crystalline leads, as shown in Fig. 3.4.

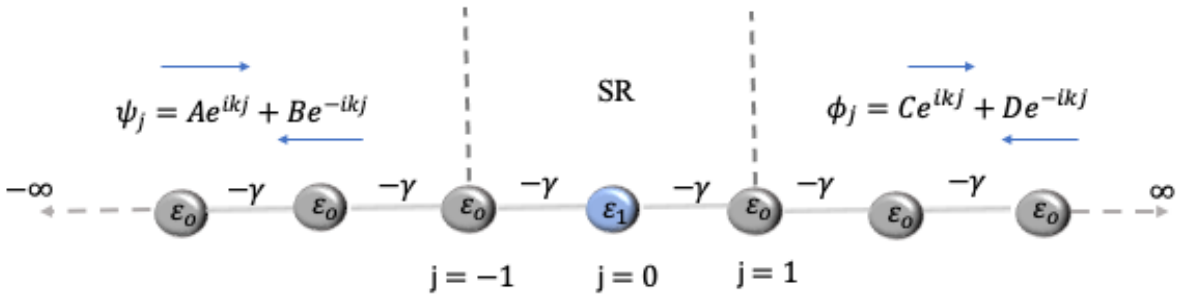

Fig. 3.4: Tight-binding model of one-dimensional crystalline chain with a single impurity at site $j = 0$.

Based on the tight-binding model, in this system, the Hamiltonian and eigenvectors are as follows:

$$\begin{pmatrix} -\infty & . & . & . & . & . & . & . & . \\ . & . & . & . & . & . & . & . & . \\ . & . & \varepsilon_\circ & -\gamma & 0 & 0 & 0 & . & . \\ . & . & -\gamma & \varepsilon_\circ & -\gamma & 0 & 0 & . & . \\ . & . & 0 & -\gamma & \varepsilon_1 & -\gamma & 0 & . & . \\ . & . & 0 & 0 & -\gamma & \varepsilon_\circ & -\gamma & . & . \\ . & . & 0 & 0 & 0 & -\gamma & \varepsilon_\circ & . & . \\ . & . & . & . & . & . & . & . & . \\ . & . & . & . & . & . & . & . & +\infty \end{pmatrix} \begin{pmatrix} . \\ . \\ . \\ \psi_{-1} \\ \psi_0 \\ \psi_1 \\ . \\ . \\ . \end{pmatrix} = E \begin{pmatrix} . \\ . \\ . \\ \psi_{-1} \\ \psi_0 \\ \psi_1 \\ . \\ . \\ . \end{pmatrix} \tag{3.26}$$

The Schrodinger equations for this structure take the following forms:

$\varepsilon_o\psi_j - \gamma\psi_{j-1} - \gamma\psi_{j+1} = E\psi_j$ for j ≤-2 (3.27)

$\varepsilon_o\psi_{-1} - \gamma\psi_{-2} - \gamma f_o = E\psi_{-1}$ for j = -1 (3.28)

$\varepsilon_1 f_o - \gamma\psi_{-1} - \gamma\phi_1 = Ef_o$ for j =0 (3.29)

$\varepsilon_o\phi_1 - \gamma f_o - \gamma\phi_2 = E\phi_1$ for j =1 (3.30)

$\varepsilon_o\phi_j - \gamma\phi_{j-1} - \gamma\phi_{j+1} = E\phi_j$ for j ≥ 2 (3.31)

where ψ_j and ϕ_j indicate the eigenvector amplitudes to the left and right of the impurity, respectively, and f_o is the amplitude on the impurity.

For j ≤ -2, where the system is crystalline chain the solution to equation (3.27) is as follows:

$$\psi_j = Ae^{ikj} + Be^{-ikj} \tag{3.32}$$

Similarly, for j ≥ 2, the solution to equation (3.31) is the following:

$$\phi_j = Ce^{ikj} + De^{-ikj} \tag{3.33}$$

where A, B, C and D are arbitrary constants. The eigenvalues of this system can be obtained by substituting equations (3.32) and (3.33) into (3.27) and (3.31):

$$E(k) = \varepsilon_o - 2\gamma \cos k \tag{3.34}$$

Function ψ_j has the mathematical property that it satisfies equation (3.27) for all j. For example, for $j = -1$, it yields

$$f_o = \psi_o = A + B \tag{3.35}$$

Similarly, ϕ_j satisfies equation (3.31) for all j. For example, for $j = -1$, it yields

$$f_o = \phi_o = C + D \tag{3.36}$$

Subsequently, equation (3.29) can be written as follows:

$$\varepsilon_1 \phi_o - \gamma \psi_{-1} - \gamma \phi_1 = E\phi_o \tag{3.37}$$

Hence (3.35) and (3.36) yield the following:

$$A + B = C + D \tag{3.38}$$

As mentioned above, ϕ_j satisfies equation (3.31) for all j, and setting $j = 0$ gives the following:

$$\varepsilon_o\phi_o - \gamma\phi_{-1} - \gamma\phi_1 = E\phi_o \tag{3.39}$$

The comparison of equation (3.37) and (3.39) yields

$$(\varepsilon_1 - \varepsilon_o)\phi_o - \gamma(\psi_{-1} - \phi_{-1}) = 0 \tag{3.40}$$

By choosing $A = 1,\ B = r,\ C = t,\ D = 0$, we find $t = 1 + r$, and substituting $\phi_o, \psi_{-1}, \phi_{-1}$ into (3.40) yields

$$t = \frac{1}{1-\alpha} \tag{3.41}$$

$$r = \frac{\alpha}{1-\alpha} \tag{3.42}$$

where $$\alpha = \frac{\varepsilon_1 - \varepsilon_o}{2\gamma i sin k} \tag{3.43}$$

t and r are the transmission and reflection amplitudes respectively. To obtain the definition of the scattering matrix, if t and r are the transmission and reflection amplitudes associated with an incoming plane wave from the left, and similarly t' and r' are the amplitudes of transmitted and reflected waves due to the incoming wave from the right, collecting these amplitudes produces a scattering matrix

$$S = \begin{pmatrix} r & t' \\ t & r' \end{pmatrix} \tag{3.44}$$

As an example, for the single impurity problem

$$S = \frac{1}{1-\alpha}\begin{pmatrix} \alpha & 1 \\ 1 & \alpha \end{pmatrix}$$

Note that S is a unitary matrix, i.e., $SS^{\dagger} = S^{\dagger}S = I$. As a result, the sum of transmission and reflection probabilities is unity.

$$R(E) + T(E) = 1 \tag{3.45}$$

where,

$$T(E) = |t|^2 = \frac{1}{(1+|\alpha|^2)} \tag{3.46}$$

$$R(E) = |r|^2 = \frac{|\alpha|^2}{(1+|\alpha|^2)} \tag{3.47}$$

3.4 The Landauer Formula

Fig. 3.5: A scattering region connected to two electrodes, which in turn are attached to two reservoirs with chemical potential μ_L and μ_R.

The Landauer formula is the standard theoretical model used to describe ballistic transport in a mesoscopic system[3–6]. It relates the transmission coefficient of the electron to the electronic conductance through one-dimensional structures with two terminals. To derive this formula, consider a system consisting of a scattering region (the ring model of N sites with periodic boundary conditions, in which each atom possesses a single site of energy ε_o with nearest neighbour couplings $-\gamma$) connected to two electrodes (leads), as shown in Fig. 3.5. For this model, the normalised eigenstates are $\psi_j{}^n = \frac{1}{\sqrt{N}} e^{ik_n j}$, where $k_n = \frac{2n\pi}{N}$. This shows that the number of

states with positive velocity per unite energy, that is called the density of states, is $\frac{\Delta n}{\Delta E} = \frac{N}{h v_k}$, and the current carried by each state is $\frac{v_k}{N}$. Thereby, the total current by the states in the energy interval ΔE is $\frac{1}{h}\,\Delta E$ (i.e., the current per unit energy is independent of k). Since each state is occupied by two electrons (one spin up and the other spin down), then

$$\Delta I = \frac{2}{h}\,\Delta E \qquad \text{for both spins} \tag{3.47}$$

To study a real device, two ideal reservoirs located on the left and right of a scatterer are considered, which feed electrons of energy E into the electrodes. They fill all the left and right-moving states with an occupancy determined by the Fermi function $f_L(E)$ and $f_R(E)$ of the left and right leads, respectively. Therefore, the number of electrons per unit time, in an energy interval ΔE, incident on the scatterer from the left and right reservoirs is $\Delta I_L = \frac{2}{h}\, f_L(E)\Delta E$ and $\Delta I_R = \frac{2}{h}\, f_R(E)\Delta E$, respectively. As shown in Fig. 3.5, electrons from the left reservoir can transmit into the right lead through the scattering region and electrons from the right reservoir can reflect into the right lead, the net electron current in the right lead is

$$\Delta I = T(E)\,\Delta I_L - \big(1 - R(E)\big)\,\Delta I_R \tag{3.48}$$

Since

$$R(E) + T(E) = 1$$

$$I = \frac{2}{h}\,[f_L(E) - f_R(E)]\,T(E)\Delta E \tag{3.49}$$

where $T(E)$ and $\mathrm{R}(E)$ are the transmission and reflection coefficients. $f_L(E)$ and $f_R(E)$ are Fermi-Dirac distribution functions of the left and right reservoirs, which have the following form:

$$f_L(E) = \left[e^{\beta(E-E_F^L)+1}\right]^{-1} \tag{3.50}$$

$$f_R(E) = \left[e^{\beta(E-E_F^R)+1}\right]^{-1} \tag{3.51}$$

Here $\beta = \frac{1}{k_B T}$, where T is the temperature and k_B is Boltzmann's constant. E_F^L(E_F^R) is the Fermi energy of the left (right) reservoir. After integrating over all energies, the total electrical current entering the right reservoir is:

$$I = \frac{2e}{h}\int_{-\infty}^{\infty} dE\ T(E)\,[f_L(E) - f_R(E)] \tag{3.52}$$

where e is the electron charge. This equation is called the Landauer formula, and it is clear that $I = 0$ when $f_L(E) = f_R(E)$ because only differences in the distributions contribute to the current. If applying the bias voltage on the left and right reservoirs, then $E_F^L = E_F + \frac{eV}{2}$, $E_F^R = E_F - \frac{eV}{2}$ .This means that at zero temperature, but finite voltage:

$$I = \frac{2e}{h}\int_{E_F-\frac{eV}{2}}^{E_F+\frac{eV}{2}} dE\ T(E) \tag{3.53}$$

If $T(E)$ does not vary significantly over an energy range, then the Fermi-Dirac functions can be Taylor expanded around the Fermi energy, thus the electrical conductance in the zero-voltage and finite temperature is:

$$G = \frac{I}{V} = G_o \int_{-\infty}^{\infty} dE\ T(E)\left[-\frac{df(E)}{dE}\right] \tag{3.54}$$

The quantity $-\frac{df(E)}{dE}$ is a normalised probability distribution of width approximately k_BT, G_o is the quantum of conductance

$$G_o = \frac{2e^2}{h} \approx 77\ \mu S \tag{3.55}$$

In the limit of zero voltage and zero temperature, the conductance is proportional to the transmission coefficient evaluated at Fermi energy.

$$G = G_o T(E_F) \tag{3.56}$$

3.5 Green's Functions

Green's function is a powerful mathematical tool for studying the properties of nano-scale structures because it can be used to express all the observable properties of the system of interest. It is physical response due to a single point source in a periodic lattice. In other words, Green's function is the impulse response of the Schrodinger equation. Therefore, Green's function naturally carries all information about the wave-function evolution from one point to the other in a system[7,8]. In this section, I will focus how to construct the Green's function for some systems.

3.5.1 Green's function of a doubly infinite chain

In what follows, I will derive the Green's function of the one-dimensional doubly infinite linear chain, as shown in Fig. 3.6.

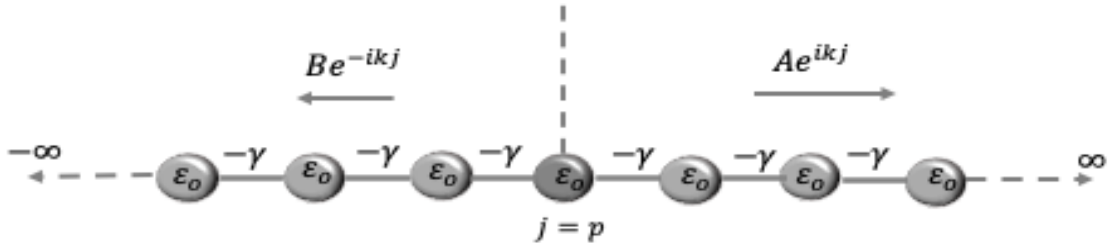

Fig. 3.6: Tight-binding representation of one-dimensional infinite chain with on-site energies ε_o and couplings $-\gamma$.

The general definition of the Green's function $G(E)$ belonging to a Hamiltonian H is:

$$(EI - H)G(E) = I \tag{3.57}$$

where I is the unit matrix

The solution to this equation can be written as:

$$G(E) = (E - H)^{-1} \tag{3.57}$$

Where G_{jp} is the retarded Green's function describes the response of a system[3] at point j due to a source at p. To highlight the relationship between Green's functions and wavefunctions, it is helpful to present the following notation:

$$G_{jp} = \psi_j^{(p)} \tag{3.59}$$

where G_{jp} is Green's matrix element belonging to the p^{th} column and j^{th}row, $\psi_j^{(p)}$ is the amplitude of column vector $\psi^{(p)}$ on site j .

Equation (3.57) can be written as

$$\sum_{l=-\infty}^{\infty}(EI - H)_{jl}G_{lp}(E) = \delta_{jp} \tag{3.60}$$

or equivalently

$$\sum_{l=-\infty}^{\infty} H_{jl}\, G_{lp}(E) = EG_{jp}(E) - \delta_{jp} \tag{3.61}$$

where δ_{jp} is Kronecker delta satisfying $\delta_{jp} = 1$ if $j = p$ and $\delta_{jp} = 0$ if $j \neq p$.

Substituting equation (3.59) into equation (3.61), yields:

$$\sum_{l=-\infty}^{\infty} H_{jl}\ \psi_l^{(p)} = E\psi_j^{(p)} - \delta_{jp} \tag{3.62}$$

This is almost identical to Schrodinger equation, except the presence of the Kronecker delta on the right-hand side, equation (3.62) can be written as:

$$\varepsilon_o\, \psi_j^{(p)} - \gamma\psi_{j-1}^{(p)} - \gamma\psi_{j+1}^{(p)} = E\psi_j^{(p)} - \delta_{jp} \tag{3.63}$$

I guess the solution to equation (3.63) is:

$$\psi_j^{(p)} = \phi_j\ = A\, e^{ikj} \quad \text{for} \quad j > p \tag{3.64}$$

$$\psi_j^{(p)} = f_j\ = B\, e^{-ikj} \quad \text{for} \quad j < p \tag{3.65}$$

For $j = p + 1$, equations (3.63) and (3.64) yield

$$\varepsilon_o\, \phi_{p+1} - \gamma\psi_p^{(p)} - \gamma\phi_{p+2} = E\phi_{p+1} \tag{3.66}$$

Since ϕ_j satisfies equation (3.62) for all values of j, this yields

$$\varepsilon_o\, \phi_{p+1} - \gamma\ \phi_p - \gamma\phi_{p+2} = E\phi_{p+1} \tag{3.67}$$

Comparing equations (3.66) and (3.67), gives

$$\psi_p^{(p)} = \phi_p \tag{3.68}$$

The same procedure is used for $j = p - 1$, which results in

$$\psi_p^{(p)} = f_p \tag{3.69}$$

Hence, equations (3.68) and (3.69) yield the following:

$$\psi_p^{(p)} = \phi_p = f_p \tag{3.70}$$

$A\, e^{ikp} = B\, e^{-ikp}$, which yields $A\ = C\, e^{-ikp}$ and $B = C\, e^{ikp}$, hence

$$\phi_j = Ce^{ik(j-p)} \text{ and } f_j = Ce^{-ik(j-p)} \tag{3.71}$$

where C is a constant. By combining these with equations (3.64) and (3.65) yields

$$\psi_j^{(p)} = Ce^{ik|j-p|} \tag{3.72}$$

To determine the value of the constant C, equation (3.63) is satisfied for the case $j = p$, thus

$$C = \frac{1}{2i\gamma \sin k} = \frac{1}{i\hbar v(E)} \tag{3.73}$$

where $v(E)$ is the group velocity. Thus, the retarded Green's function, which describes the two outgoing waves from the source p, is given by:

$$G_{jp}(E) = \psi_j^{(p)} = \frac{e^{ik|j-p|}}{i\hbar v(E)} \tag{3.74}$$

It is worth mentioning that equation (3.74) is not the most general solution, because any solution of the Schrodinger equation could be added to $\psi_j^{(p)}$. Therefore, the most general solution is:

$$G_{jp}(E) = \psi_j^{(p)} = \frac{e^{ik|j-p|}}{i\hbar v(E)} + Ae^{ikj} + Be^{-ikj} \tag{3.75}$$

where A and B are arbitrary constants, choosing $A = -\frac{e^{ik(j-p)}}{i\hbar v}$ and $B = -\frac{e^{-ik(j-p)}}{i\hbar v}$, the Green's function is obtained, which is called advanced Green's function (the complex conjugate of the retarded Green's function).

$$G_{jp}(E) = \psi_j^{(p)} = -\frac{e^{-ik(E)|j-p|}}{i\hbar v(E)} \tag{3.76}$$

3.5.2 Green's function of a semi-infinite linear chain

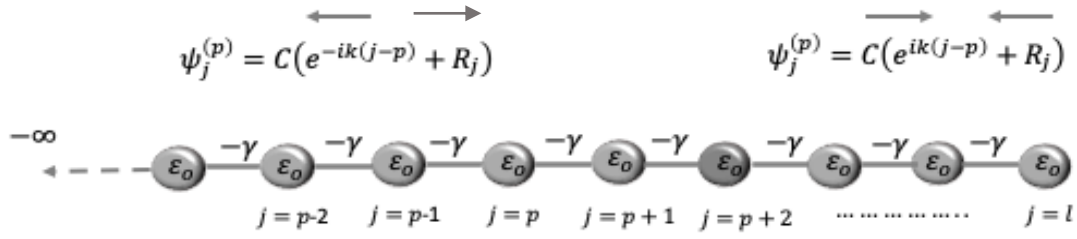

Fig. 3.7: A semi-infinite linear chain with site energies ε_o and hopping elements $-\gamma$, which terminates at site $j = l$.

To derive the Green's function of a semi-infinite chain, consider the semi-infinite chain with site energies ε_o and hopping elements $-\gamma$, as shown in Fig.3.7, in which the chain terminates at site $j = l$, where $l \geq p$. This leads to the following boundary condition

$$\psi_{l+1}^{(p)} = 0 \tag{3.77}$$

Fig. 3.7 shows the reflected plane wave e^{-ikj} will be created due to the hitting of the incoming plane wave e^{ikj} to the end of the chain. Therefore, the reflected wave will be added to the retarded Green's function

$$G_{jp}(E) = \frac{e^{ik|j-p|}}{i\hbar v(E)} + \mathrm{B}\, e^{-ikj} \tag{3.78}$$

where $$B = -\frac{e^{ik(2l+2-p)}}{i\hbar v(E)}$$

Hence, the retarded Green's function takes the following form:

$$G_{jp}(E) = \psi_j^{(p)} = \frac{e^{ik|j-p|} - e^{-ik(j+p-2l-2)}}{i\hbar v(E)} \tag{3.79}$$

On the other hand, if the chain terminates at site $l \leq p$, the boundary condition becomes

$$\psi_{l-1}^{(p)} = 0$$

Thus, the Green's function is:

$$G_{jp}(E) = \psi_j^{(p)} = \frac{e^{ik|j-p|} - e^{ik(j+p-2l+2)}}{i\hbar v(E)} \tag{3.80}$$

The Green's function on the terminal site $j = l$ due to the source at site $p = l$ is:

$$G_{ll}(E) = -\frac{e^{ik(E)}}{\gamma} \tag{3.81}$$

which is called the surface Green's function.

3.5.3 Green's function of a finite one-dimensional chain

To derive the Green's function of a finite one-dimensional chain, consider a linear chain of N tight-binding sites with free-end boundary conditions, as shown in Fig. 3.8. Therefore, Green's function should vanish at site $j = 0$ and site $j = N + 1$.

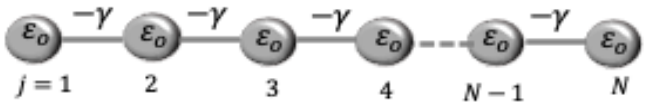

Fig. 3.8: A finite one-dimensional chain with on-site energies ε_o and hopping elements $-\gamma$.

To achieve that, Green's function should take the following expressions:

$$G_{jp}(E) = \begin{cases} A \sin kj & , \quad j \leq p \\ B \sin k[j - (N+1)] & , \quad j \geq p \end{cases} \tag{3.82}$$

So, the boundary conditions will be satisfied, and the continuity at $j = p$ yields

$$A \sin kp = B \sin k[p - (N+1)]$$

The constants A and B must be chosen as:

$$A = C \sin k[p - (N+1)] \text{ and } B = C \sin kp \tag{3.83}$$

where C is a constant

Hence, equation (3.82) can be rewritten as:

$$G_{jp}(E) = \begin{cases} C \sin k[p - (N+1)] \sin kj & for \quad j \leq p \\ C \sin kp \sin k[j - (N+1)] & for \quad j \geq p \end{cases} \tag{3.84}$$

Then C can be obtained as:

$$C = \frac{1}{\gamma \sin k \sin k(N+1)} \tag{3.85}$$

From equation (3.85), it is clear that the Green's function diverges when $\sin k(E)\,(N+1)=0$, i.e., when $k(E)=n\pi/(N+1)$, where n is an integer. At the gap centre $E=0$, where $k=\frac{\pi}{2}$, C diverges when N is odd. For even N (i.e., $N=2n$), the magic number table can be expressed as:

$$M_{jp}=\frac{G_{jp}(o)}{C} \tag{3.86}$$

$$\Rightarrow M_{jp}=\begin{cases}(-1)^{n+1}\sin\frac{\pi j}{2}\cos\frac{\pi p}{2}, & j\le p\\ (-1)^{n+1}\sin\frac{\pi p}{2}\cos\frac{\pi j}{2}, & j\ge p\end{cases} \tag{3.87}$$

This means that $M_{jp}=0$ if j and p are both odd or both even. Furthermore, for $j\le p$, $M_{jp}=0$ if j is even or p is odd and for $j\ge p$, $M_{jp}=0$ if p is even or j is odd. Otherwise, $|M_{jp}|$=1.

3.6 Transport through an arbitrary scattering region

To calculate the most general formula for the transmission coefficient of an arbitrary scattering region, I consider the structure shown in Fig. 3.9, which consists of two semi-infinite chains, in which the site energies and hopping elements in the left (right) lead are $\varepsilon_l(\varepsilon_R)$ and $-\gamma_l(-\gamma_R)$, respectively. The leads are connected to the scattering region at sites 1 and N by coupling $-\alpha$ and $-\beta$.

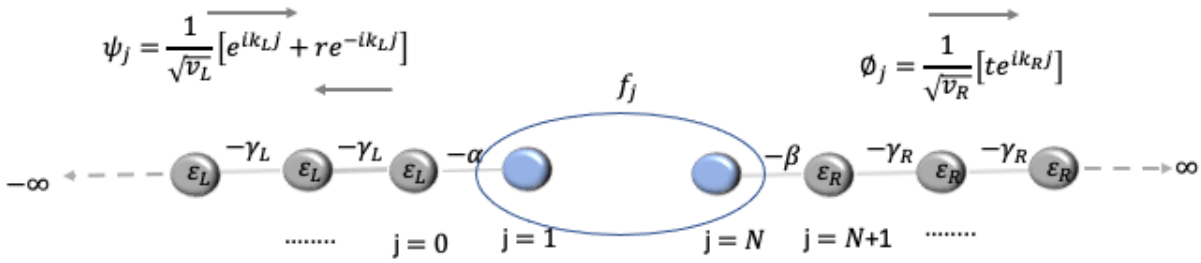

Fig. 3. 9: Tight-binding representation of an arbitrary scattering region attached to (1-D) leads.

Our aim is to solve the Schrodinger equation

$$\sum_{l=-\infty}^{\infty} H_{jl}\psi_l = E\psi_j$$

The eigenvector amplitudes will be denoted by ψ_j for the left lead, ϕ_j for the right lead and f_j for the scattering region, in which the plane waves are normalized to unit current:

$$\psi_j = \frac{1}{\sqrt{v_L}}\left[e^{ik_L j} + re^{-ik_L j}\right] \tag{3.88}$$

$$\phi_j = \frac{1}{\sqrt{v_R}}\left[te^{ik_R j}\right] \tag{3.89}$$

The Schrodinger equation for this structure takes the following form:

$$\varepsilon_L\psi_j - \gamma_L\psi_{j-1} - \gamma_L\psi_{j+1} = E\psi_j \qquad \text{for } j < 0 \tag{3.90}$$

$$\varepsilon_L\psi_o - \gamma_L\psi_{-1} - \alpha f_1 = E\psi_o \qquad \text{for } j = 0 \tag{3.91}$$

$$\sum_{l=1}^{N} H_{jl}f_l - \alpha\psi_o\delta_{j1} - \beta\phi_{N+1}\delta_{jN} = E\, f_j \qquad \text{for } 1 \le j \le N \tag{3.92}$$

$$\varepsilon_R\phi_{N+1} - \gamma_R\phi_{N+2} - \beta f_N = E\phi_{N+1} \qquad \text{for } j = N+1 \tag{3.93}$$

$$\varepsilon_R\phi_j - \gamma_R\phi_{j+1} - \gamma_R\phi_{j-1} = E\phi_j \qquad \text{for } j > N+1 \tag{3.94}$$

Equation (3.92) could be re-written as:

$$|f\rangle = g|s\rangle \tag{3.95}$$

where

$$g = (EI - H)^{-1}$$

g is the Green's function of an isolated scatterer. $|s\rangle$ is called the source which is a zero vector with non-zero elements in the connection points only (at site j=1 and $j = N$).

$$|f\rangle = \begin{pmatrix} f_1 \\ f_2 \\ . \\ . \\ f_N \end{pmatrix} \qquad |s\rangle = \begin{pmatrix} -\alpha\psi_o \\ o \\ o \\ o \\ -\beta\phi_{N+1} \end{pmatrix}$$

For the junction shown in Fig. 3.9, $|f\rangle$ has only two non-zero elements due to the source. Thus, equation (3.95) can be written as:

$$\begin{pmatrix} f_1 \\ f_N \end{pmatrix} = \begin{pmatrix} g_{11} & g_{1N} \\ g_{N1} & g_{NN} \end{pmatrix} \begin{pmatrix} -\alpha\psi_o \\ -\beta\phi_{N+1} \end{pmatrix} \tag{3.96}$$

$$\tilde{g}^{-1} \begin{pmatrix} f_1 \\ f_N \end{pmatrix} = \begin{pmatrix} -\alpha\psi_o \\ -\beta\phi_{N+1} \end{pmatrix} \tag{3.97}$$

where $\tilde{g}^{-1}$ is the inverse of the 2×2 sub matrix of Green's function.

By using the recurrence relation, we obtain the following:

$$\gamma_L \psi_1 = \alpha f_1$$

$$\gamma_R \phi_N = \beta f_N$$

From equations (3.88) and (3.89), we find

$$\phi_{N+1} = \phi_N e^{ik_R} \tag{3.98}$$

$$\psi_1 = \frac{1}{\sqrt{v_L}} [2i \sin k_L] + \psi_o e^{-ik_L} \tag{3.99}$$

Hence,

$$\begin{pmatrix} -\alpha\psi_o \\ -\beta\phi_{N+1} \end{pmatrix} = \Sigma \begin{pmatrix} f_1 \\ f_N \end{pmatrix} + \begin{pmatrix} \frac{\alpha\, e^{ik_L}}{\sqrt{v_L}} [2i \sin k_L] \\ 0 \end{pmatrix} \tag{3.100}$$

where

$$\Sigma = \begin{pmatrix} \Sigma_L & O \\ O & \Sigma_R \end{pmatrix}$$

$\Sigma_L = \frac{-\alpha^2 e^{ik_L}}{\gamma_L}$, $\Sigma_R = \frac{-\beta^2 e^{ik_R}}{\gamma_R}$ are the self-energies associated with the left and right leads, respectively. Substituting equation (3.100) into equation (3.97) yields

$$((\tilde{g})^{-1} - \Sigma) \begin{pmatrix} f_1 \\ f_N \end{pmatrix} = \begin{pmatrix} \frac{\alpha\, e^{ik_L}}{\sqrt{v_L}} [2i \sin k_L] \\ 0 \end{pmatrix} \tag{3.101}$$

Hence,

$$\begin{pmatrix} f_1 \\ f_N \end{pmatrix} = G \begin{pmatrix} \frac{\alpha\, e^{ik_L}}{\sqrt{v_L}}[2i \sin k_L] \\ 0 \end{pmatrix} \tag{3.102}$$

where

$$G = ((\tilde{g})^{-1} - \Sigma\,)^{-1} = \begin{pmatrix} G_{11} & G_{12} \\ G_{N1} & G_{NN} \end{pmatrix} \tag{3.103}$$

From equation (3.102),

$$f_N = G_{N1}\ \frac{\alpha e^{ik_L}}{\sqrt{v_L}}\ [2i \sin k_L] = \frac{\gamma_R}{\beta}\ \phi_N \tag{3.104}$$

Since $\emptyset_N = \frac{1}{\sqrt{v_R}}\left[te^{ik_R N}\right]$, $\hbar v_R = 2\gamma_R \sin k_R$ and $\hbar v_L = 2\gamma_L \sin k_L$, I obtain the following:

$$t = iG_{N1}\alpha\ \beta e^{ik_L}\sqrt{\frac{2 \sin k_L}{\gamma_L}}\quad \sqrt{\frac{2 \sin k_R}{\gamma_R}}\quad e^{-ik_R N} \tag{3.105}$$

$$T(E) = |\ t\ |^2 = 4\left[\frac{\alpha^2 \sin k_L}{\gamma_L}\right]\left[\frac{\beta^2 \sin k_R}{\gamma_R}\right]\ |G_{N1}|^2 \tag{3.106}$$

Since $$|G_{N1}|^2\ = \left|\frac{g_{N1}}{\Delta}\right|^2$$

where $$\Delta = 1 - g_{11}\,\Sigma_L - \ g_{NN}\,\Sigma_R + \Sigma_L\,\Sigma_R[g_{11}\ g_{NN} - g_{1N}\ g_{N1}]$$

The transmission probability is

$$T(E) = |\ t\ |^2 = 4\left[\frac{\alpha^2 \sin k_L}{\gamma_L}\right]\left[\frac{\beta^2 \sin k_R}{\gamma_R}\right]\ \left|\frac{g_{N1}}{\Delta}\right|^2 \tag{3.107}$$

This equation is the most general formula used to calculate the transmission probability of any scattering region that is connected to different one-dimensional leads[3].

3.7 Basic features of the transport curve

The key feature of electron transport through single molecules and phase-coherent nanostructures is emergence of transport resonance and anti-resonance associated with quantum interference[9–13] . To gain a broad understanding of the properties of these resonances, it will be useful to briefly study some kinds of resonances including; Breit-Wigner resonance[3,6,14] and Fano- resonance[15–19].

3.7.1 Breit-Wigner Resonance

Quantum interference between different paths of electrons gives rise to resonances or anti-resonances in the transmission function. The constructive interference of electrons passing through a single molecular orbital can be expressed by the Breit-Wigner formula (the Lorentzian function)[6]:

$$T(E) = \frac{4\,\Gamma_L\,\Gamma_R}{(E-\varepsilon_n)^2+(\Gamma_L+\Gamma_R)^2} \tag{3.108}$$

where $T(E)$ is the transmission coefficient of the electrons, Γ_L and Γ_R describe the coupling of the molecular orbital to the electrodes. It is worth noting that Γ controls the width of the resonance, which means that if the couplings to the electrodes (α and β) are small, the resonances will become narrow, as shown in Fig. 3.10. $\varepsilon_n = E_n - \sigma$ is an eigenvalue E_n of the molecular orbital shifted slightly by an amount σ due to the coupling of the orbital to the electrodes[6]. The transmission coefficient $T(E)$ has the maximum value $T(E)$ =1 at $E = \varepsilon_n$, in the case of a symmetric molecule is attached symmetrically to identical electrodes ($\Gamma_L = \Gamma_R$), as shown in Fig.3.11. In contrast, when the junction is asymmetric (e.g., $\Gamma_L \gg \Gamma_R$), the transmission function has the value $T(\varepsilon_n) = \frac{4\Gamma_R}{\Gamma_L}$, which is much less than unity. In other words, the on-resonance transmission coefficient of asymmetric junction is lower than that of symmetric junctions. It is worth mentioning that this formula applies when the energy of the electron is close to an eigenvalue of the isolated molecule, and when the energy level spacing of the molecule δ is larger than the width of the resonance[3].

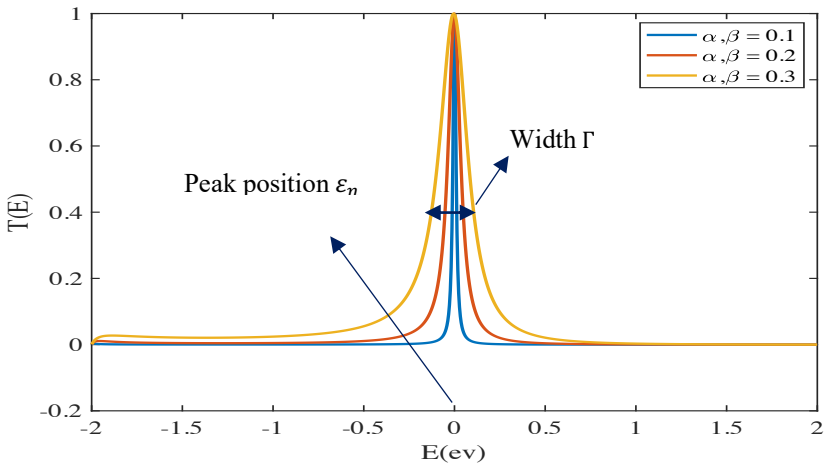

Fig. 3.10: The effect of varying the coupling on the width of resonance.

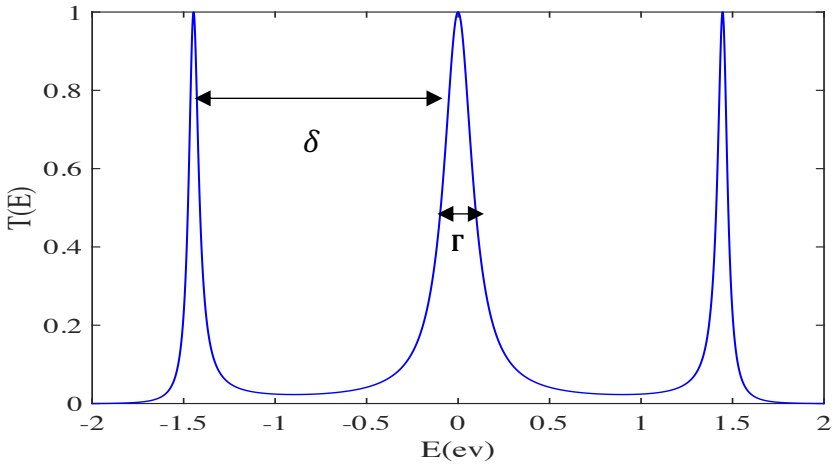

Fig.3.11: The transmission coefficient for a symmetric molecule attached symmetrically to identical leads ($\Gamma_1 = \Gamma_2$).

3.7.2 Fano-Resonance

Fano-resonances are widely known across many different branches of physics, which occurs when a bound state (e.g. a localized state located a pendant group of energy ε_p) interacts with the continuum of states[15]. It is described as phenomenon of constructive and destructive interferences between a bound state and the continuum. In other words, it is composed of an anti-resonance followed by a resonance with an asymmetric line profile. Fig. 3.12 shows a simple example of a system consists of a doubly infinite one-dimensional crystalline chain with site energies ε_o and hopping elements $-\gamma$ coupled to the pendant site of energy ε_p by coupling integral $-\alpha$.

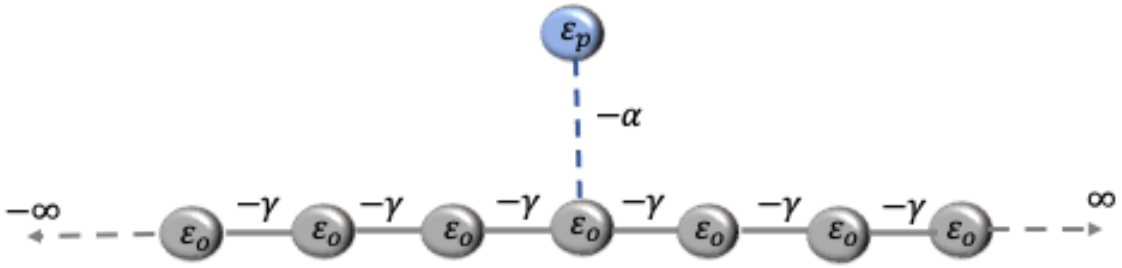

Fig. 3.12: Tight binding model of Fano-resonance, where a doubly- infinite chain coupled to a pendant site ε_p by coupling integral $-\alpha$.

Equation (3.108) is replaced by:

$$T(E) = \frac{4\Gamma_L \Gamma_R}{(E-\varepsilon)^2 + (\Gamma_L + \Gamma_R)^2}$$

where

$$\varepsilon = \varepsilon_n + \alpha^2/(E - \varepsilon_p)$$

This formula shows that when $E = \varepsilon_p$, $\varepsilon \to \infty$, the chain divides into two sections separated by an infinite tunnel barrier and therefore the transmission coefficient $T(E)$ vanishes. It also shows that when $E - \varepsilon = 0 \to (E - \varepsilon_n)(E - \varepsilon_p) - \alpha^2 = 0$, there are two solutions to this equation close to

ε_p and ε_n . When $E = \varepsilon_n$, the Breit-Wigner resonance occurs, whereas at $E = \varepsilon_p$ anti-resonance takes place forming a Fano resonance. Fig. 3.13 exhibits destructive QI at $E = \varepsilon_p$, arising from Fano resonances associated with the pendant groups, for different values of $\alpha = 0.1, 0.2$ and 0.3 which in turn determines the positions of the two resonances.

It is worth mentioning that Fano-resonance can control electrical transport and lead to giant thermopowers and figure of merit in single-molecule devices[6] .It has been observed in various quantum systems, such as nanowires, tunnel junctions and quantum dots[20].

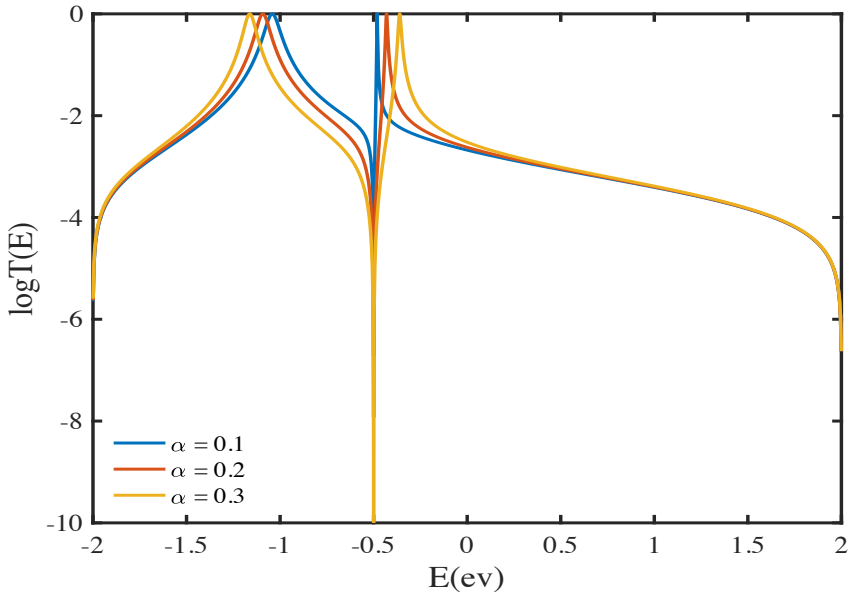

Fig. 3.13: The transmission coefficient versus energy E for different values of α at ε_p= -0.5

3.8 Conclusion

In summary, a theory of single particle transport was discussed, which forms the main numerical tool for studying the charge transport through molecules. The theoretical basis for calculating electronic transport was described, including the study of one-dimensional scattering theory and Green's functions for different transport regimes. In addition, the Landauer formula with a simple derivation was presented. The general methodology to calculate the transmission coefficient in a molecular junction for electrons passing from one electrode to the other was described. Finally, different types of resonances with different quantum interference patterns have been displayed.

3.9 Bibliography

(1) Thoss, M.; Evers, F. Perspective: Theory of Quantum Transport in Molecular Junctions. *J. Chem. Phys.* **2018**, *148* (3), 030901.

(2) Schulz, S.; Czycholl, G. Tight-Binding Model for Semiconductor Nanostructures. *Phys. Rev. B* **2005**, *72* (16), 165317.

(3) Lambert, C. J. *Quantum Transport in Nanostructures and Molecules: An Introduction to Molecular Electronics*; IOP Publishing, 2021.

(4) Gruss, D.; Velizhanin, K. A.; Zwolak, M. Landauer's Formula with Finite-Time Relaxation: Kramers' Crossover in Electronic Transport. *Sci. Rep.* **2016**, *6* (1), 24514.

(5) Landauer, R. Electrical Transport in Open and Closed Systems. *Z. Fü r Phys. B Condens. Matter* **1987**, *68* (2–3), 217–228.

(7) Claughton, N. R.; Leadbeater, M. Theory of Andreev Resonances in Quantum Dots. 29.

(8) Sadeghi, H. Theory of Electron, Phonon and Spin Transport in Nanoscale Quantum Devices. *Nanotechnology* **2018**, *29* (37), 373001.

(9) Gantenbein, M.; Wang, L.; Al-Jobory, A. A.; Ismael, A. K.; Lambert, C. J.; Hong, W.; Bryce, M. R. Quantum Interference and Heteroaromaticity of Para-and Meta-Linked Bridged Biphenyl Units in Single Molecular Conductance Measurements. *Sci. Rep.* **2017**, *7* (1), 1–9.

(10) Gehring, P.; Sadeghi, H.; Sangtarash, S.; Lau, C. S.; Liu, J.; Ardavan, A.; Warner, J. H.; Lambert, C. J.; Briggs, G. Andrew. D.; Mol, J. A. Quantum Interference in Graphene Nanoconstrictions. *Nano Lett.* **2016**, *16* (7), 4210–4216.

(11) Wang, X.; Bennett, T. L.; Ismael, A.; Wilkinson, L. A.; Hamill, J.; White, A. J.; Grace, I. M.; Kolosov, O. V.; Albrecht, T.; Robinson, B. J. Scale-up of Room-Temperature

Constructive Quantum Interference from Single Molecules to Self-Assembled Molecular-Electronic Films. *J. Am. Chem. Soc.* **2020**, *142* (19), 8555–8560.

(12) Ye, J.; Al-Jobory, A.; Zhang, Q.-C.; Cao, W.; Alshehab, A.; Qu, K.; Alotaibi, T.; Chen, H.; Liu, J.; Ismael, A. K. Highly Insulating Alkane Rings with Destructive σ-Interference. *Sci. CHINA-Chem.* **2022**.

(13) Naghibi, S.; Ismael, A. K.; Vezzoli, A.; Al-Khaykanee, M. K.; Zheng, X.; Grace, I. M.; Bethell, D.; Higgins, S. J.; Lambert, C. J.; Nichols, R. J. Synthetic Control of Quantum Interference by Regulating Charge on a Single Atom in Heteroaromatic Molecular Junctions. *J. Phys. Chem. Lett.* **2019**, *10* (20), 6419–6424.

(14) Breit, G.; Wigner, E. Capture of Slow Neutrons. *Phys. Rev.* **1936**, *49* (7), 519–531.

(15) Ismael, A. K.; Grace, I.; Lambert, C. J. Connectivity Dependence of Fano Resonances in Single Molecules. *Phys. Chem. Chem. Phys.* **2017**, *19* (9), 6416–6421.

(16) Cai, C.; Zhu, R. Fano Resonance via Bonding and Antibonding States in Nonadiabatically-Pumped Double-Quantum-Well Systems. *Phys. Lett. A* **2017**, *381* (43), 3675–3682.

(17) Miroshnichenko, A. E.; Flach, S.; Kivshar, Y. S. Fano Resonances in Nanoscale Structures. *Rev. Mod. Phys.* **2010**, *82* (3), 2257–2298.

(18) Miroshnichenko, A. E.; Flach, S.; Kivshar, Y. S. Fano Resonances in Nanoscale Structures. *Rev. Mod. Phys.* **2010**, *82* (3), 2257–2298.

(19) Tekman, E.; Bagwell, P. F. Fano Resonances in Quasi-One-Dimensional Electron Waveguides. *Phys. Rev. B* **1993**, *48* (4), 2553–2559.

(20) Ho, J. F.; Luk'yanchuk, B.; Zhang, J. B. Tunable Fano Resonances in Silver–Silica–Silver Multilayer Nanoshells. *Appl. Phys. A* **2012**, *107* (1), 133–137.

Chapter 4

Tuning Fermi Level Alignment in Large Scale Self-Assembled Oligo (phenylene-ethynylene) Derivatives

This work was carried out in collaboration with the group of Prof. Martin R. Bryce (Department of Chemistry, Durham University), who synthesized the SAMs that were used in this work and Prof. Christopher J. B. Ford (Department of Physics, University of Cambridge), who conducted the experiments. Theoretical work was carried out at Lancaster by myself. This work was submitted in the name of

"Tuning Fermi Level Alignment in Large Scale Self-Assembled Oligo (phenylene-ethynylene) Derivatives**"**

Xintai Wang, Hanan Althobaiti, Shanglong Ning, Alaa Al-Jobory, Jan Girovsky, Hippolyte P.A.G. Astier, Luke J. O'Driscoll, Martin R. Bryce, Colin J. Lambert and Christopher J. B. Ford.

The aim of this chapter is to examine the effects of orbital alignment in large-scale self-assembled monolayers (SAMs), with single-layer graphene (SLG) as a top electrode and gold as a bottom electrode, to provide asymmetry to a single-molecule junction. The SAMs are formed from oligo(phenylene-ethynylene) (OPE)-based molecular wires with different molecule-electrode contacts. OPE derivatives are molecules consisting of phenyl rings connected with triple bonds. They have a highly conjugated aromatic structure, due to the delocalization of the electrons along the molecular backbone. Such a structure results in the energy gap between the lowest unoccupied molecular orbital (LUMO) and the highest occupied molecular orbital (HOMO) being smaller (~3

eV) than the HOMO – LUMO gap of saturated molecules (~ 7eV), leading to more efficient charge transport through the molecule. In this work, we design and simulate a three-terminal junction, in which the OPE derivatives, conjugated molecules with different anchoring groups, were integrated between the single-layer graphene (SLG) and the gold electrode to form SLG/molecule/Au junction.

4.1 Motivation

Molecular devices consisting of single or multiple molecules bridging two or more electrodes have attracted intense theoretical and experimental interest, due to their tunable and unique transport properties[1,2].The testbeds for molecular-electronic measurements are either single-molecule junctions or large-scale molecular thin films formed from self-assembled monolayers (SAMs)[3–6]. The central challenge for single-molecule electronics is the uncertainty in the binding geometry of single molecules located between two metal electrodes. This uncertainty is reduced in SAMs, because molecules are fixed in specific conformations due to intermolecular forces between neighbouring molecules[3,7–9]. Recent studies have demonstrated that electron transport properties of molecular wires can be controlled by chemically varying their anchor groups to the electrodes, which causes a shift of molecular orbital alignment[10–13]. Understanding and controlling the orbital alignment of molecules placed between electrodes is essential in the design of applicable molecular electronic devices. The orbital alignment is determined both by the molecular backbone structure and the molecule-electrode interface. The energy levels alignment after the formation of a molecular tunnel junction is often poorly understood because spectroscopy inside junctions is not possible, which complicates the interpretation of the data generated by molecular junctions[14]. Therefore, controlling the alignment of molecular orbitals with respect to the Fermi level of the

electrodes is a major challenge in the field of molecular electronics. Recently, in an effort to overcome this challenge, Xin *et al.* used the ionic-liquid gate to effectively modulate the alignment between molecular frontier orbitals and the Fermi energy level of graphene electrodes, thus tuning the charge transport properties of the junctions[15]. Famili et al. reported that an effective gate control was achieved using an ionic liquid, in which a strong gating electric field, generated from the electrical double layer (EDL) of ionic liquid, is vertically applied to the graphene/SAM/gold junctions, and thus tunes the energy levels of the SAM resulting in a significant conductance modulation in the molecular transistors[16].

This work sheds light on how to control electron transport within the HOMO-LUMO energy gap in molecular junctions. Most studies of molecular orbital alignment in molecular junctions involve tuning their energy levels via a back gate. However, this is difficult to achieve in scalable self-assembled monolayers (SAMs), because SAM-based junctions are bottom-up designs, and the bottom metal electrode could screen out the electric field produced by a back gate[15,17,18]. On the other hand, the use of graphene in this study, as a conductive material, offers a possibility for gating SAMs via a top[4,16,19] gate, because the ultra-thin nature of single-layer graphene (SLG) allows some of the electric field to penetrate through vertically[20–22].

4.2 Three-terminal junction

Charge transport in molecular junctions has been studied extensively in both two- and three-terminal configurations, because such junctions are excellent candidates for testing quantum transport theories and hold significant promise in terms of reaching the ultimate limit of device miniaturization[23]. Three-terminal device that feature an additional gate electrode, has established

the feasibility of actively tuning the charge transmission characteristics of molecular junctions[5,24]. It combines both the ability to form a stable single-molecule junction and the ability to shift the energy levels of the molecule by gating[25].

Control of the molecular conductance by a third electrode is not only a necessary requirement for integration of molecular devices in circuits, but also essential for a comprehensive study of transmolecular conduction[26–32]. As the gate electrode allows to repel and attract electrons, it can be used to oxidize and reduce molecules and investigate molecular transport properties for different charge states. Three-terminal devices have also been employed to reveal the fine structure of individual single-molecule magnets and the presence of magnetic anisotropy[15,33,34].

From an experimental point of view, three-terminal molecular devices (an example is shown in Fig. 4.1), have been fabricated by several approaches. These include electromigration in which a metal wire is broken with an electric field[35], shadow evaporation[36] and electrochemical techniques such as mechanically controllable break junction (MCBJ)[25]. Despite the impressive progress made in this field, addressing three-terminal device still implies several technological challenges. The main challenge is certainly how to embed a single molecule between the source and drain electrodes in a reliable way and place the gate electrode a few angstroms away from the molecule to achieve the required gate field. In this chapter I present model of a three-terminal electrodes, where a molecule bridges the gap between two graphene electrodes and a gold electrode, which is explained in more detail in section 4.8.

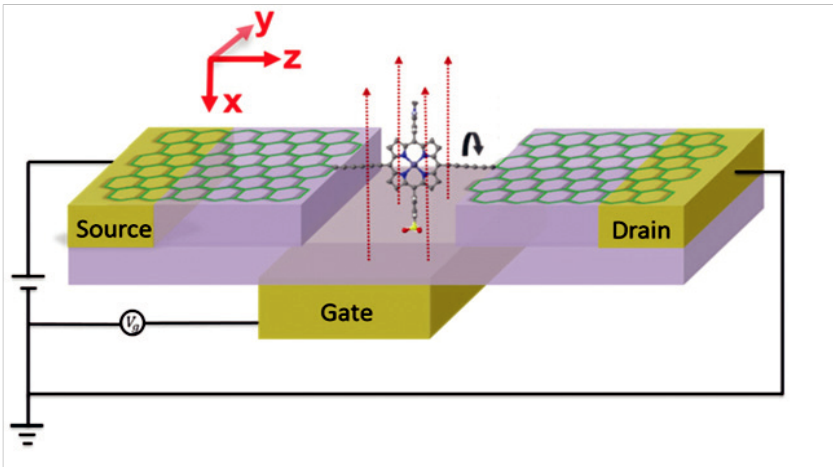

Fig. 4.1: Three-terminal concept for nanoscale switch with source and drain and gate electrodes[30].

4.3 Molecular structure

Charge transport in molecular junctions significantly depends on the chemical identity of the anchor groups and on the nature of the chemical interactions at the electrode-molecule interface[37–39]. The ideal anchoring group would provide reproducible, well-defined binding, strong anchoring and a small contact resistance[13,40]. Fig. 4.2 shows a selection of anchoring groups that have been used in this chapter. In what follows, I will discuss the structure of these anchors and some of their properties. Several previous studies have shown that stable and reproducible single-molecule junctions are formed if thiol (-SH), methyl thioether (-SMe) and pyridyl (-Py) groups are used as anchoring groups[41]. Thiol (-SH) has been most widely employed as a terminal anchor groups due to its high binding energy to many metals, such as gold, copper and silver[42]. The strong interaction between (-SH) and the metal electrodes often leads to rather high conductance values. Another good candidate for anchoring group is pyridine (-C_5H_4N), which is stable under ambient conditions and does not require protective groups, meaning that it forms stable and reproducible molecular

junctions[43]. In this vein, Hong *et al.* reported that the mechanical stability and the probability of forming a junction is highest for (-Py), followed by (-SH)[41].

Thioacetates (-SAc), which have the molecular formula (-S-$COCH_3$), are archetypal masked thiols, as they can be deprotected under mild conditions to form thiolates[44]. Notably, thioacetates spontaneously cleave in the presence of gold to form the direct Au–S bonds that would be expected from thiols[43,45].

Another simple functional group which has been utilised for anchoring is thioether (-SMe), in which the sulfur is bonded to the methyl group (-S-CH_3). It has seen increasing use in recent years as it allows for strong Au–S interactions (albeit weaker than those between thiols and gold). An important difference between (–SMe) and (–SAc) anchoring groups is that the methyl group is retained upon binding to a gold surface whereas the acetate group is not[43].

Carbazole was selected in this study as a support for of the additional anchors (-SMe). It consists of two benzene rings fused together on either side of a pyrrole ring, that is a five-membered ring in which the heteroatom has at least one pair of non-binding valence shell electrons[46].

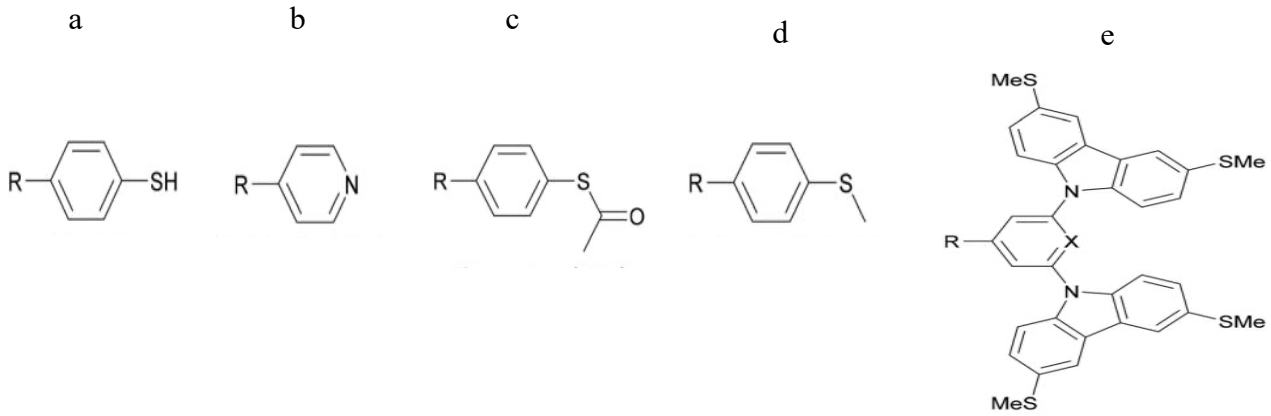

Fig. 4.2: Selected anchors groups used in the formation of OPE molecular junctions, for simplicity, anchors groups are shown attached to a benzene ring unless they already form part of the terminal aromatic system (e.g., pyridine derivatives)[35]. a: Thiol (-SH), b: Pyridine (-C_5H_4N), c: Thioacetate (-SAc), d: Thioether (-SMe), e: Carbazole-based tetrapod x=CH, N.

In the present work, I investigate 6 different molecules with oligo(phenylene-ethynylene) (OPE) backbones, the chemical structures of which are shown in Fig. 4.3. Molecule **1** has acetyl-protected thiol (-SAc) terminal group at one end and is benzene terminated at the other end. Thiols are known to have strong affinity with gold, whereas benzene has negligible affinity to gold[9,47]. Molecules **2** and **3** are SAc terminated at one end and have a *para*- or *meta*- connected terminal pyridine group respectively at the other end. Pyridine is known to have a strong affinity to gold in either of these connectivities. Molecules **4** and **5** are symmetrical designs, with SAc terminal groups at both ends (in para positions). Molecule **5** contains an additional PE repeat unit compared to the other species in this study. Molecule **6** has a pyridine group at each end in the para position, and a methyl thioether (-SMe)-based tetrapodal group at one end[48].

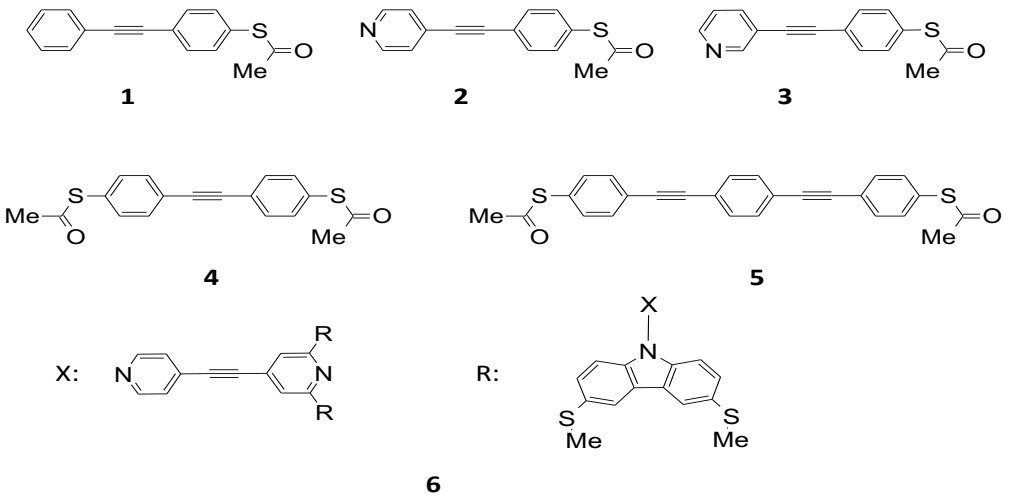

Fig. 4.3: Chemical structures of the *OPE*-based molecules. **1**, **2** and **3** are asymmetric molecules with different anchor groups involving thioacetate and pyridine, while **4** and **5** are symmetric molecules having PE repeat unit with thioacetate anchors from both ends. **6** is OPE2 backbone with the carbazole-based anchor groups including 4 thioether linkers.

The optimized geometry and ground state Hamiltonian of each structure in this chapter was obtained using the SIESTA implementation of density functional theory (DFT)[49,50], which has been presented in detail in chapter 2. SIESTA employs the norm-conserving pseudo-potentials to account for the core electrons and linear combinations of atomic orbitals to construct the valence states. The local density approximation (LDA) of the exchange and correlation functional by Ceperley and Adler is used along with double- polarized (DZP) basis sets. The real-space grid was defined by a plane wave cut-off of 250 Rydbergs. The optimum geometries of the isolated molecules **1-6** were obtained by relaxing the molecules until all forces on the atoms were less than 0.01 eV / Å as shown in Fig. 4.4. Results were also computed using the generalized gradient

approximation with the Perdew-Burke-Ernzerhof parameterization (GGA-PBE) and it was found that the resulting transmission functions were comparable with those obtained using LDA.

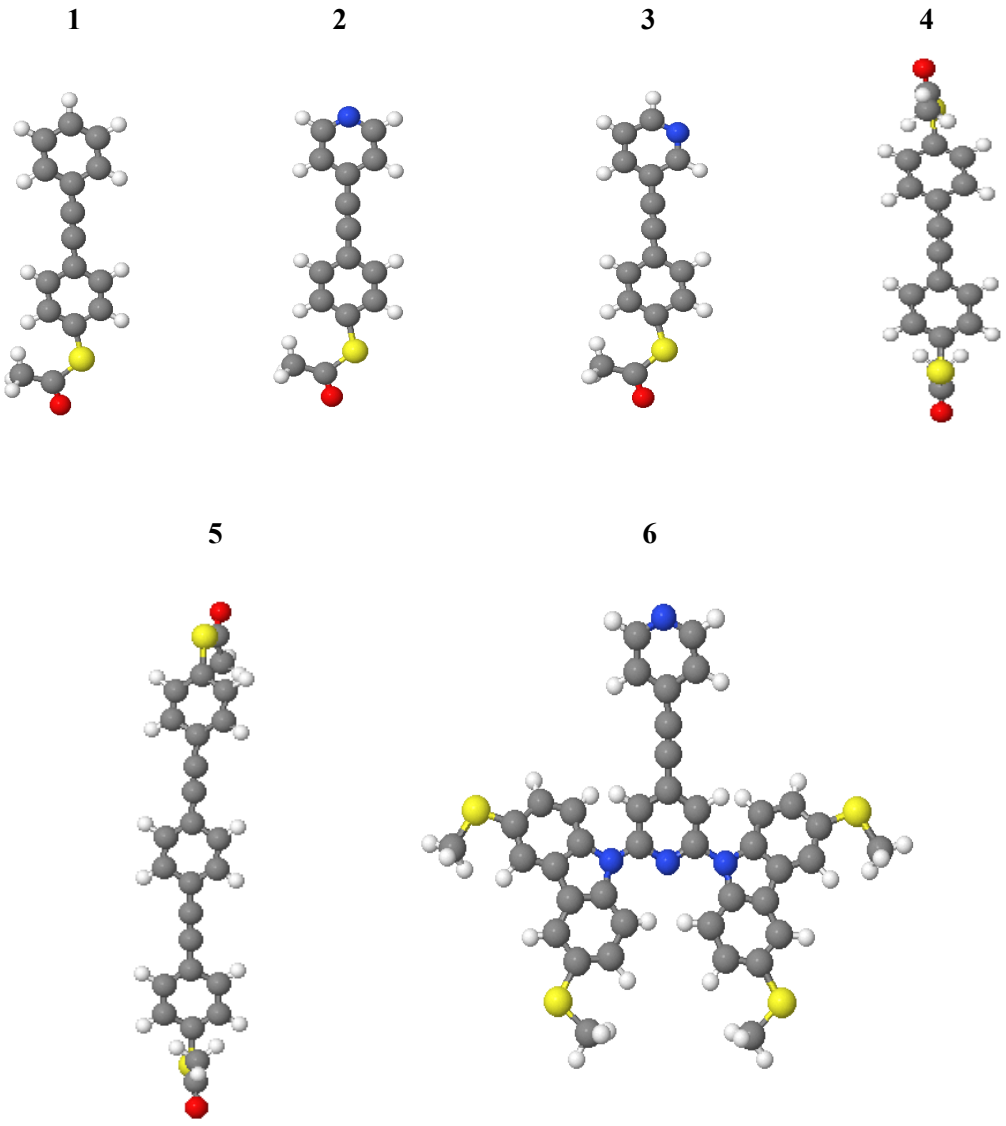

Fig. 4.4: Fully relaxed isolated molecules **1-6**. Key: C = grey, H = white, O = red, S = yellow, N=blue.

4.4 Frontier orbitals

To gain a deeper insight into the electronic properties of these structures (see Fig. 4.4), the DFT based methods discussed in chapter 2 have been used. The gas-phase electronic structures of all molecules were investigated to explore the distribution and composition of the frontier molecular orbitals. Plots of the frontier orbitals for the studied molecules **1-6** (see Fig. 4.4) are given in Figs. 4.5-4.10. The highest occupied molecular orbitals (HOMO), lowest unoccupied orbitals (LUMO), HOMO-1 and LUMO+1 along with their energies are calculated. By comparing the topology of the HOMO and LUMO orbitals of **1-6** molecules, one could notice that the HOMOs and LUMOs are extended across the backbone for each molecule, which suggests that they might act as electron-electron channels.

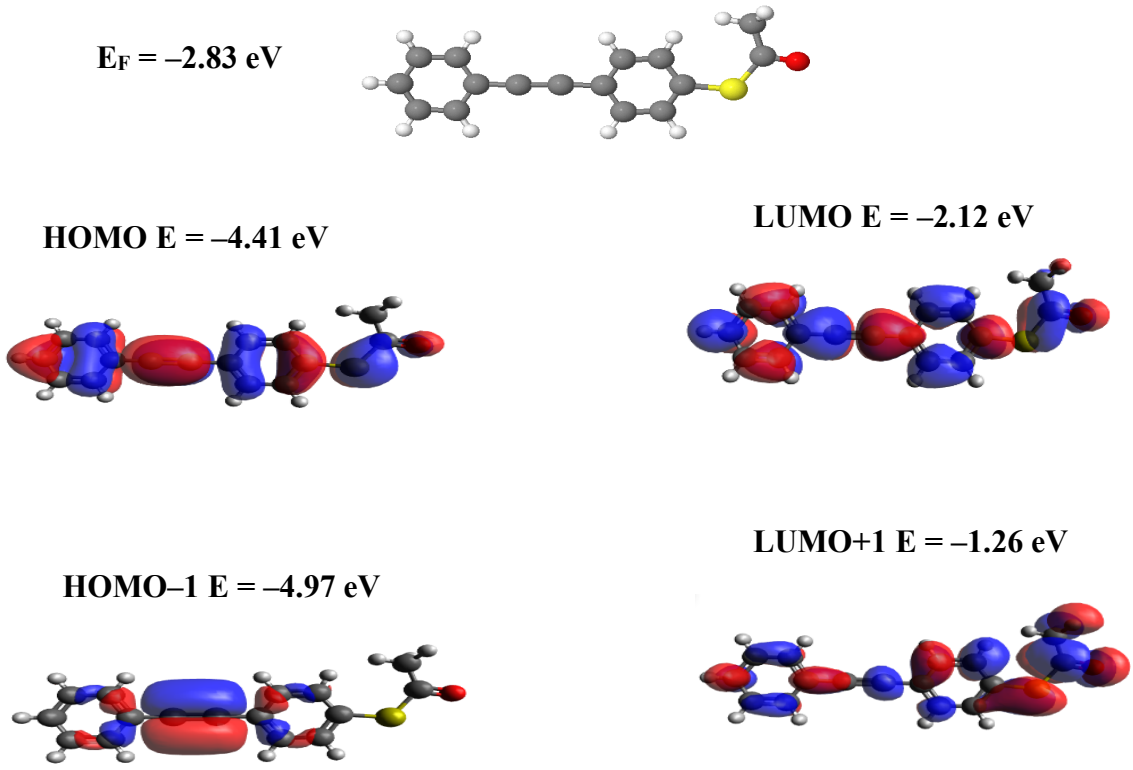

Fig. 4.5: Wave function for **1**. **Top panel**: Fully optimised geometry of **1**. **Lower panel**: HOMO, LUMO, HOMO–1 and LUMO+1 along with their energies.

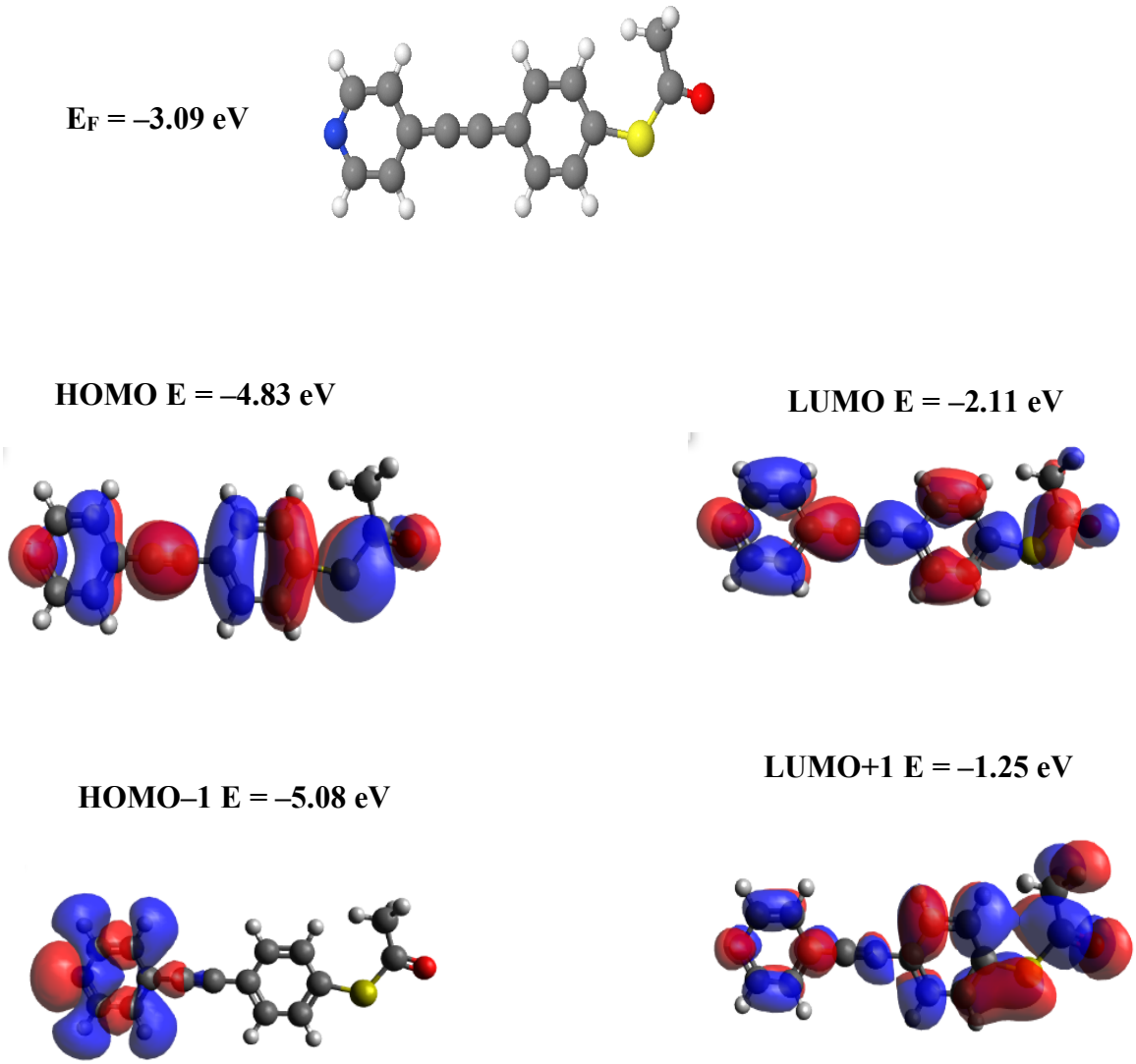

Fig. 4.6: Wave function for **2**. **Top panel**: Fully optimised geometry of **2**. **Lower panel**: HOMO, LUMO, HOMO–1 and LUMO+1 along with their energies.

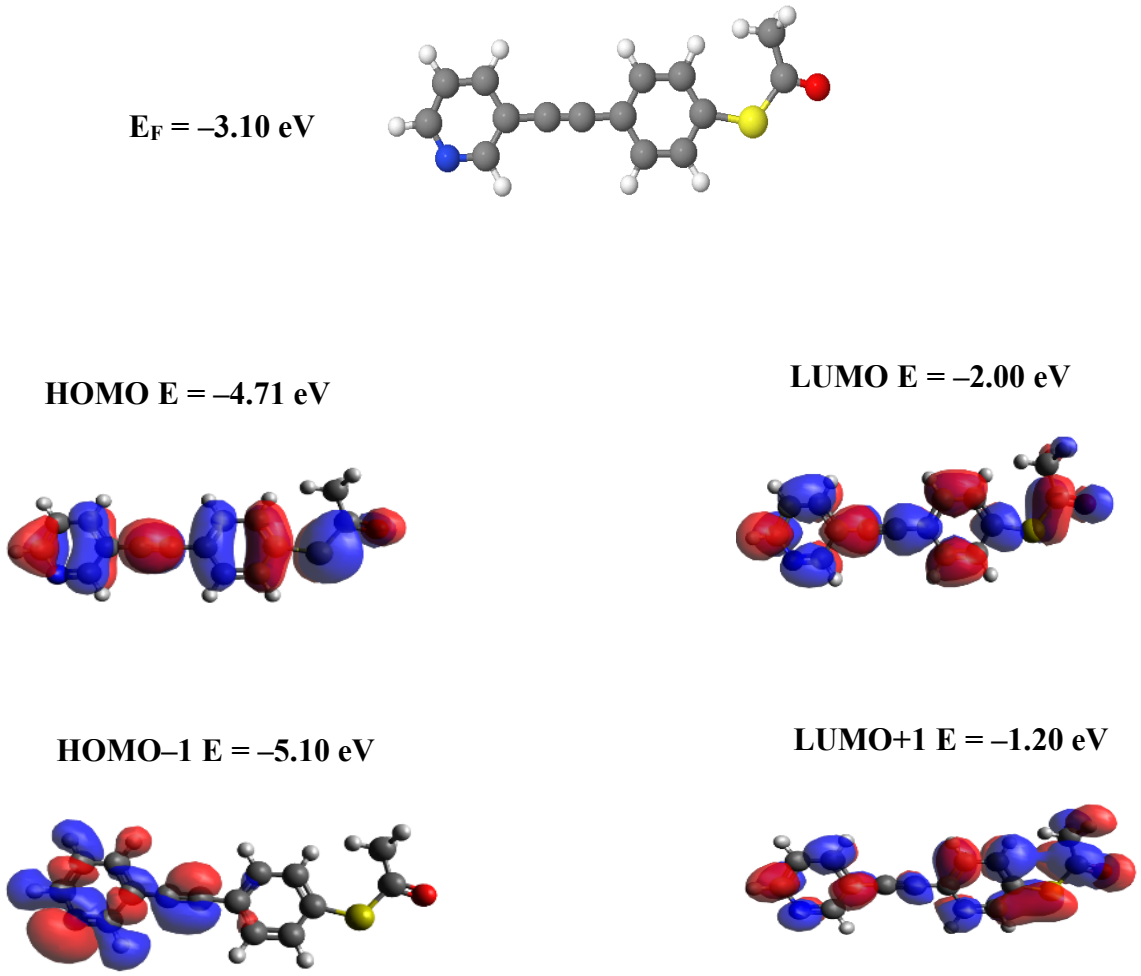

Fig. 4.7: Wave function for **3**. **Top panel**: Fully optimised geometry of **3**. **Lower panel**: HOMO, LUMO, HOMO–1 and LUMO+1 along with their energies.

E_F = –2.93 eV

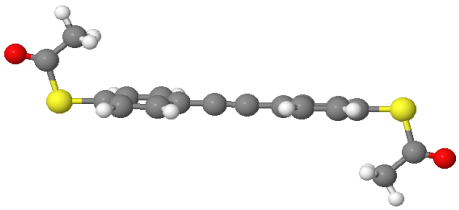

HOMO E = –4.88 eV

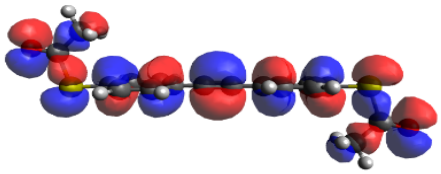

LUMO E = –2.28 eV

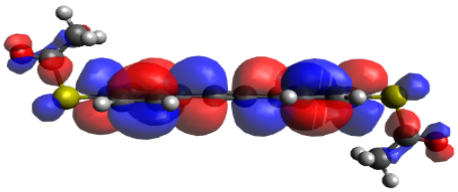

HOMO–1 E = –5.25 eV

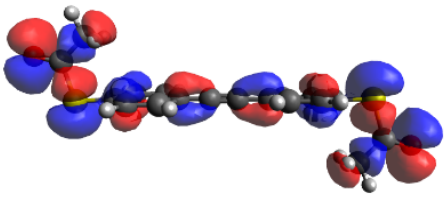

LUMO+1 E = –1.15 eV

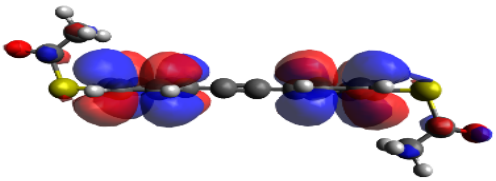

Fig. 4.8 : Wave function for **4**. **Top panel**: Fully optimised geometry of **4**. **Lower panel**: HOMO, LUMO, HOMO–1 and LUMO+1 along with their energies.

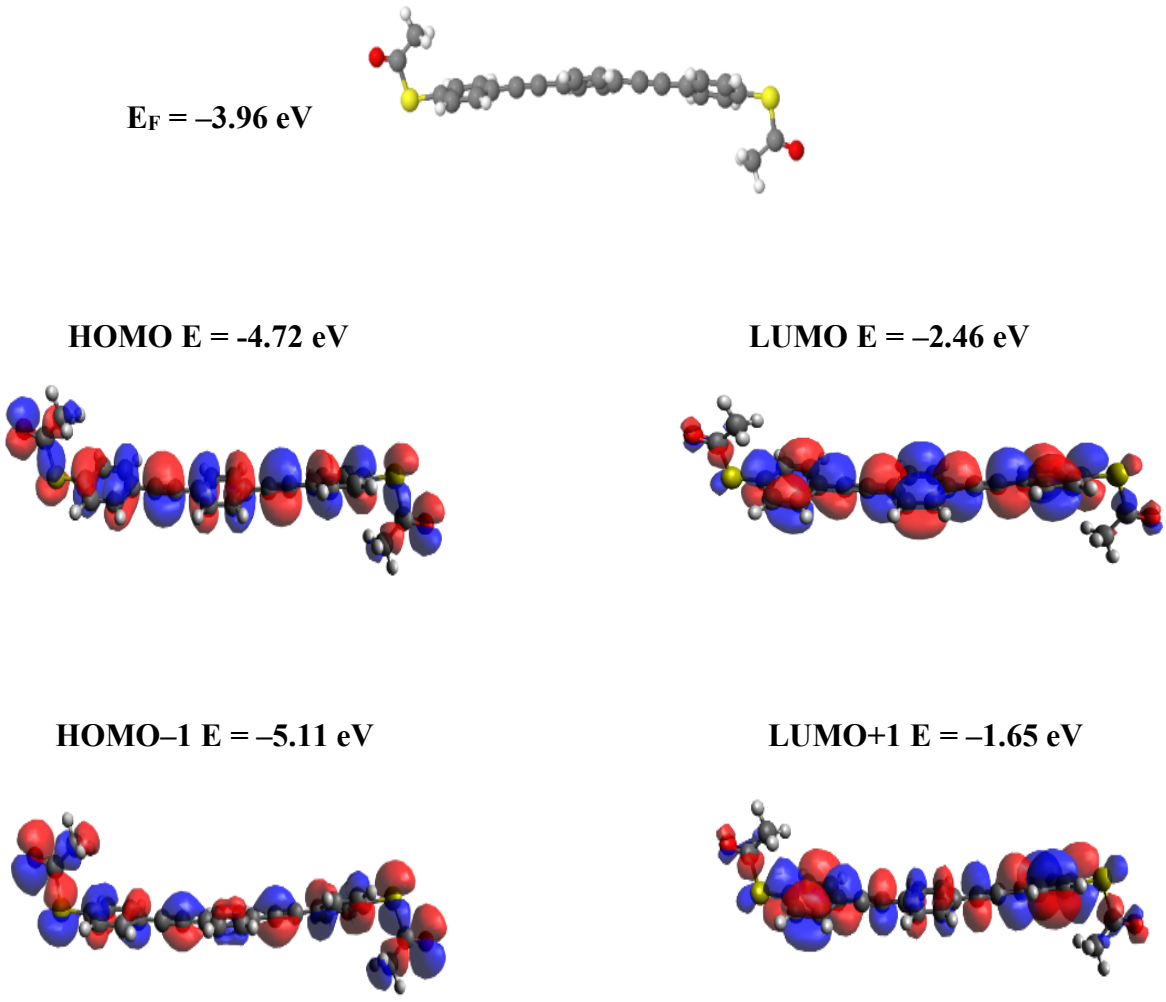

Fig. 4. 9: Wave function for **5**. **Top panel**: Fully optimised geometry of **5**. **Lower panel**: HOMO, LUMO, HOMO–1 and LUMO+1 along with their energies.

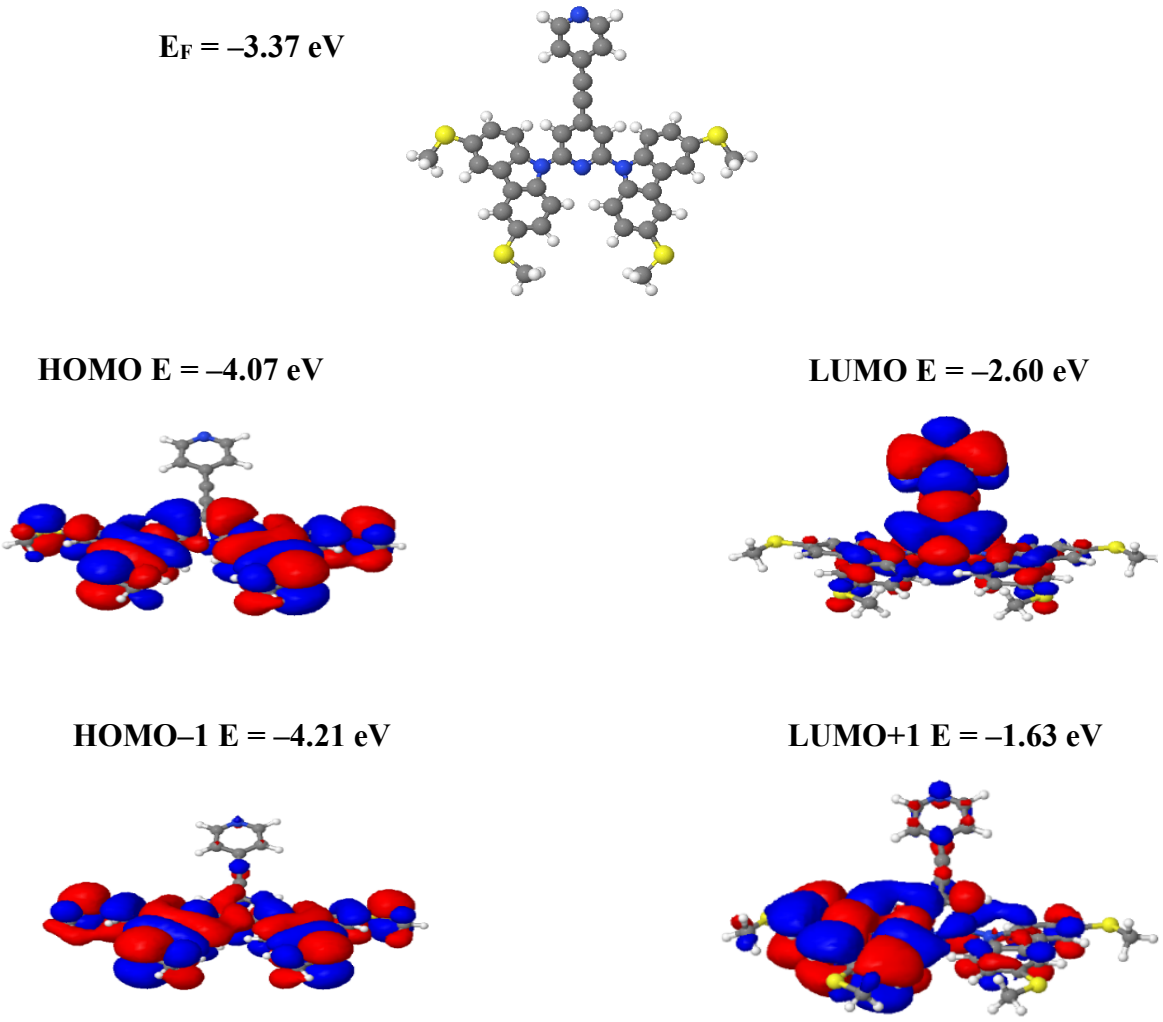

Fig. 4.10: Wave function for **6**. **Top panel:** Fully optimised geometry of **6**. **Lower panel**: HOMO, LUMO, HOMO–1 and LUMO+1 along with their energies.

4.5 Binding energy

The binding energy of anchor groups to the electrode plays a crucial role in determining the strength of molecule–electrode coupling, crucially impacting the chemical stability of the junction as well as its charge transport properties[11]. Since the different anchor groups possess different coupling strengths, in what follows, the optimum binding distance between the anchor groups and electrodes will be calculated using DFT and the counterpoise method, which removes basis set superposition errors (BSSE), as it is described in section 2.7.3 of chapter 2. The binding distance z is defined as the distance between the top or bottom surface and the anchor group (see the black double-arrow on the right panel of Figs. 4.11- 4.16).

If one of the compounds **1-6** is defined as entity A and the single-layer graphene (SLG) or gold electrode as entity B. The ground-state energy of the total system is calculated using SIESTA and is denoted $\mathrm{E}_{\mathrm{AB}}^{\mathrm{AB}}$. The energy of each entity is then calculated in a fixed basis, which is achieved in SIESTA using ghost atoms; (basis set functions which have no electrons or protons). Hence, the energy of the individual molecule **1-6** in the case of the fixed basis is defined as $\mathrm{E}_{\mathrm{A}}^{\mathrm{AB}}$ and for the graphene/gold as $\mathrm{E}_{\mathrm{B}}^{\mathrm{AB}}$. The energy difference $\Delta(z)$ between the isolated entities and their total energy when placed a distance z apart is then calculated using the following equation:

$$\text{Energy difference} = \Delta(z) = \mathrm{E}_{\mathrm{AB}}^{\mathrm{AB}} - \mathrm{E}_{\mathrm{A}}^{\mathrm{AB}} - \mathrm{E}_{\mathrm{B}}^{\mathrm{AB}} \tag{4.1}$$

Since the junction modelled in this study is asymmetric, in the following, I will calculate the binding energy between anchors and two different contact electrodes (i.e., gold and graphene).

4.5.1 Binding energy on graphene sheet

In this section, the binding energies and their corresponding optimum distances are calculated between the graphene surface and phenyl, pyridine (Py), thioacetate (SAc) anchors, as shown in Figs. 4.11-4.13.

Fig. 4.11 shows the binding energy as a function of the distance between the graphene surface and the phenyl ring (Gr-Phenyl), where the optimum distance (i.e., the minimum of the binding energy curve) is found to be $z = 2.4\,A^o$, with binding energy of approximately 0.11 eV. Fig. 4.12 exhibits the optimum distance between graphene and pyridine (Gr-Py) to be $z = 2.7A^o$, at approximately 0.14 eV, and the equilibrium distance between the thioacetate anchor and graphene (Gr-SAc) is obtained to be $z = 5.7A^o$, at approximately 0.09 eV, as shown in Fig. 4.13. The comparison between these Figs. reveals that the binding energies of graphene sheet to phenyl ring, Py and SAc anchor groups follow the trend $\left|E_{Gr-Py}\right| > \left|E_{Gr-phenyl}\right| > \left|E_{Gr-SAc}\right|$.

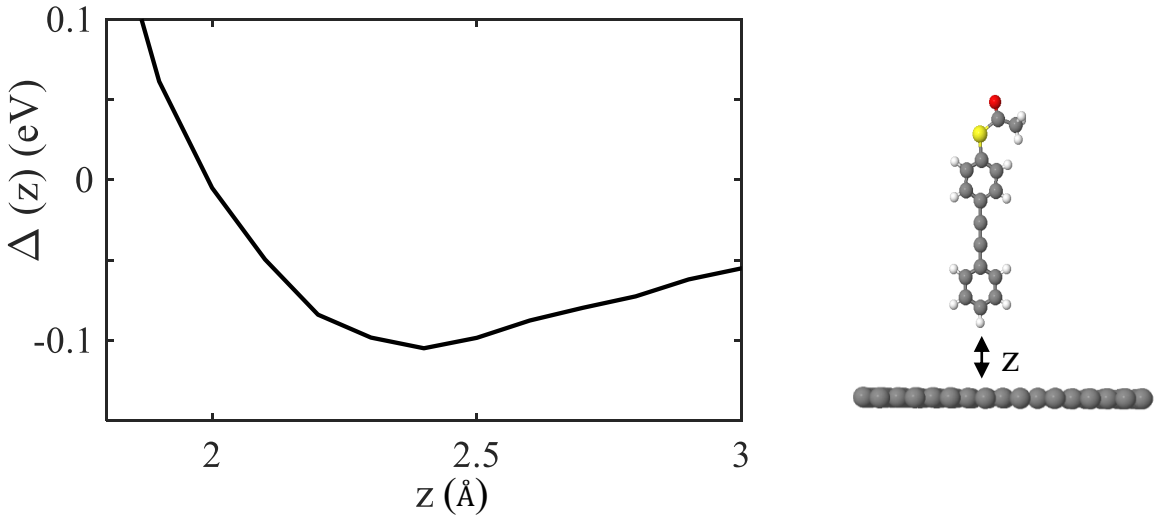

Fig. 4.11: Phenyl ring (molecule **1**) on a graphene surface (Right panel). Energy difference of phenyl anchor to graphene as a function of molecule-contact distance. The equilibrium distance corresponds to the energy minimum and is found to be approximately 2.4 Å (Left panel).

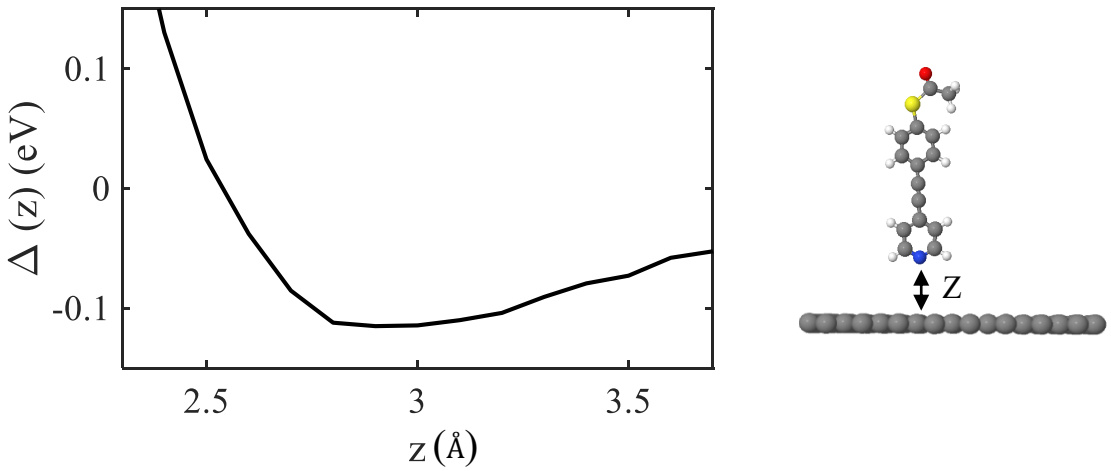

Fig. 4.12: Pyridine anchor (molecule **2**) on a graphene surface (Right panel). Energy difference of pyridine anchor to graphene as a function of molecule-contact distance. The equilibrium distance is approximately 2.7 Å (Left panel).

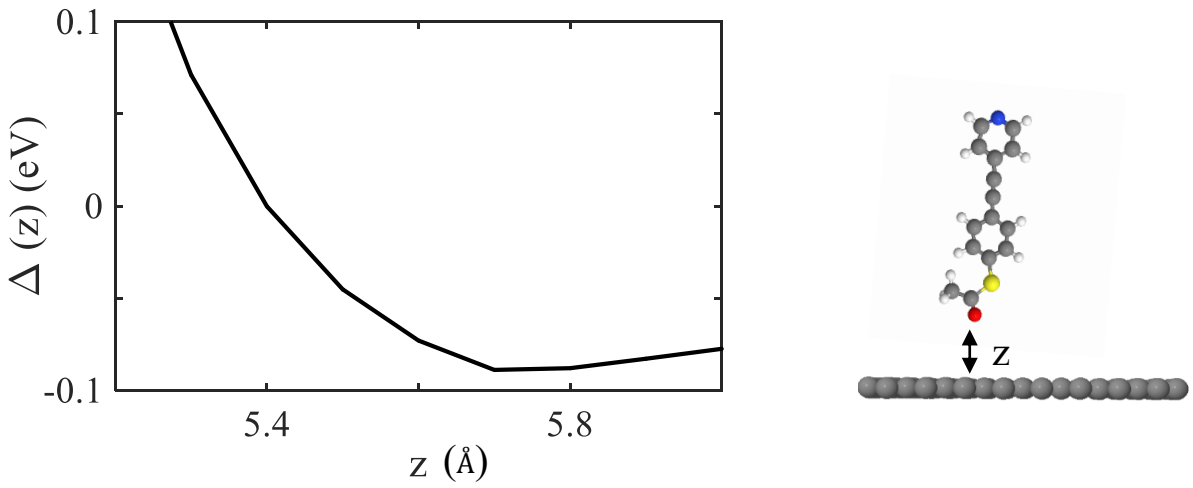

Fig. 4.13: Thioacetate anchor (molecule **2**) on a graphene surface (Right panel). Energy difference of thioacetate anchor to graphene as a function of molecule-contact distance. The equilibrium distance is approximately 5.7 Å (Left panel).

4.5.2 Binding energy on a gold surface

In the following, the binding energies are evaluated to find the optimum binding distance between the gold electrode and Py, thiol, SMe anchors, as shown in Figs. 4.14-4.16, where the right panels show the structure of the molecule linked to the gold electrode via anchor group, and the left panels represent the binding energy plots as a function of the optimum binding distance ***z***. Fig. 4.14 shows that the optimum binding distance between the Py anchor group and the Au to be 2.5 Å, and the B.E is found to be approximately 0.42 eV. This result is in goo.d agreement with the literature review[48,51].

To calculate the optimum distance between the Au and thiol anchor, the acetate anchor has been released, as shown in Fig. 4.15, which is found to be 2.7 Å, with approximately 0.85 eV in excellent agreement with the 0.8 eV in the literature[52]. This indicates that the binding energy of a thiol anchor group is approximately 2 times stronger than that of the Py anchor to the Au electrode. This is reasonable as thiol anchor provides strong electronic coupling to the gold surface through Au-S bond formation (strong covalent bond).

To determine the binding energy of four thioethers (SMe) to the Au, the two carbazole units in molecule **6** are parallel to the gold surface, as shown in the right panel of Fig. 4.16. The left panel of the same figure displays that each SMe contributes approximately 0.2 eV to the total binding energy at equilibrium distance of about 4.2 Å. This suggests that the use of multiple thioethers results in strong anchoring to a gold surface, where four thioethers make a contribution comparable to that expected from a thiol[48].

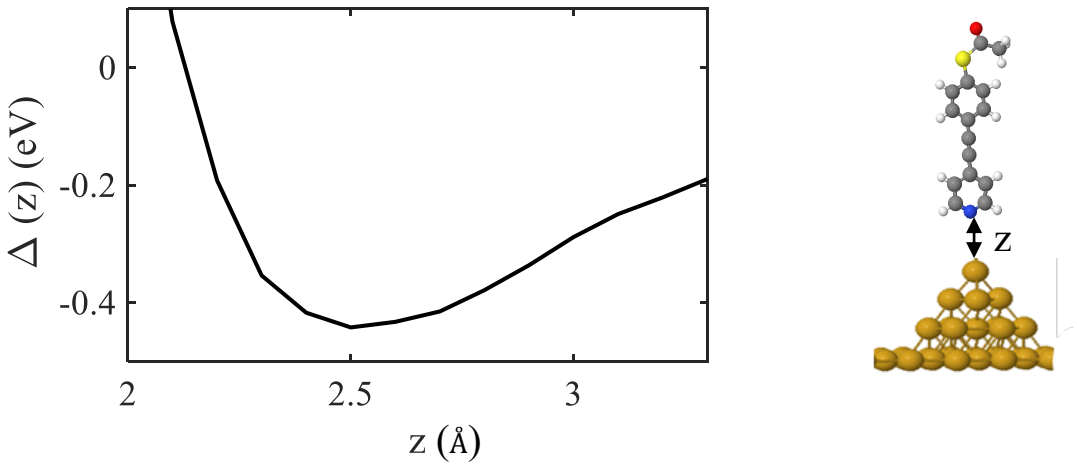

Fig. 4.14: Pyridine anchor (molecule **2**) on a gold surface (Right panel). Energy difference of pyridine anchor to gold as a function of molecule-contact distance. The equilibrium distance is approximately 2.5 Å (Left panel).

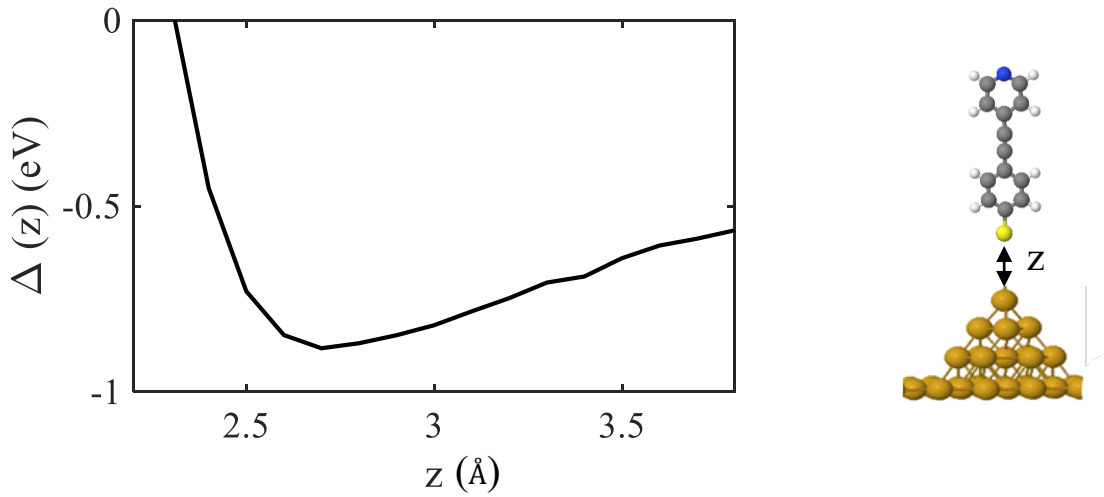

Fig. 4.15: Thiol anchor (molecule **2**) on a gold surface (Right panel). The acetate group has been released. Energy difference of thiol anchor to gold as a function of molecule-contact distance. The equilibrium distance is approximately 2.7 Å (Left panel).

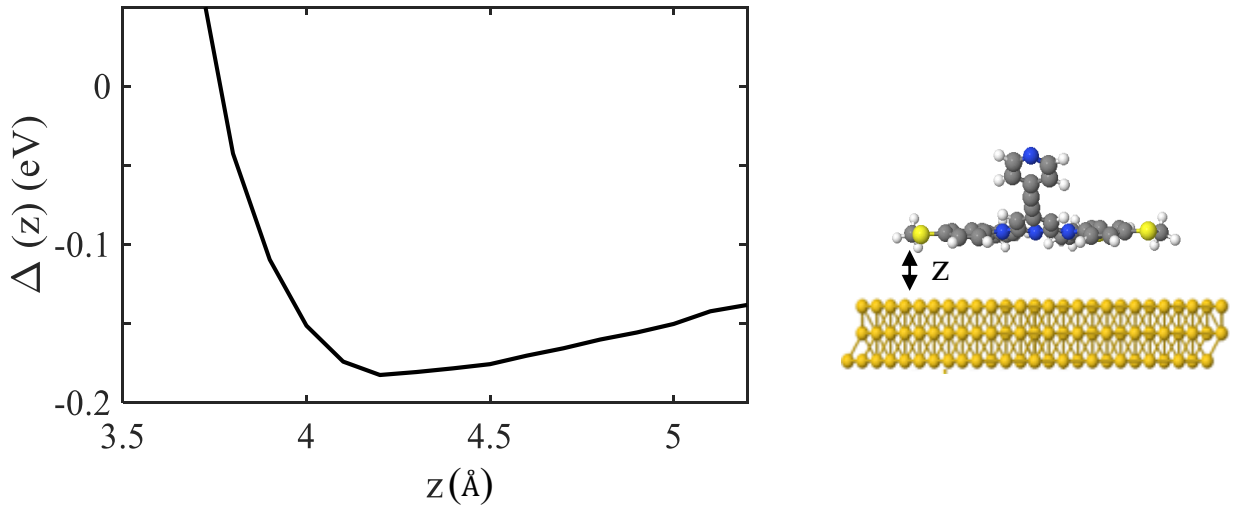

Fig. 4.16:Thioether anchor (molecule **6**) on a gold surface (Right panel). Energy difference of thioether anchor to flat gold as a function of molecule-contact distance. The equilibrium distance is approximately 4.2 Å (Left panel).

Table 4.1 represents the optimum separation distance and binding energy for five different anchor groups bind to graphene or gold electrodes. The comparison between them shows that the thiol anchor is coupled to Au (0.85 eV) more strongly compared to other anchors. In addition, the B.E. of Au to thiol, Py and SMe are 0.85 eV, 0.42 eV and 0.20 eV, respectively, whereas the B.E. of Gr to Py, phenyl and SAc are significantly weaker (0.14 eV, 0.11 eV and 0.09 eV, respectively). In other words, these anchors bind much more weakly to the Gr surface than to Au due to the fact that Van der Waals interactions between anchors and Gr are weak. For example, pyridine binds more strongly to Au (0.42 eV) than to graphene (0.14 eV), suggesting that pyridine is more likely to interact with a metallic surface than non-metallic.

Table 4.1: Summary of the energy-difference calculations (Figs. 4.11-4.16) for graphene-molecule (Gr-M) and gold-molecule (Au-M) contacts. z is the equilibrium distance and $\Delta(z)$ is the corresponding minimum energy difference.

Material-contact	$\Delta(z)$ **(eV)**	**z (Å)**
Gr-Phenyl	0.11	2.4
Gr-Py	0.14	2.7
Gr-SAc	0.09	5.7
Au-Py	0.42	2.5
Au-SH	0.85	2.7
Au-SMe	0.20	4.2

4.6 Optimised DFT structures of compounds within their junctions

Using the optimised structures and geometries for the compounds obtained as described above, I again employed the SIESTA code to calculate self-consistent optimised geometries, ground-state Hamiltonians and overlap matrix elements for each graphene-molecule-gold junction. The optimised structures were then used to compute the transmission curve for each compound, where a double-zeta-plus-polarization (DZP) basis set, with norm-conserving pseudopotentials was employed and the Hamiltonian and overlap matrices were calculated on a real space grid defined by a plane wave cutoff of 250 Ry. The local density approximation (LDA) of the exchange and correlation functional was used in all calculations, which is found to be comparable with those obtained using GGA. Figs. 4.17-4.22 illustrate the studied molecules in asymmetric junctions (i.e., Gr and Au contacts), in which the molecule is sandwiched between Gr and Au electrodes. Chap.2). The gold electrodes consist of five layers of (111) gold with each layer containing 25 gold atoms. To model the periodicity in the graphene, which consists of 110 atoms, the unit cell was repeated using a Bravais lattice with 50 k-points in y direction. Note that there is a tilt-angle range for each compound, which is presented in section 4.7. In this study, I investigate an asymmetric junction, that can be implemented by placing a single molecule between single-layer graphene (SLG) and gold surface. Fig. 4.17 shows the molecule **1**, which is an asymmetric molecule, sandwiched between the graphene sheet and the Au electrode, such that the thioacetate anchor is oriented towards the Au, and the phenyl ring is directed towards the graphene. Since the thioacetate cleaves in the presence of gold, a direct bond is formed between S and Au.

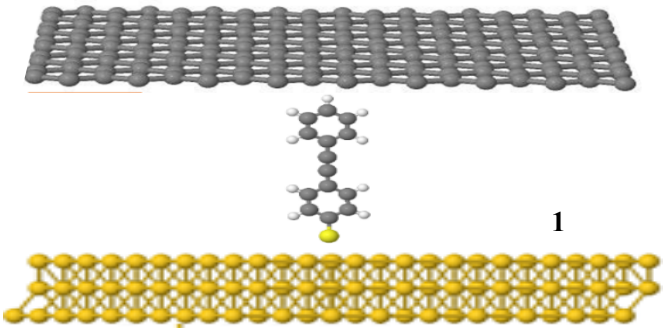

Fig. 4.17: Schematic illustration of an asymmetric junction containing a single molecule **1**. The top contact is single-layer graphene (SLG) and the bottom contact is gold. Note: here the molecule is asymmetric as well as the contacts (i.e., Gr and Au).

As mentioned above, molecule **2** is asymmetric (i.e., terminated with different anchors: thioacetate and Py), and thus flipping it results in two different configurations labelled **a** and **b** as shown in Fig. 4.18. In configuration **a,** molecule **2** is attached to the Gr sheet via pyridyl and the Au through thiol, which results from the cleavage of thioacetate with Au. In configuration **b** (the opposite of configuration **a)**, molecule **2** is flipped so that the thioacetate binds to the Gr sheet and pyridyl to Au. The same procedure is repeated for molecule **3,** which is the same as molecule **2,** but the pyridyl is located in meta position rather than para, leading to the possible binding configurations **a** and **b**, as shown in Fig. 4.19.

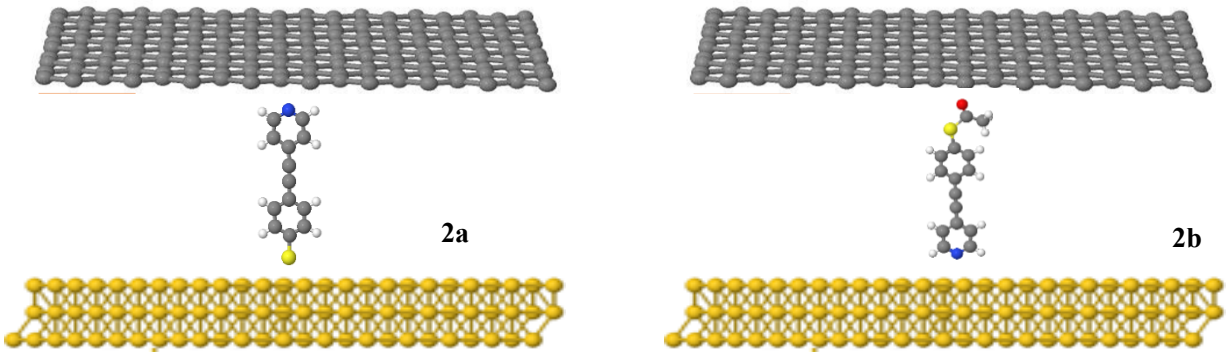

Fig. 4.18: Schematic illustration of asymmetric molecular junctions for **a** and **b. a** and **b** show how the molecule **2** flips between the Gr sheet and Au. **a** is when Py is linked to the Gr and **b** is when thioacetate is linked to the Gr. (Note: **2a** and **2b** molecular junctions are doubly asymmetric).

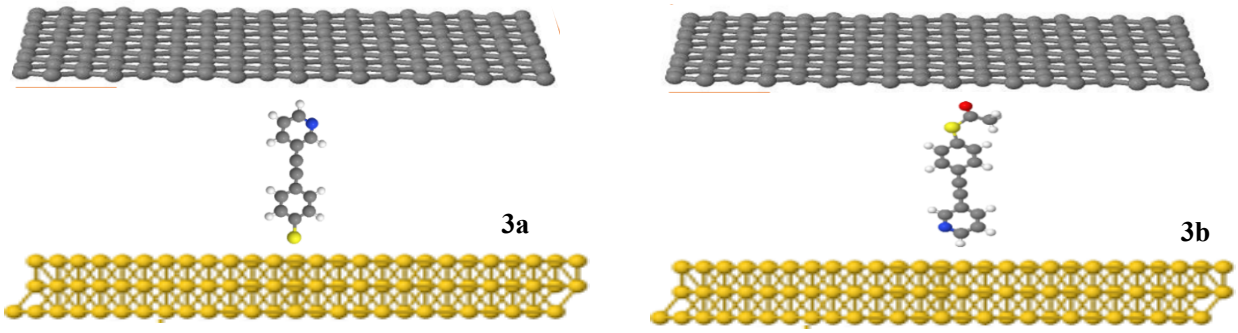

Fig. 4.19: Schematic illustration of asymmetric molecular junctions for **a** and **b. a** and **b** show how the molecule **3** flips between the Gr sheet and Au. **a** is when Py is linked to the Gr and **b** is when thioacetate is linked to the Gr (again these molecular junctions are doubly asymmetric).

As molecules **4** and **5** are symmetric molecules (terminated by thioacetate at each end), there will be one case for the junction, where the thioacetate is linked to the Gr sheet and the thiol is linked to the Au, as shown in Figs. 4.20 and 4.21. It should be noted that although molecules **4** and **5** are originally symmetric, the thioacetate group easily dissociates in the presence of Au to form Au-S, which eventually ends up as an asymmetric molecule with asymmetric contacts.

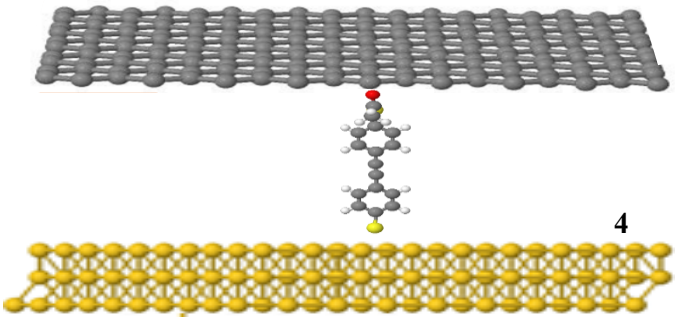

Fig. 4.20: Schematic illustration of an asymmetric junction containing a single molecule **4**. The top contact is single-layer graphene (SLG) and the bottom contact is gold. Note: here thiol is linked to Au (due to the cleavage of the thioacetate in the presence of Au), and thioacetate is linked to Gr.

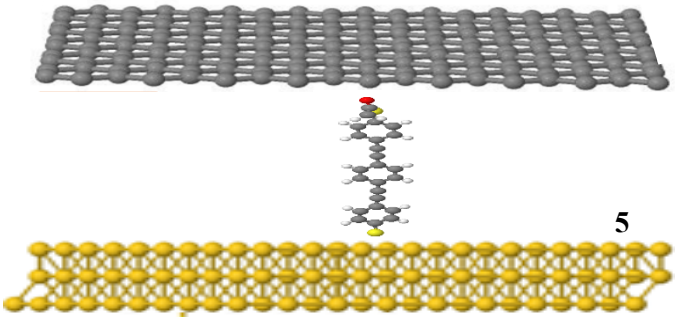

Fig. 4.21: Schematic illustration of an asymmetric junction containing a single molecule **5**. The top contact is single-layer graphene (SLG) and the bottom contact is gold. Again, thiol here is linked to Au (due to the cleavage of the thioacetate in the presence of Au), and thioacetate is linked to Gr.

Fig. 4.22 shows molecule **6** is positioned parallel to the Au, in which the four SMe anchors are oriented towards the Au surface and the Py anchor is directed towards the Gr sheet. It is worth

noting that the torsion angle between the central benzene ring and the two carbazole units is approximately 37^{o}.

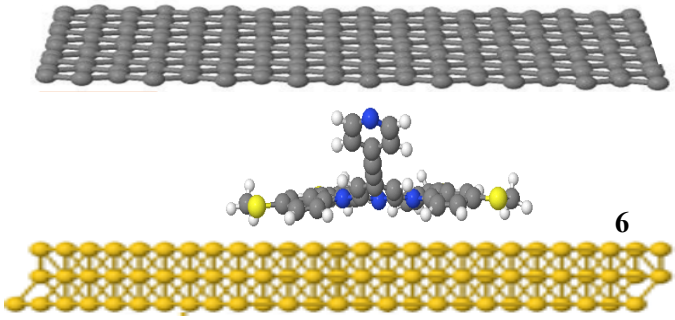

Fig. 4.22: Schematic illustration of an asymmetric junction containing a single molecule **6**. The top contact is single-layer graphene (SLG) and the bottom contact is gold. Here, 4 SMe are linked to Au and Py is linked to Gr.

4.7 The tilt angle (θ)

In this section, I shall determine the tilt angle θ of each compound between SLG and gold contacts, which corresponds to the experimentally measured most-probable break-off distance. A theoretical model of how the tilt angle varies between the SLG and Au substrate is shown in Fig. 4.23

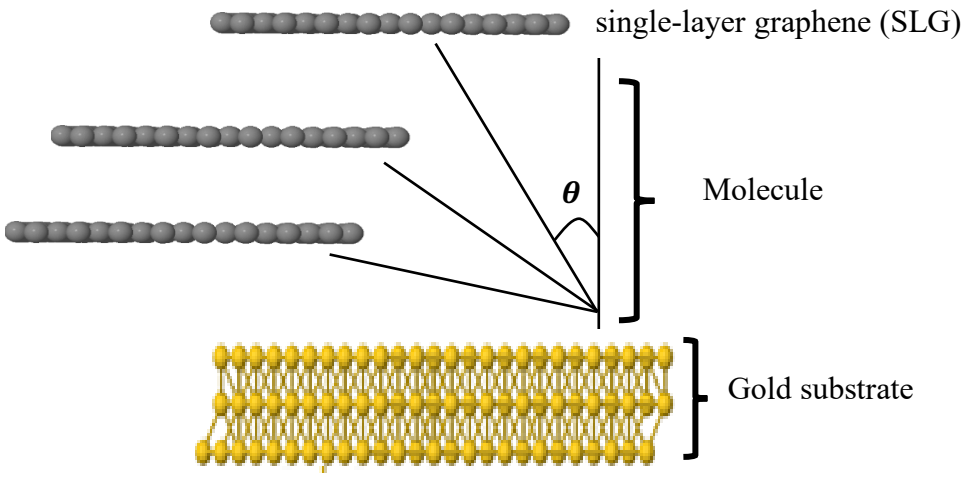

Fig. 4.23: Schematic representation of the tilt angle model (θ), which varies between the graphene sheet and the substrate gold.

Table 4.2 shows a range of tilt angles calculated from the film thickness for each molecule. Break-off distance values suggest that compounds **1**, **2a**, **3a**, **4, 5** and **6** tilt at an angle θ ranging from 35° to 45°, compound **2b** tilt at 65° to 75°, and **3b** tilt at 10° to 20° as shown in Figs. 4.24-4.29.

Table 4.2: Experimental break-off distance (film thickness), and equivalent tilt angle (θ)

Compound	Experimental film thickness (nm)	Equivalent experimental tilt angle (θ)
1	0.8	35°-45°
2a	1.05	35°-45°
2b		65°-75°
3a	0.7	35°-45°
3b		10°-20°
4	1.1	35°-45°
5	1.7	35°-45°
6	0.8	37°-48°

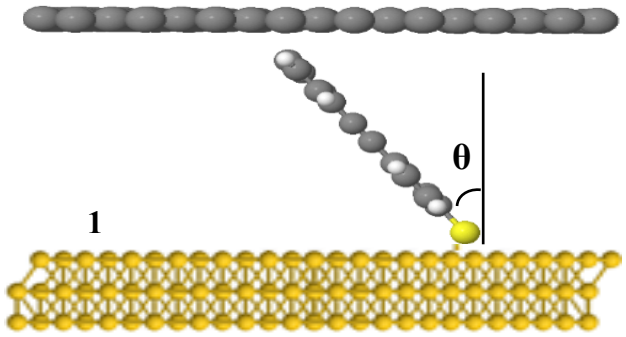

Fig. 4.24: Schematic illustration of Au/**1**/SLG junction with a tilt angle θ ≈ 40° for molecule **1** between Gr sheet and gold.

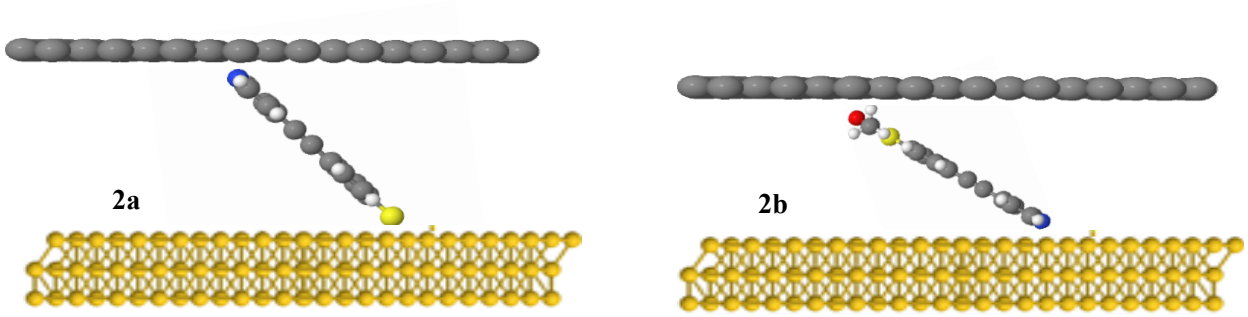

Fig. 4.25: Schematic illustration of Au/**2a** and **2b**/SLG junctions with tilt angles of θ ≈ 40° and 70° respectively for **2a** and **2b** between Gr sheet and gold

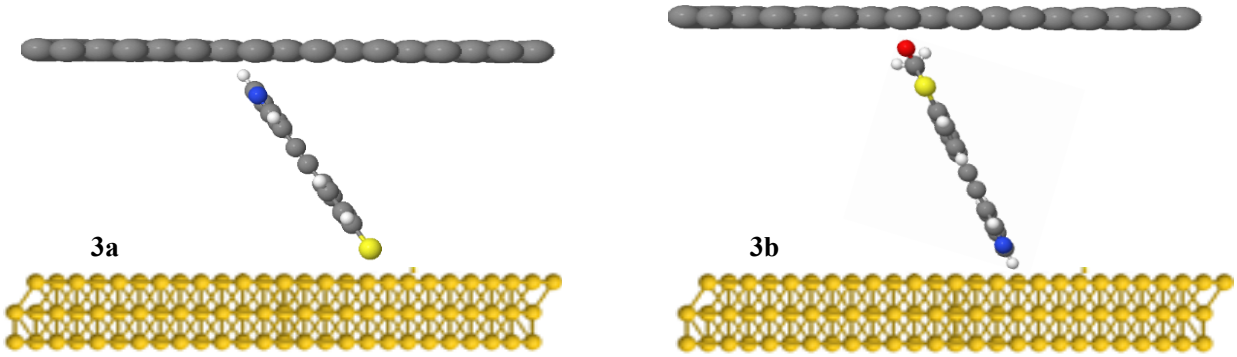

Fig. 4.26: Schematic illustration of Au/**3a** and **3b**/SLG junctions with tilt angles of θ ≈ 40° and 15° respectively for **3a** and **3b** between Gr sheet and gold.

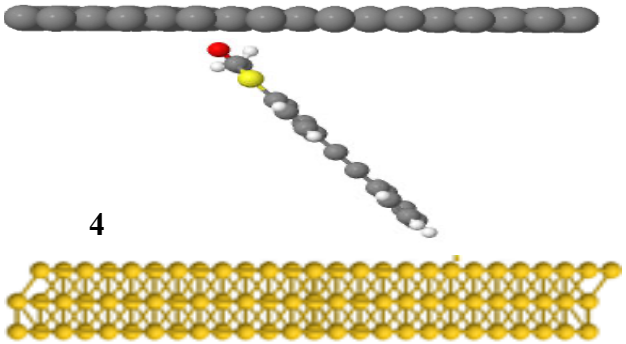

Fig. 4.27: Schematic illustration of Au/**4**/SLG junction with a tilt angle of θ ≈ 40° for molecule **4** between Gr sheet and gold.

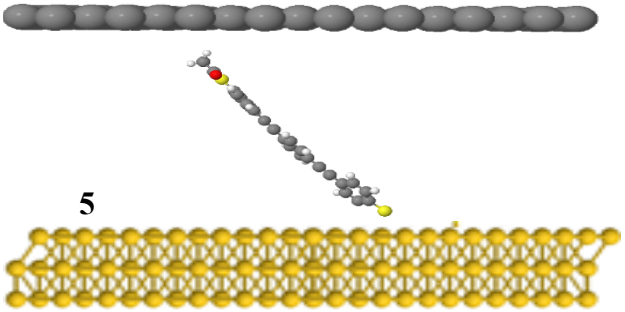

Fig. 4.28: Schematic illustration of Au/**5**/SLG junction with a tilt angle of θ ≈ 40° for molecule **5** between Gr sheet and gold.

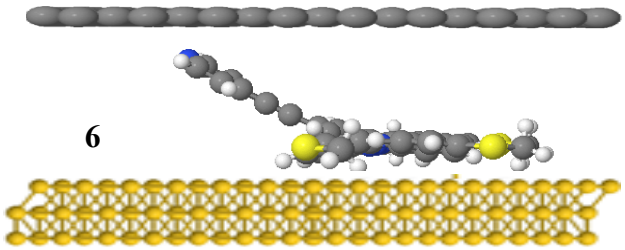

Fig. 4.29: Schematic illustration of Au/**6**/SLG junction with a tilt angle of θ ≈ 42° for molecule **6** between Gr sheet and gold.

4.8 Model of three-terminal junction

In this study, I modelled the three-terminal junction shown in Fig. 4.30, where a single molecule is sandwiched between the three contacts. The in-plane periodicity of the graphene sheet and the molecular layer is achieved by repeating the unit cell using a Bravais lattice with 50k points in the y-direction (see upper black arrow). The gold electrode is modelled as a nanowire attached to each molecule. Fig. 4.30 shows the top contact is SLG and is divided into two electrodes (electrode 1 and electrode 2), whereas the bottom contact is Au (electrode 3). In this case, there are three paths of charge transport between these terminals: the direct path, where the electrons of energy E flow directly from terminal 1 to 2. Path 1-3 for electrons passing from the top-left electrode (lead 1) to the bottom electrode (lead 3), and path 2-3 for electrons travelling from the top-right electrode (lead 2) to the bottom electrode (lead 3), as shown in Fig. 4.30.

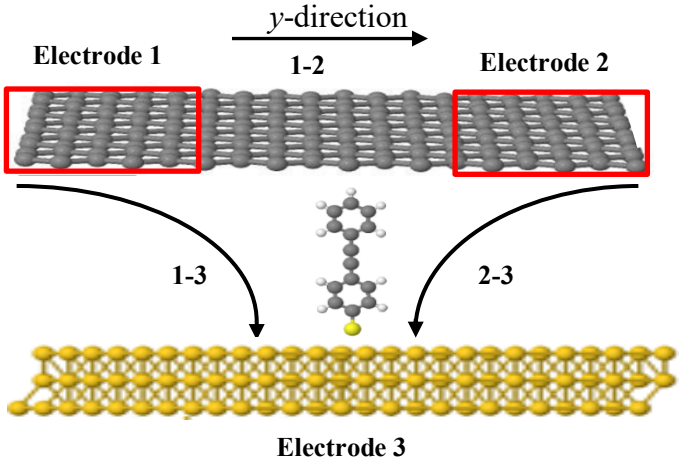

Fig. 4.30: Schematic illustration of a three-terminal junction with periodic boundary conditions along the y-axis. The direct path 1-2: electrons of energy E flow directly from electrode 1 to 2, path 1-3: electrons passing from the top-left electrode (lead 1) to the bottom electrode (lead 3), and path 2-3**:** electrons travelling from the top-right electrode (lead 2) to the bottom electrode (lead 3).

4.9 Transport calculations in a three-terminal junction

To calculate the transmission coefficient $T(E)$of electrons of energy E passing from the graphene to the gold or vice versa, a mean-field Hamiltonian and an overlap matrix were extracted from the converged DFT calculation and combined with the Gollum transport code[53]. In what follows, I shall investigate the charge transport behaviour of the studied molecules **1-6**, whose structures are shown in Fig. 4.4, through an asymmetric junction (i.e., SLG and Au) with two different structures of Au (i.e., flat and cluster).

4.9.1 Au flat surface

As mentioned above, in the three-terminal junction, there are two transmission pathways 1-3 and 2-3 describing the transport between the gold and graphene electrodes (see Fig. 4.31). Since the electron pathways 1-3 and 2-3 have an equal length and therefore yield almost identical transmission coefficients $T(E)$, their average is taken, as shown in Figs. 4.32-4.37. Fig. 4.32 shows the average transmission coefficient $T(E)$ for molecule **1**, whose tilt angle is approximately 40°. This Fig. also reveals that the charge transport through the thiol-terminated molecule takes place in the tail of the HOMO resonance.

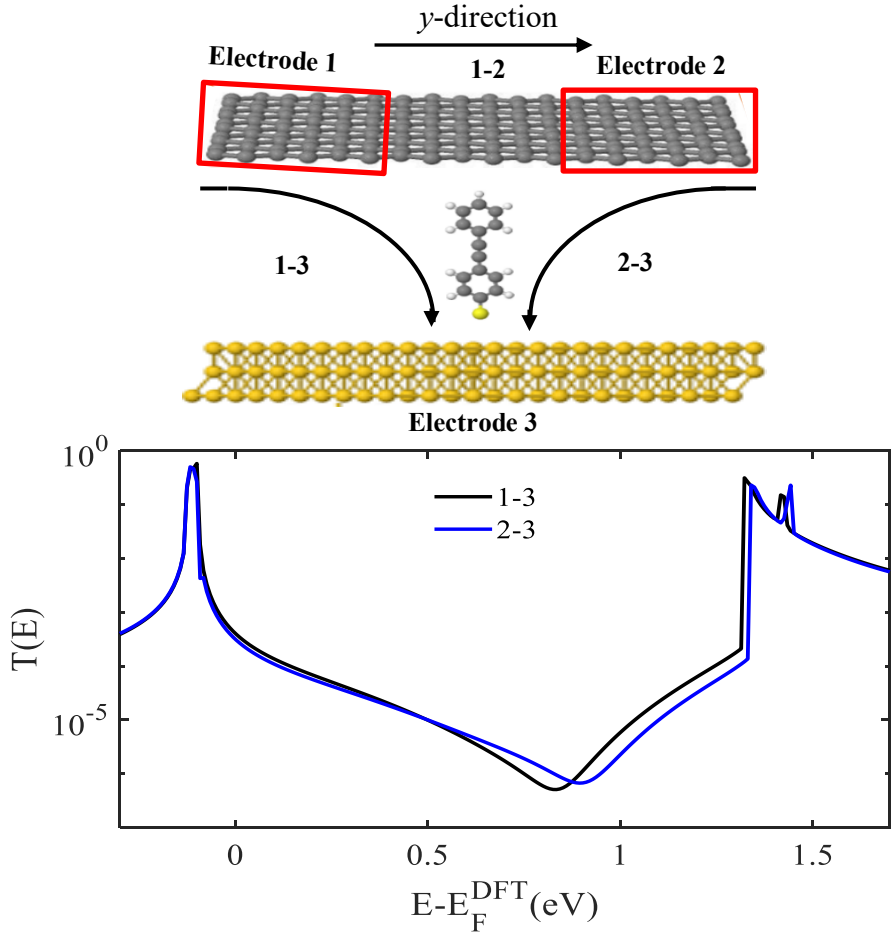

Fig. 4.31: Top panel: Schematic illustration of a three-terminal Au/**1**/SLG junction with periodic boundary conditions along the *y*-axis. The top contact is SLG and is divided into two electrodes (electrode 1 and electrode 2), whereas the bottom contact is Au (electrode 3). Bottom panel: An example of zero-bias transmission coefficient $T(E)$ curves: 1-3 and 2-3 have an equal path length, and therefore have identical curves (black and blue lines).

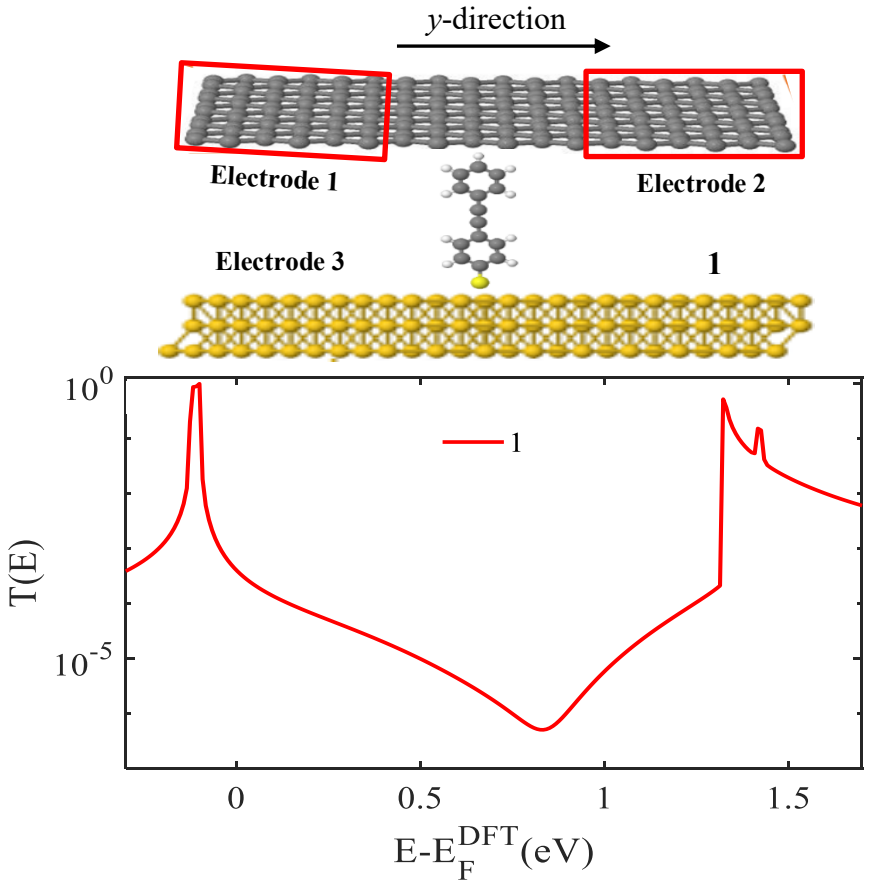

Fig. 4.32: Top panel: Schematic illustration of a three-terminal Au/**1**/SLG junction with periodic boundary conditions along the *y*-axis, as in Fig. 4.31. Bottom panel: Zero-bias transmission coefficient $T(E)$ averaged over the values for paths 1-3 and 2-3 shown in Fig. 4.31.

As previously mentioned, **2** has two different anchors (SAc and Py), meaning that there are two approaches to linking the electrodes in the junction. **2a** is when the thiol binds to Au and pyridine binds to SLG, and **2b**, by flipping the molecule in the junction, is when the pyridine attaches to Au and the thioacetate to the SLG as shown in the top panel of Fig. 4.33. The two anchors are well-known to move energy levels relative to the Fermi energy in an opposite direction. In other words,

SAc produces HOMO-dominated junctions, whereas Py produces LUMO-dominated junctions. In our case the binding energy of thiol to the Au is stronger than that of Py to the SGL (case **2a)** and the DFT-predicted Fermi energy sits so close to the HOMO resonance. The bottom panel of Fig. 4.33 shows that **2b** yields a lower conductance, because the separation between the Au and SLG electrodes is larger than in **2a**.

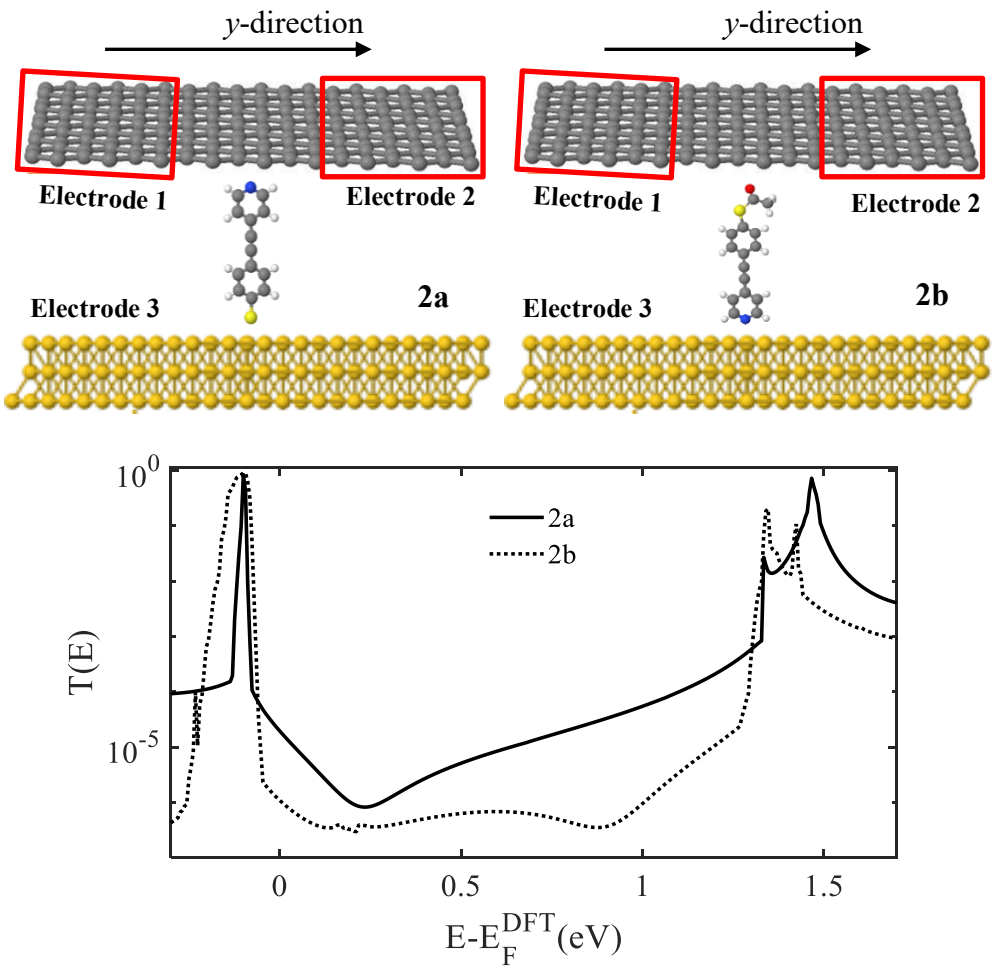

Fig. 4.33: Top panel: Schematic illustration of a three-terminal Au/**2a** or **2b**/SLG junction with periodic boundary conditions along the *y*-axis. Bottom panel: Zero-bias transmission coefficients $T(E)$ of molecule **2** as a function of energy.

Similarly, **3** also has two possibilities in the junction. Configuration **3a** occurs when the thiol binds to Au and pyridine binds to SLG, and **3b** occurs when the molecule is flipped in the junction, with the pyridine binding to Au and the thioacetate binding to the SLG as shown in the top panel of Fig. 4.34. Since the separation distance between the Au and SLG in **3b** is larger than in **3a**, the conductance in case **3b** is lower than that of case **3a.**

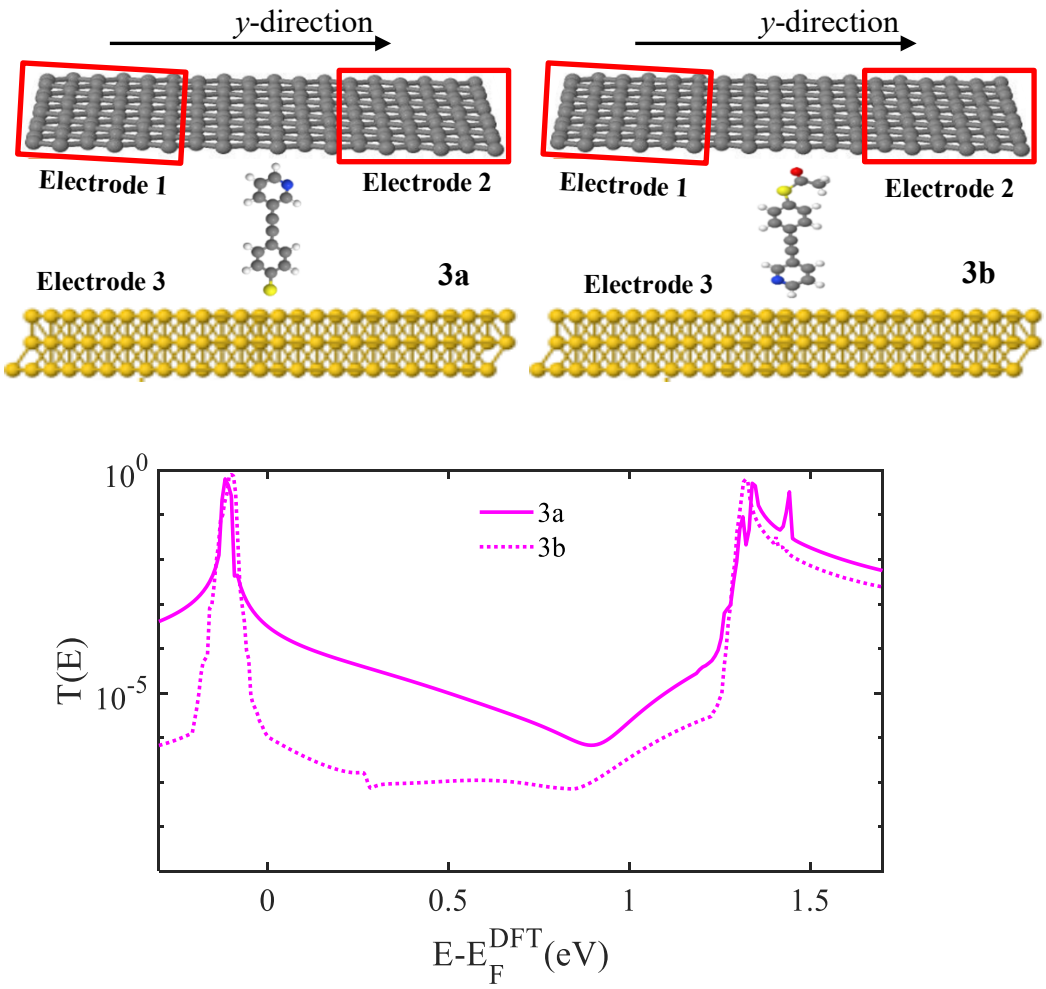

Fig. 4.34: Top panel: Schematic illustration of a three-terminal Au/**3a** or **3b**/SLG junction with periodic boundary conditions along the *y*-axis. Bottom panel: Zero-bias transmission coefficients $T(E)$ of molecule **3** as a function of energy.

The bottom panel of Fig. 4.35 shows the transmission coefficient $T(E)$ as a function of energy E for molecule **4**. It reveals that molecule **4** is a HOMO-dominated, because both anchors (SAc and thiol) are pinning in the same direction toward HOMO resonance.

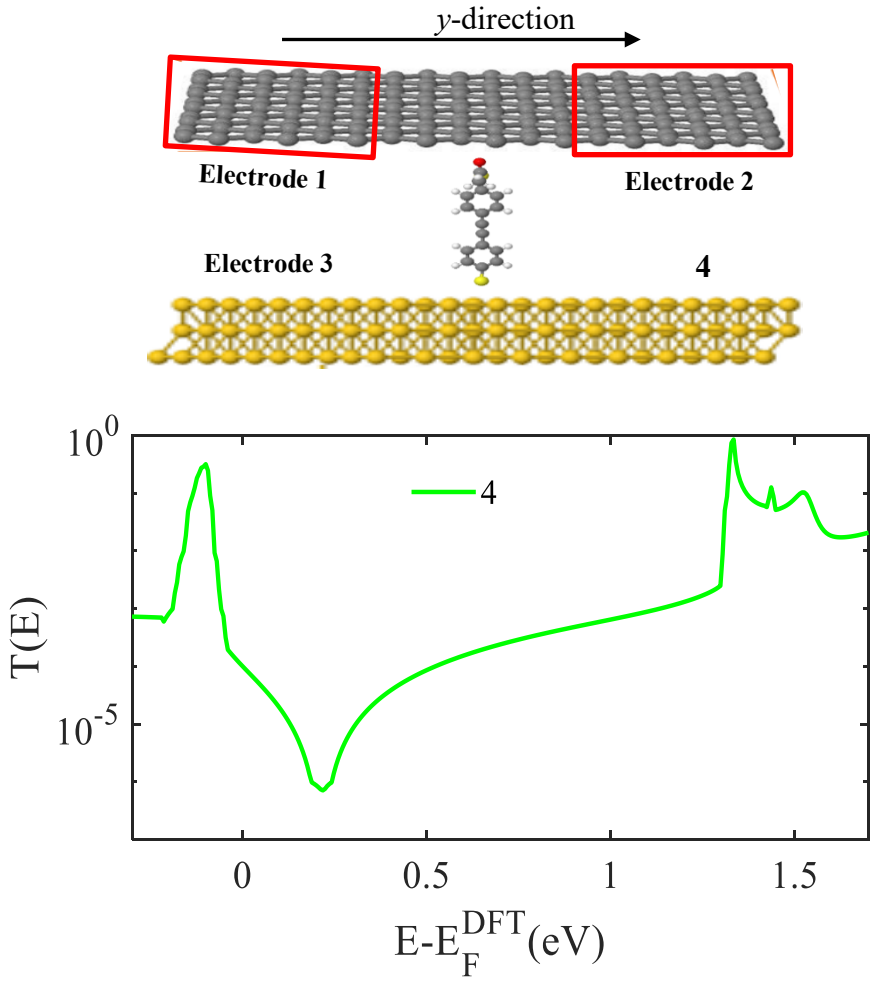

Fig. 4.35: Top panel: Schematic illustration of a three-terminal Au/**4**/SLG junction with periodic boundary conditions along the *y*-axis. Bottom panel: Zero-bias transmission coefficient *T*(*E*) of molecule **4** as a function of energy.

Similarly, the bottom panel of Fig. 4.36 shows the transmission coefficient $T(E)$ as a function of energy for SAM **5.** The HOMO resonance is predicted to be pinned near the Fermi Level of the electrodes due to the presence of the thiol and thioacetate anchor groups.

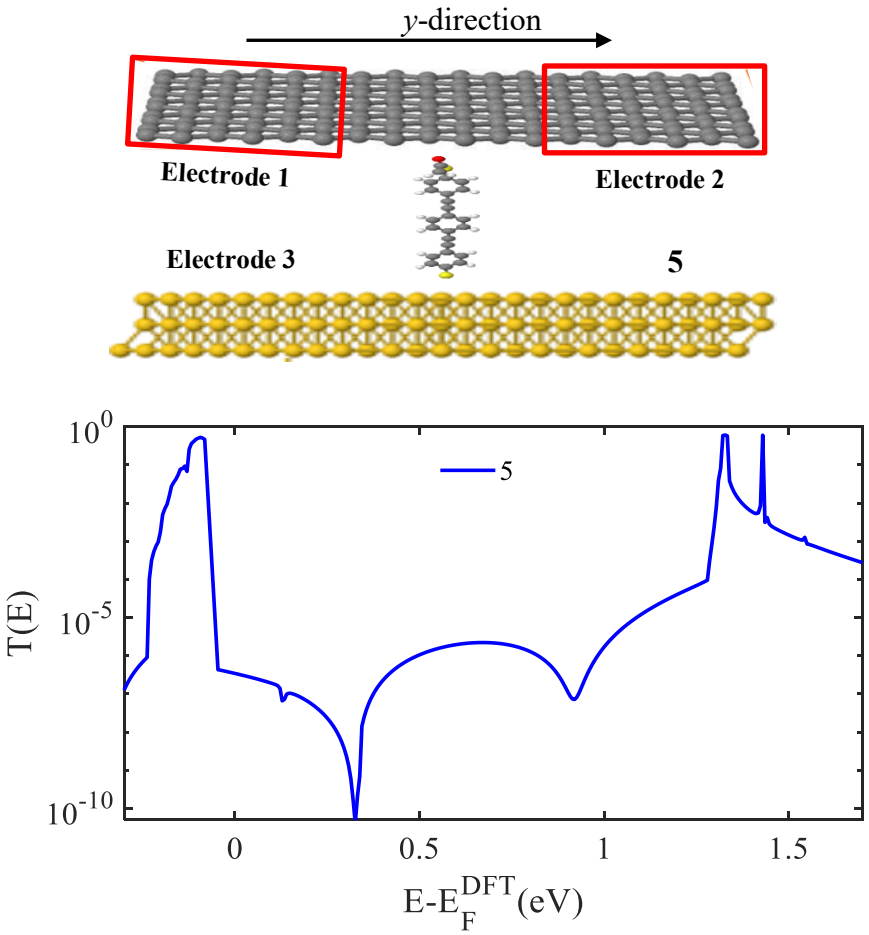

Fig. 4.36: Top panel: Schematic illustration of a three-terminal Au/**5**/SLG junction with periodic boundary conditions along the *y*-axis. Bottom panel: Zero-bias transmission coefficient *T*(*E*) of molecule **5** as a function of energy.

The bottom panel of Fig. 4.37 exhibits a different attitude of molecule **6** compared to the 5 previous molecules, as molecule **6** is a LUMO-dominated at the DFT-predicted Fermi energy ($E\text{-}E_F^{DFT}=0$ eV). This behaviour can be attributed to the presence of the four SMe anchors that bind to Au and Py that binds to the SGL. In other words, these linkers are LUMO-dominated anchors.

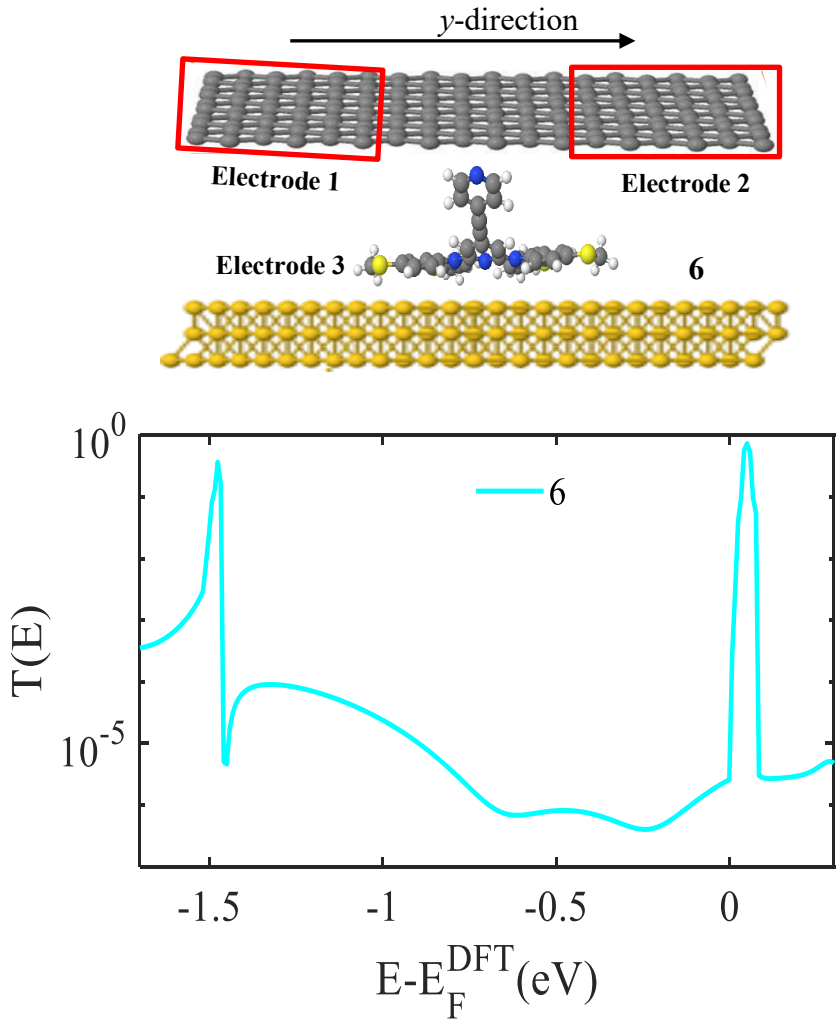

Fig. 4.37: Top panel: Schematic illustration of a three-terminal Au/**6**/SLG junction with periodic boundary conditions along the *y*-axis. Bottom panel: Zero-bias transmission coefficient $T(E)$ of molecule **6** as a function of energy.

Figs. 4.38- a and -b show the transmission coefficients $T(E)$ of studied molecules **1-6** as a function of energy. As shown in Fig. 4.38-**a,** HOMO resonance is predicted to be pinned near the Fermi Level of the electrodes for molecules **1-5**. While the LUMO resonance is predicted to be pinned near the Fermi Level of the electrodes for **6**, as shown in Fig. 4.38-b. It is clear that molecule **5** possesses the lowest conductance among the 5 studied molecules (see Fig. 4.38-a), this trend is expected, because molecule **5** has a longer tunnelling length compared to the others.

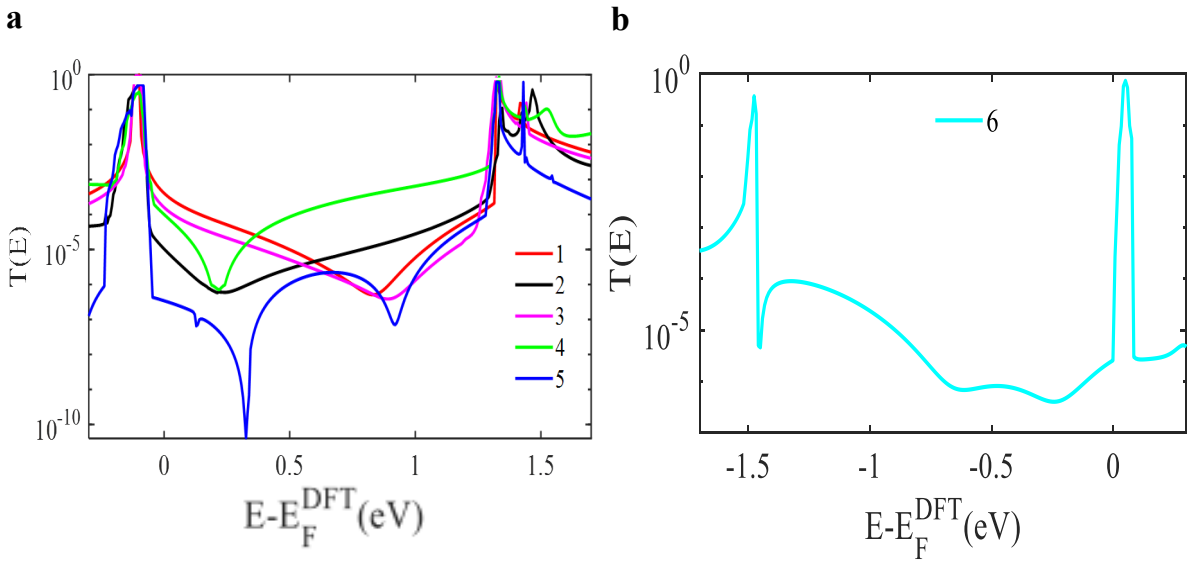

Fig. 4. 38. **a:** Zero-bias transmission coefficient $T(E)$ of molecules **1-5** as a function of energy. The HOMO resonance is predicted to be pinned near the DFT-predicted Fermi energy. **b:** For side-by-side comparison with the other transmission coefficients, this shows the zero-bias transmission coefficient $T(E)$ of **6**, reproduced from Fig. 4.37. The LUMO resonance is predicted to be pinned near the DFT-predicted Fermi energy (flat Au substrate). Note: All the transmission curves here for a flat Au surface.

4.9.2 Au-cluster

To probe the effect of changing the shape of the Au surface on the alignment of the Fermi level, the above transmission function simulations were repeated with the molecules bound to a gold atomic cluster rather than a flat Au substrate (see Figs. 4.39-4.44). Fig. 4.39 demonstrates that the transport is still HOMO dominated for molecule **1**, this means that molecule **1** is insensitive to the shape of the Au surface.

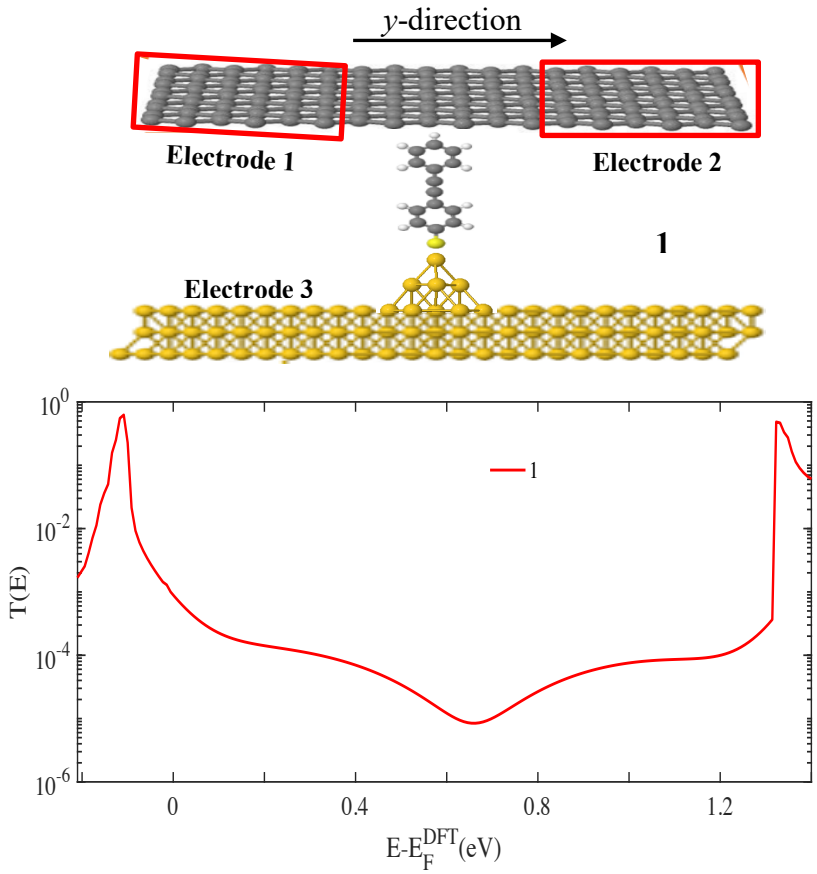

Fig. 4.39: Top panel: Schematic illustration of a three-terminal Au/**1**/SLG junction with periodic boundary conditions along the *y*-axis. The top contact is SLG and is divided into two electrodes (electrode 1 and electrode 2), whereas the bottom contact is an add-atom Au (electrode 3). Bottom panel**:** Zero-bias transmission coefficient $T(E)$ of molecule **1** as a function of energy (insensitive case).

As discussed above, for molecule **2** there are two cases **2a** and **2b**, and the average of their transmission curves was taken, as shown in the bottom panel of Fig. 4.40. The average transmission curve in this figure reveals that the charge transport in these junctions is a LUMO dominated rather than HOMO, which indicates that changing the Au surface from flat to a cluster switches the dominant transport from HOMO to LUMO. Therefore, this proves that molecule **2** is sensitive to the shape of the Au surface.

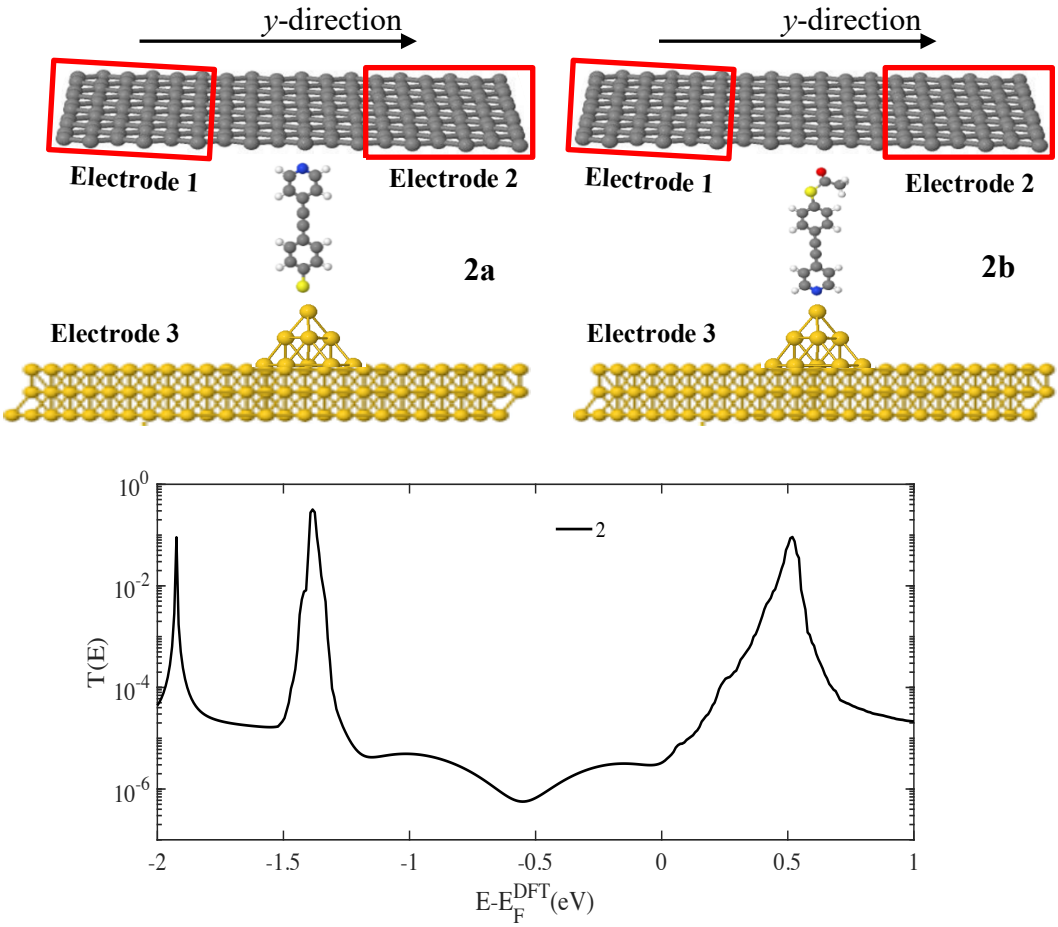

Fig. 4.40: Top panel: Schematic illustration of a three-terminal Au/**2a** or **2b**/SLG junction with periodic boundary conditions along the *y*-axis. The top contact is SLG, whereas the bottom contact is an add-atom Au. Bottom panel**:** Zero-bias transmission coefficient $T(E)$ of molecule **2** as a function of energy (sensitive case). Note: the transmission curve is the average of **2a** and **2b** curves.

Similarly, molecule **3** has two configurations **3a** and **3b**, and the average of their transmission coefficient curves was taken, as shown in the bottom panel of Fig. 4.41, indicating that the electron transport takes place through the LUMO resonance, which means that molecule **3** is also sensitive to the shape of the Au surface.

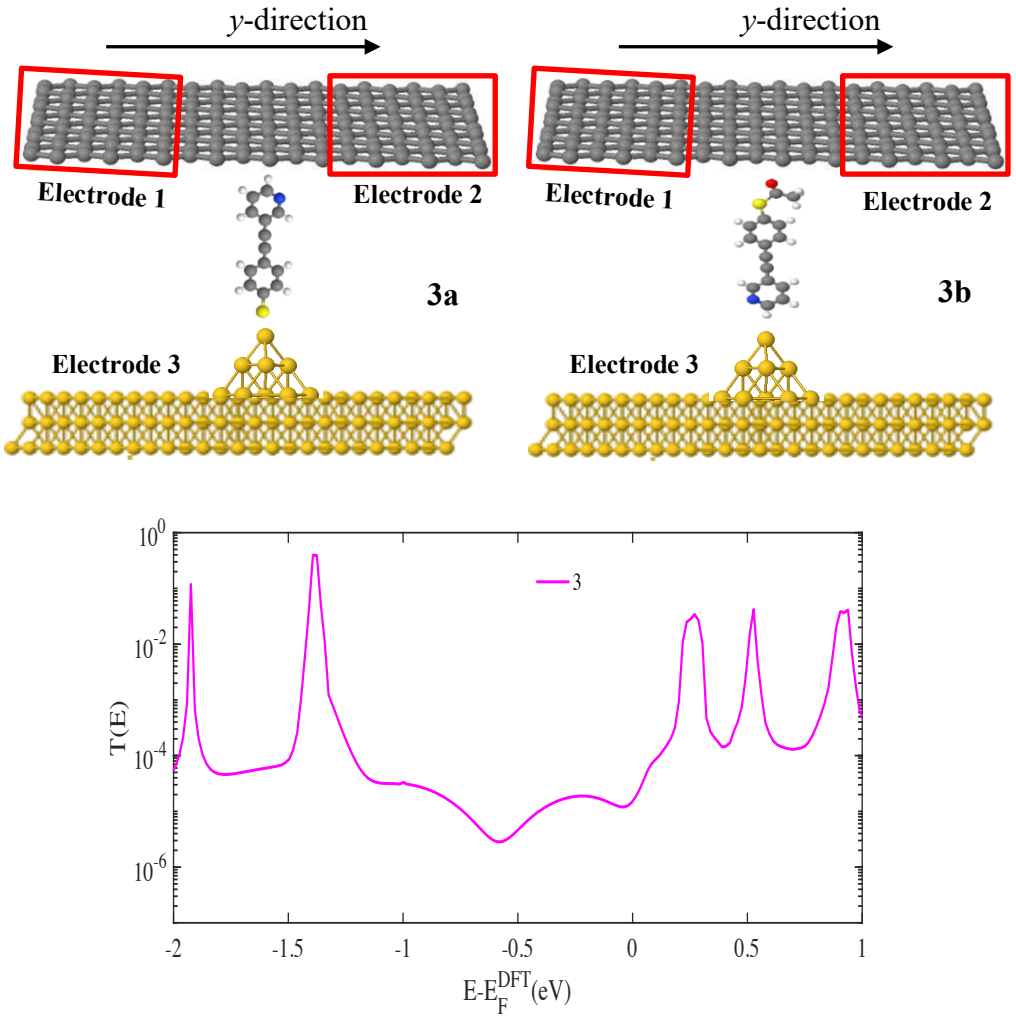

Fig. 4.41: Top panel: Schematic illustration of a three-terminal Au/**3a** or **3b**/SLG junction with periodic boundary conditions along the *y*-axis. The top contact is SLG, whereas the bottom contact is an add-atom Au. Bottom panel**:** Zero-bias transmission coefficient $T(E)$ of molecule **3** as a function of energy (sensitive case). Note: the transmission curve is the average of **3a** and **3b** curves.

Fig. 4.42 shows the transmission curve for molecule **4**, which points out that the transport is still HOMO dominated, as has been previously reported (see Fig. 4.35), demonstrating that molecule **4** is insensitive to the shape of the Au surface.

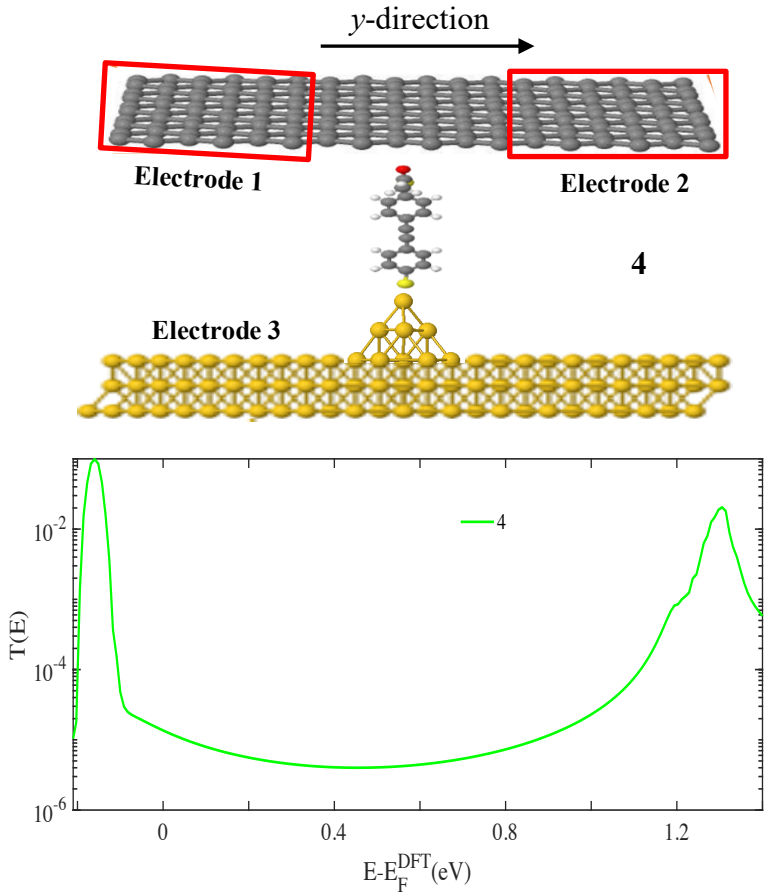

Fig. 4.42: Top panel: Schematic illustration of a three-terminal Au/**4**/SLG junction with periodic boundary conditions along the *y*-axis. The top contact is SLG, whereas the bottom contact is an add-atom Au. Bottom panel: Zero-bias transmission coefficient $T(E)$ of molecule **4** as a function of energy (insensitive case).

Fig. 4.43 shows the transmission curve for molecule **5**, which also reveals that the electrons near the Fermi energy transmitted through the tail of the HOMO, as has been previously reported (see Fig. 4.36), indicating that changing the shape of the Au surface does not have an influence on the alignment of Fermi level for this molecule.

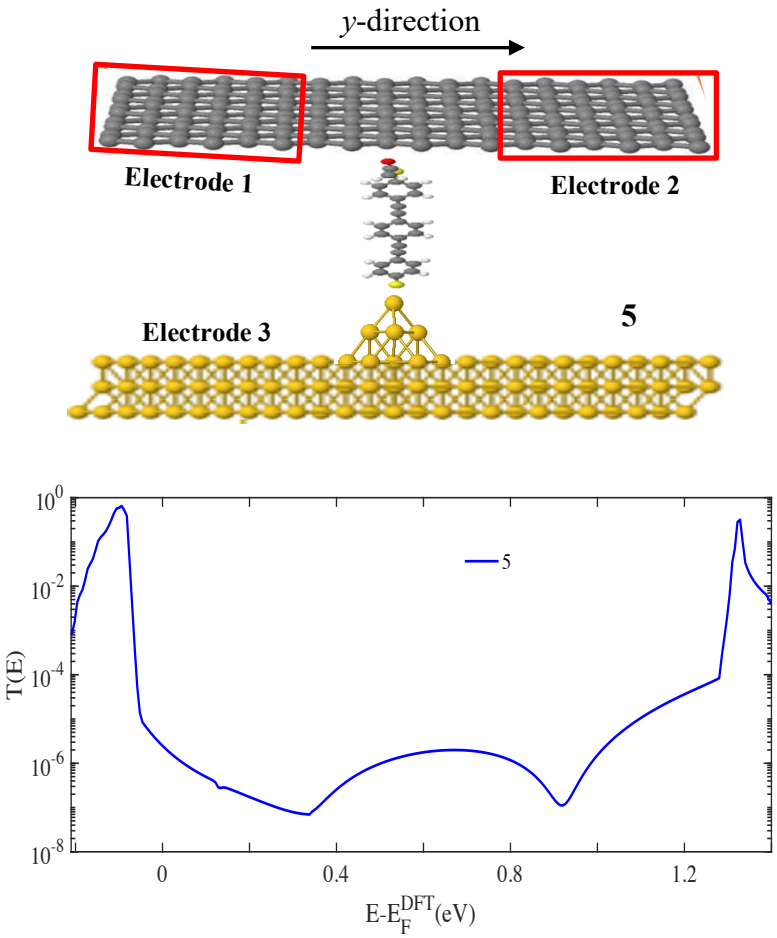

Fig. 4.43: Top panel: Schematic illustration of a three-terminal Au/**5**/SLG junction with periodic boundary conditions along the y-axis. The top contact is SLG, whereas the bottom contact is an add-atom Au. Bottom panel: Zero-bias transmission coefficient $T(E)$ of molecule **5** as a function of energy (insensitive case).

Fig. 4.44 shows the calculated transmission coefficient of molecule **6**, which implies that the LUMO resonance pinned close to the DFT-predicted Fermi energy. A similar behavior was obtained in the flat Au substrate, as discussed above (see Fig. 4.37), which means molecule **6** is insensitive to the shape of the Au surface.

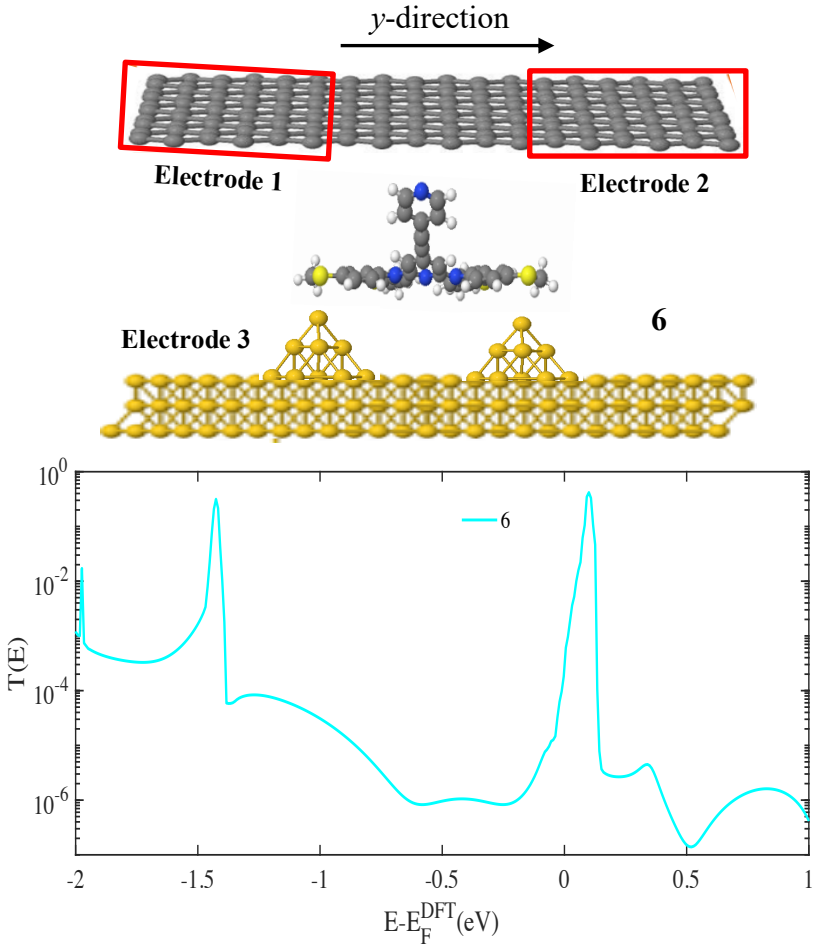

Fig. 4.44: Top panel: Schematic illustration of a three-terminal Au/**6**/SLG junction with periodic boundary conditions along the *y*-axis. The top contact is SLG, whereas the bottom contact is an add-atom Au. Bottom panel: Zero-bias transmission coefficient $T(E)$ of molecule **6** as a function of energy (insensitive case).

The above transmission function calculations of molecules **1-6** (Figs. 4.39-4.44) are summarized in Figs.4.45-a and -b. These curves demonstrate that **1**, **4**, **5** and **6** are insensitive molecules to the shape of the Au surface whereas the rest are sensitive. Molecules **2** and **3** are the sensitive ones (which have pyridyl anchors), because they switch from HOMO to LUMO by changing the Au substrate from flat gold to a cluster. (See Figs. 4.38, 4.45). It is well known that the position of the energy levels relative to the Fermi energy depends on charge transport between the electrode and the molecule, which means if the electrons transfer from the electrode to the molecule, the energy level goes down and vice versa. For molecules **2** and **3**, which have Py anchor, the electrons transfer from the gold cluster to the molecule, hence the energy level goes down, which leads to switching the transport from HOMO to LUMO. In other words, the charge transfer for these molecules depends on the shape of the gold electrode

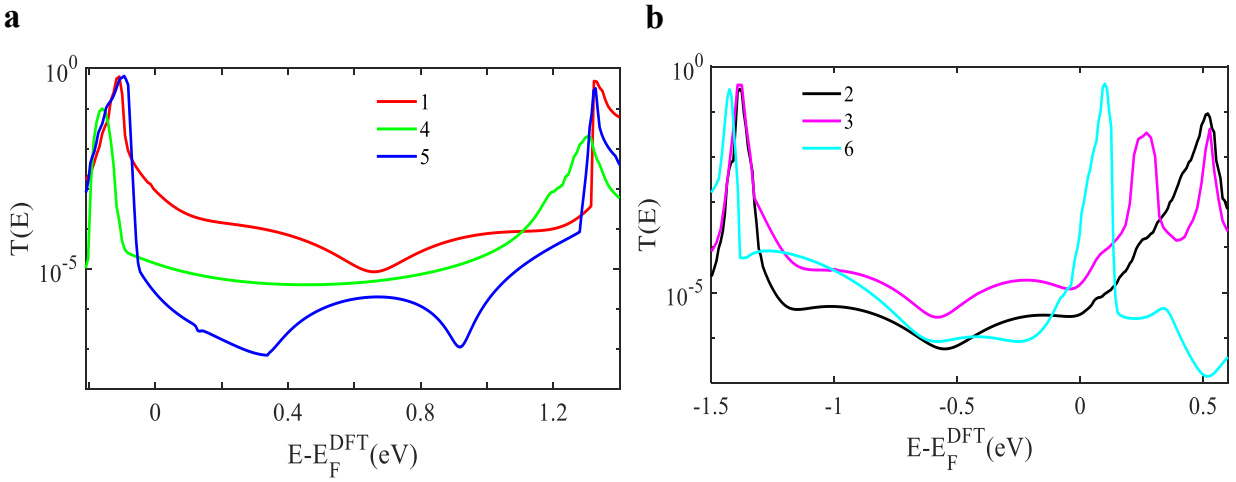

Fig. 4.45. **a:** Zero-bias transmission coefficient $T(E)$ of molecules **1, 4** and **5** as a function of energy, the HOMO resonance is predicted to be pinned near the DFT-predicted Fermi energy. **b:** Zero-bias transmission coefficient $T(E)$ of **2, 3** and **6,** the LUMO resonance is predicted to be pinned near the DFT-predicted Fermi energy (add-atom Au substrate).

4.10 Conclusion

In this chapter, the charge transport mechanism of six OPE-based molecules has been studied using a three-terminal junction. The binding energies between different anchors including (SH, Py, SMe and SAc) and two-contact electrodes (Au and Gr) have been explored, and the results indicate that the thiol anchor exhibits strong binding to the Au compared to the others due to the strong covalent bond. In terms of the electrode material, these anchors bind much weakly to the Gr sheet than to Au due to the weak Van der Waals interactions between Gr and anchors. To probe the impact of the shape of the Au surface on the alignment of the molecular energy levels relative to the Fermi energy level of the electrode, I first studied the charge transport behaviour through SLG/molecule/Au-flat. I have demonstrated that the transmission coefficients near the DFT-predicted Fermi energy ($E\text{-}E_F^{DFT}$=0 eV) for molecules **1-5** are HOMO-dominated, whereas **6** is LUMO-dominated due to the presence of SMe and Py anchors. Then, I repeated the transmission function calculations, where the molecules were bound to a gold atomic cluster. I found that the HOMO resonance is pinned near the DFT-predicted Fermi energy ($E\text{-}E_F^{DFT}$=0 eV), while for molecules **2**, **3** and **6** the LUMO resonance is pinned near the DFT-predicted Fermi energy ($E\text{-}E_F^{DFT}$=0 eV). This indicates that 4 molecules are insensitive to the shape of the Au surface, whereas two are sensitive. Molecules **2** and **3** (pyridyl anchors) are sensitive, because they switch from HOMO to LUMO by changing the Au substrate from flat gold to a cluster. In other words, the relative position of E_F for molecules **2** and **3** depends on whether the gold is flat or possesses a gold cluster at the molecule-gold contact.

4.11 Bibliography

(1) Herrer, L.; Ismael, A.; Martín, S.; Milan, D. C.; Serrano, J. L.; Nichols, R. J.; Lambert, C.; Cea, P. Single Molecule vs. Large Area Design of Molecular Electronic Devices Incorporating an Efficient 2-Aminepyridine Double Anchoring Group. *Nanoscale* **2019**, *11* (34), 15871–15880.

(2) Wu, Q.; Sadeghi, H.; García-Suárez, V. M.; Ferrer, J.; Lambert, C. J. Thermoelectricity in Vertical Graphene-C60-Graphene Architectures. *Sci. Rep.* **2017**, *7* (1), 11680.

(3) Love, J. C.; Estroff, L. A.; Kriebel, J. K.; Nuzzo, R. G.; Whitesides, G. M. Self-Assembled Monolayers of Thiolates on Metals as a Form of Nanotechnology. *Chem. Rev.* **2005**, *105* (4), 1103–1170.

(4) Zhao, S.; Chen, H.; Qian, Q.; Zhang, H.; Yang, Y.; Hong, W. Non-Covalent Interaction-Based Molecular Electronics with Graphene Electrodes. *Nano Res.* **2021**.

(5) Xiang, D.; Wang, X.; Jia, C.; Lee, T.; Guo, X. Molecular-Scale Electronics: From Concept to Function. *Chem. Rev.* **2016**, *116* (7), 4318–4440.

(6) Ulman, A. Formation and Structure of Self-Assembled Monolayers. *Chem. Rev.* **1996**, *96* (4), 1533–1554.

(7) Li, X.; Tan, Z.; Huang, X.; Bai, J.; Liu, J.; Hong, W. Experimental Investigation of Quantum Interference in Charge Transport through Molecular Architectures. *J. Mater. Chem. C* **2019**, *7* (41), 12790–12808.

(8) Carlotti, M.; Kovalchuk, A.; Wächter, T.; Qiu, X.; Zharnikov, M.; Chiechi, R. C. Conformation-Driven Quantum Interference Effects Mediated by through-Space Conjugation in Self-Assembled Monolayers. *Nat. Commun.* **2016**, *7* (1), 13904.

(9) Wei, Z.; Li, T.; Jennum, K.; Santella, M.; Bovet, N.; Hu, W.; Nielsen, M. B.; Bjørnholm, T.; Solomon, G. C.; Laursen, B. W.; Nørgaard, K. Molecular Junctions Based on SAMs of Cruciform Oligo(Phenylene Ethynylene)s. *Langmuir* **2012**, *28* (8), 4016–4023.

(10) Sun, Y.-Y.; Peng, Z.-L.; Hou, R.; Liang, J.-H.; Zheng, J.-F.; Zhou, X.-Y.; Zhou, X.-S.; Jin, S.; Niu, Z.-J.; Mao, B.-W. Enhancing Electron Transport in Molecular Wires by Insertion of a Ferrocene Center. *Phys. Chem. Chem. Phys.* **2014**, *16* (6), 2260.

(11) Obersteiner, V.; Egger, D. A.; Zojer, E. Impact of Anchoring Groups on Ballistic Transport: Single Molecule vs Monolayer Junctions. *J. Phys. Chem. C* **2015**, *119* (36), 21198–21208.

(12) Ismael, A. K.; Lambert, C. J. Molecular-Scale Thermoelectricity: A Worst-Case Scenario. *Nanoscale Horiz.* **2020**, *5* (7), 1073–1080.

(13) Zotti, L. A.; Kirchner, T.; Cuevas, J.-C.; Pauly, F.; Huhn, T.; Scheer, E.; Erbe, A. Revealing the Role of Anchoring Groups in the Electrical Conduction Through Single-Molecule Junctions. *Small* **2010**, *6* (14), 1529–1535.

(14) Gupta, N. K.; Schultz, T.; Karuppannan, S. K.; Vilan, A.; Koch, N.; Nijhuis, C. A. The Energy Level Alignment of the Ferrocene–EGaIn Interface Studied with Photoelectron Spectroscopy. *Phys. Chem. Chem. Phys.* **2021**, *23* (24), 13458–13467.

(15) Xin, N.; Li, X.; Jia, C.; Gong, Y.; Li, M.; Wang, S.; Zhang, G.; Yang, J.; Guo, X. Tuning Charge Transport in Aromatic-Ring Single-Molecule Junctions via Ionic-Liquid Gating. *Angew. Chem. Int. Ed.* **2018**, *57* (43), 14026–14031.

(16) Famili, M.; Jia, C.; Liu, X.; Wang, P.; Grace, I. M.; Guo, J.; Liu, Y.; Feng, Z.; Wang, Y.; Zhao, Z.; Decurtins, S.; Häner, R.; Huang, Y.; Liu, S.-X.; Lambert, C. J.; Duan, X. Self-Assembled Molecular-Electronic Films Controlled by Room Temperature Quantum Interference. *Chem* **2019**, *5* (2), 474–484.

(17) Ghosh, A. W.; Rakshit, T.; Datta, S. Gating of a Molecular Transistor: Electrostatic and Conformational. *Nano Lett.* **2004**, *4* (4), 565–568.

(18) Li, Y.; Buerkle, M.; Li, G.; Rostamian, A.; Wang, H.; Wang, Z.; Bowler, D. R.; Miyazaki, T.; Xiang, L.; Asai, Y.; Zhou, G.; Tao, N. Gate Controlling of Quantum Interference and Direct Observation of Anti-Resonances in Single Molecule Charge Transport. *Nat. Mater.* **2019**, *18* (4), 357–363.

(19) Jia, C.; Grace, I. M.; Wang, P.; Almeshal, A.; Huang, Z.; Wang, Y.; Chen, P.; Wang, L.; Zhou, J.; Feng, Z.; Zhao, Z.; Huang, Y.; Lambert, C. J.; Duan, X. Redox Control of Charge Transport in Vertical Ferrocene Molecular Tunnel Junctions. *Chem* **2020**, *6* (5), 1172–1182.

(20) Britnell, L.; Gorbachev, R. V.; Jalil, R.; Belle, B. D.; Schedin, F.; Mishchenko, A.; Georgiou, T.; Katsnelson, M. I.; Eaves, L.; Morozov, S. V.; Peres, N. M. R.; Leist, J.; Geim, A. K.; Novoselov, K. S.; Ponomarenko, L. A. Field-Effect Tunneling Transistor Based on Vertical Graphene Heterostructures. *Science* **2012**, *335* (6071), 947–950.

(21) Tian, T.; Rice, P.; Santos, E. J. G.; Shih, C.-J. Multiscale Analysis for Field-Effect Penetration through Two-Dimensional Materials. *Nano Lett.* **2016**, *16* (8), 5044–5052.

(22) Jia, C.; Famili, M.; Carlotti, M.; Liu, Y.; Wang, P.; Grace, I. M.; Feng, Z.; Wang, Y.; Zhao, Z.; Ding, M.; Xu, X.; Wang, C.; Lee, S.-J.; Huang, Y.; Chiechi, R. C.; Lambert, C. J.; Duan, X. Quantum Interference Mediated Vertical Molecular Tunneling Transistors. *Sci. Adv.* **2018**, *4* (10), eaat8237.

(23) Kim, Y.; Jeong, W.; Kim, K.; Lee, W.; Reddy, P. Electrostatic Control of Thermoelectricity in Molecular Junctions. *Nat. Nanotechnol.* **2014**, *9* (11), 881–885.

(24) Kim, Y.; Jeong, W.; Kim, K.; Lee, W.; Reddy, P. Electrostatic Control of Thermoelectricity in Molecular Junctions. *Nat. Nanotechnol.* **2014**, *9* (11), 881–885.

(25) Xiang, D.; Jeong, H.; Kim, D.; Lee, T.; Cheng, Y.; Wang, Q.; Mayer, D. Three-Terminal Single-Molecule Junctions Formed by Mechanically Controllable Break Junctions with Side Gating. *Nano Lett.* **2013**, *13* (6), 2809–2813.

(26) Markin, A.; Ismael, A. K.; Davidson, R. J.; Milan, D. C.; Nichols, R. J.; Higgins, S. J.; Lambert, C. J.; Hsu, Y.-T.; Yufit, D. S.; Beeby, A. Conductance Behavior of Tetraphenyl-Aza-BODIPYs. *J. Phys. Chem. C* **2020**, *124* (12), 6479–6485.

(27) Davidson, R. J.; Milan, D. C.; Al-Owaedi, O. A.; Ismael, A. K.; Nichols, R. J.; Higgins, S. J.; Lambert, C. J.; Yufit, D. S.; Beeby, A. Conductance of 'Bare-Bones' Tripodal Molecular Wires. *RSC Adv.* **2018**, *8* (42), 23585–23590.

(28) Ismael, A. K.; Lambert, C. J. Single-Molecule Conductance Oscillations in Alkane Rings. *J. Mater. Chem. C* **2019**, *7* (22), 6578–6581.

(29) Milan, D. C.; Krempe, M.; Ismael, A. K.; Movsisyan, L. D.; Franz, M.; Grace, I.; Brooke, R. J.; Schwarzacher, W.; Higgins, S. J.; Anderson, H. L. The Single-Molecule Electrical Conductance of a Rotaxane-Hexayne Supramolecular Assembly. *Nanoscale* **2017**, *9* (1), 355–361.

(30) Herrer, I. L.; Ismael, A. K.; Milan, D. C.; Vezzoli, A.; Martín, S.; Gonzalez-Orive, A.; Grace, I.; Lambert, C.; Serrano, J. L.; Nichols, R. J. Unconventional Single-Molecule Conductance Behavior for a New Heterocyclic Anchoring Group: Pyrazolyl. *J. Phys. Chem. Lett.* **2018**, *9* (18), 5364–5372.

(31) Wang, X.; Ismael, A.; Almutlg, A.; Alshammari, M.; Al-Jobory, A.; Alshehab, A.; Bennett, T. L.; Wilkinson, L. A.; Cohen, L. F.; Long, N. J. Optimised Power Harvesting by Controlling the Pressure Applied to Molecular Junctions. *Chem. Sci.* **2021**, *12* (14), 5230–5235.

(32) González, M. T.; Ismael, A. K.; Garcia-Iglesias, M.; Leary, E.; Rubio-Bollinger, G.; Grace, I.; Gonzalez-Rodriguez, D.; Torres, T.; Lambert, C. J.; Agrait, N. Interference Controls Conductance in Phthalocyanine Molecular Junctions. *J. Phys. Chem. C* **2021**, *125* (27), 15035–15043.

(33) Mol, J. A.; Lau, C. S.; Lewis, W. J. M.; Sadeghi, H.; Roche, C.; Cnossen, A.; Warner, J. H.; Lambert, C. J.; Anderson, H. L.; Briggs, G. A. D. Graphene-Porphyrin Single-Molecule Transistors. *Nanoscale* **2015**, *7* (31), 13181–13185.

(34) Perrin, M. L.; Burzurí, E.; van der Zant, H. S. J. Single-Molecule Transistors. *Chem. Soc. Rev.* **2015**, *44* (4), 902–919.

(35) Park, H.; Lim, A. K. L.; Alivisatos, A. P.; Park, J.; McEuen, P. L. Fabrication of Metallic Electrodes with Nanometer Separation by Electromigration. *Appl. Phys. Lett.* **1999**, *75* (2), 301–303.

(36) van der Zant, H. S. J.; Kervennic, Y.-V.; Poot, M.; O'Neill, K.; de Groot, Z.; Thijssen, J. M.; Heersche, H. B.; Stuhr-Hansen, N.; Bjørnholm, T.; Vanmaekelbergh, D.; van Walree, C. A.; Jenneskens, L. W. Molecular Three-Terminal Devices: Fabrication and Measurements. *Faraday Discuss* **2006**, *131*, 347–356.

(37) Ismael, A. K.; Wang, K.; Vezzoli, A.; Al-Khaykanee, M. K.; Gallagher, H. E.; Grace, I. M.; Lambert, C. J.; Xu, B.; Nichols, R. J.; Higgins, S. J. Side-group-mediated Mechanical Conductance Switching in Molecular Junctions. *Angew. Chem. Int. Ed.* **2017**, *56* (48), 15378–15382.

(38) Li, S.; Yu, H.; Schwieter, K.; Chen, K.; Li, B.; Liu, Y.; Moore, J. S.; Schroeder, C. M. Charge Transport and Quantum Interference Effects in Oxazole-Terminated Conjugated Oligomers. *J. Am. Chem. Soc.* **2019**, *141* (40), 16079–16084.

(39) Ismael, A. K.; Al-Jobory, A.; Grace, I.; Lambert, C. J. Discriminating Single-Molecule Sensing by Crown-Ether-Based Molecular Junctions. *J. Chem. Phys.* **2017**, *146* (6), 064704.

(40) Kaliginedi, V.; V. Rudnev, A.; Moreno-García, P.; Baghernejad, M.; Huang, C.; Hong, W.; Wandlowski, T. Promising Anchoring Groups for Single-Molecule Conductance Measurements. *Phys Chem Chem Phys* **2014**, *16* (43), 23529–23539.

(41) Frisenda, R.; Tarkuç, S.; Galán, E.; Perrin, M. L.; Eelkema, R.; Grozema, F. C.; van der Zant, H. S. J. Electrical Properties and Mechanical Stability of Anchoring Groups for Single-Molecule Electronics. *Beilstein J. Nanotechnol.* **2015**, *6*, 1558–1567.

(42) Hong, W.; Manrique, D. Z.; Moreno-García, P.; Gulcur, M.; Mishchenko, A.; Lambert, C. J.; Bryce, M. R.; Wandlowski, T. Single Molecular Conductance of Tolanes: Experimental and Theoretical Study on the Junction Evolution Dependent on the Anchoring Group. *J. Am. Chem. Soc.* **2012**, *134* (4), 2292–2304.

(43) O'Driscoll, L. J.; Bryce, M. R. A Review of Oligo(Arylene Ethynylene) Derivatives in Molecular Junctions. *Nanoscale* **2021**, *13* (24), 10668–10711.

(44) Valkenier, H.; Huisman, E. H.; van Hal, P. A.; de Leeuw, D. M.; Chiechi, R. C.; Hummelen, J. C. Formation of High-Quality Self-Assembled Monolayers of Conjugated Dithiols on Gold: Base Matters. *J. Am. Chem. Soc.* **2011**, *133* (13), 4930–4939.

(45) Tour, J. M.; Jones, L.; Pearson, D. L.; Lamba, J. J. S.; Burgin, T. P.; Whitesides, G. M.; Allara, D. L.; Parikh, A. N.; Atre, S. Self-Assembled Monolayers and Multilayers of Conjugated Thiols, .Alpha.,.Omega.-Dithiols, and Thioacetyl-Containing Adsorbates. Understanding Attachments between Potential Molecular Wires and Gold Surfaces. *J. Am. Chem. Soc.* **1995**, *117* (37), 9529–9534.

(46) Salam, L. B.; Ilori, M. O.; Amund, O. O. Properties, Environmental Fate and Biodegradation of Carbazole. *3 Biotech* **2017**, *7* (2), 111.

(47) Pérez-Rentero, S.; Grijalvo, S.; Ferreira, R.; Eritja, R. Synthesis of Oligonucleotides Carrying Thiol Groups Using a Simple Reagent Derived from Threoninol. *Molecules* **2012**, *17* (9), 10026–10045.

(48) O'Driscoll, L. J.; Wang, X.; Jay, M.; Batsanov, A. S.; Sadeghi, H.; Lambert, C. J.; Robinson, B. J.; Bryce, M. R. Carbazole-Based Tetrapodal Anchor Groups for Gold Surfaces: Synthesis and Conductance Properties. *Angew. Chem. Int. Ed.* **2020**, *59* (2), 882–889.

(49) Artacho, E.; Anglada, E.; Diéguez, O.; Gale, J. D.; García, A.; Junquera, J.; Martin, R. M.; Ordejón, P.; Pruneda, J. M.; Sánchez-Portal, D.; Soler, J. M. The SIESTA Method; Developments and Applicability. *J. Phys. Condens. Matter* **2008**, *20* (6), 064208.

(50) Soler, J. M.; Artacho, E.; Gale, J. D.; García, A.; Junquera, J.; Ordejón, P.; Sánchez-Portal, D. The SIESTA Method for *Ab Initio* Order- *N* Materials Simulation. *J. Phys. Condens. Matter* **2002**, *14* (11), 2745–2779.

(51) Milan, D. C.; Krempe, M.; Ismael, A. K.; Movsisyan, L. D.; Franz, M.; Grace, I.; Brooke, R. J.; Schwarzacher, W.; Higgins, S. J.; Anderson, H. L.; Lambert, C. J.; Tykwinski, R. R.; Nichols, R. J. The Single-Molecule Electrical Conductance of a Rotaxane-Hexayne Supramolecular Assembly. *Nanoscale* **2017**, *9* (1), 355–361.

(52) Wang, X.; Bennett, T. L. R.; Ismael, A.; Wilkinson, L. A.; Hamill, J.; White, A. J. P.; Grace, I. M.; Kolosov, O. V.; Albrecht, T.; Robinson, B. J.; Long, N. J.; Cohen, L. F.; Lambert, C. J. Scale-Up of Room-Temperature Constructive Quantum Interference from Single Molecules to Self-Assembled Molecular-Electronic Films. *J. Am. Chem. Soc.* **2020**, *142* (19), 8555–8560.

(53) Ferrer, J.; Lambert, C. J.; García-Suárez, V. M.; Manrique, D. Z.; Visontai, D.; Oroszlany, L.; Rodríguez-Ferradás, R.; Grace, I.; Bailey, S. W. D.; Gillemot, K.; Sadeghi, H.; Algharagholy, L. A. GOLLUM: A next-Generation Simulation Tool for Electron, Thermal and Spin Transport. *New J. Phys.* **2014**, *16* (9), 093029.

Chapter 5

The Thermoelectric Properties of Oligo (phenylene-ethynylene) Derivatives

The measurement of the Seebeck coefficient in molecular junctions offers complementary information to conductance measurements and is becoming essential for the understanding of transport processes at the nanoscale. In this chapter, the thermoelectric properties of the molecules discussed in chapter 4, oligo (phenylethylene) OPE-based molecules, are examined theoretically. I demonstrate that changing the shape of the gold surface can affect the sign of the Seebeck coefficient.

5.1 Introduction

Thermoelectricity enables direct conversion of waste heat into electric energy and open a new way to harvest new environmentally friendly energy for energy-saving recycling[1–3]. Studies of charge and heat transport in single-molecule junctions are of great fundamental importance as they provide additional insights into the electronic structure of junctions and their transport properties[1]. It is worth mentioning that the thermoelectric properties of single-molecule junctions can be modified by manipulating their transport properties such as increasing the length of the molecule [4–6], changing the molecule-electrode coupling geometry[7,8] and chemical doping of the molecule[9,10]. This chapter aims to explore the effect of changing the shape of the gold surface on the sign of the Seebeck coefficient of the molecules studied in chapter 4. In what follows, I will present a brief overview of the Seebeck coefficient as a physical concept. Subsequently, the Seebeck coefficient

is investigated for molecules **1**-**6** trapped between SLG and the flat Au surface. Finally, it is examined again by changing the shape of Au from flat to cluster.

5.2 Seebeck coefficient

As mentioned above, thermoelectric effect describes the direct conversion between thermal and electric energies, when there is a temperature difference $\Delta T$and voltage difference ΔVacross, leading to an electric current I and heat current Q passing through a system. Therefore, in the regime of linear response, the electric current I and heat flow Q are related to the temperature ΔT and voltage differences ΔV by the following equation[11]

$$\binom{I}{Q} = \frac{2}{h}\begin{pmatrix} e^2 L_o & \frac{e}{T}L_1 \\ eL_1 & L_2 \end{pmatrix}\binom{\Delta V}{\Delta T} \tag{5.1}$$

where T is the reference temperature, e is the electronic charge

$$L_n = \int_{-\infty}^{\infty}(E - E_F)^n T(E)\left(-\frac{\partial f(E,T)}{\partial E}\right) dE \tag{5.2}$$

In this expression $T(E)$ is the transmission coefficient for electrons of energy E passing through the molecule from one electrode to other, and $f(E,T)$ is the Fermi energy distribution defined as $f(E,T) = \left[e^{(E-E_F)/k_BT} + 1\right]^{-1}$ where k_B is Boltzmann's constant.

When $\Delta T = 0$, equation (5.1) yields for the electrical conductance

$$G = \left(\frac{I}{\Delta V}\right)_{\Delta T=0},\ G = \frac{2e^2}{h}\,L_o \tag{5.3}$$

Similarly, when $I = 0$ equation yields for the Seebeck coefficient

$$S = -\left(\frac{\Delta V}{\Delta T}\right)_{I=0},\ S = \frac{-1}{e\,T}\,\frac{L_1}{L_o} \tag{5.4}$$

When the temperature is low enough, $T(E)$ varies approximately linearly with E on the scale of k_BT, then these expressions take the form

$$G \approx \left(\frac{2e^2}{h}\right) T(E_F) \tag{5.5}$$

$$S \approx -\alpha|e|\, T \left(\frac{dlnT(E)}{dE}\right)_{E=E_F} \tag{5.6}$$

where $\alpha = \left(\frac{k_B}{e}\right)^2 \frac{\pi^2}{3} = 2.44 \times 10^{-8}\, W\Omega K^{-2}$ is the Lorentz number.

From Equation (5.6), it is clear that the Seebeck coefficient is proportional to the slope of the natural logarithm of the transmission coefficient at the Fermi level. Consequently, S is enhanced by increasing the slope of $lnT(E)$ near $E = E_F$. The sign of S can be positive or negative, depending on the sign of the slope of the transmission function at the Fermi energy E_F. In other words, it is related to the nature of the charge carriers: S is positive for hole-dominated transport and negative for electron-dominated transport[13,14]. Therefore, measurements of the Seebeck coefficient of molecular junctions (MJs) are of great importance in determining the dominant transport mechanism and the location of frontier molecular orbitals in MJs[15–17].

To calculate the Seebeck coefficient for six OPE-based molecules, whose structures are shown in Fig. 4.4, I used DFT combined with the quantum transport code Gollum. In what follows, I will study the Seebeck coefficient of the studied molecules **1-6**, through an asymmetric junction (i.e., SLG and Au) with two different structures of Au (flat and cluster).

5.3 Au-flat surface

As discussed above, the slope of the transmission coefficient $T(E)$ determines the sign and magnitude of the Seebeck coefficient S. In other words, whether the curve is HOMO or LUMO

dominated. Fig. 5.1 shows Seebeck coefficient S (thermopower) over a range of Fermi energies at room temperature for molecules **1**, which is positive at DFT-predicted Fermi $E\text{-}E_F^{DFT}$=0 eV, and this is due to the fact that this molecule is a HOMO-dominated (see Fig. 4.32).

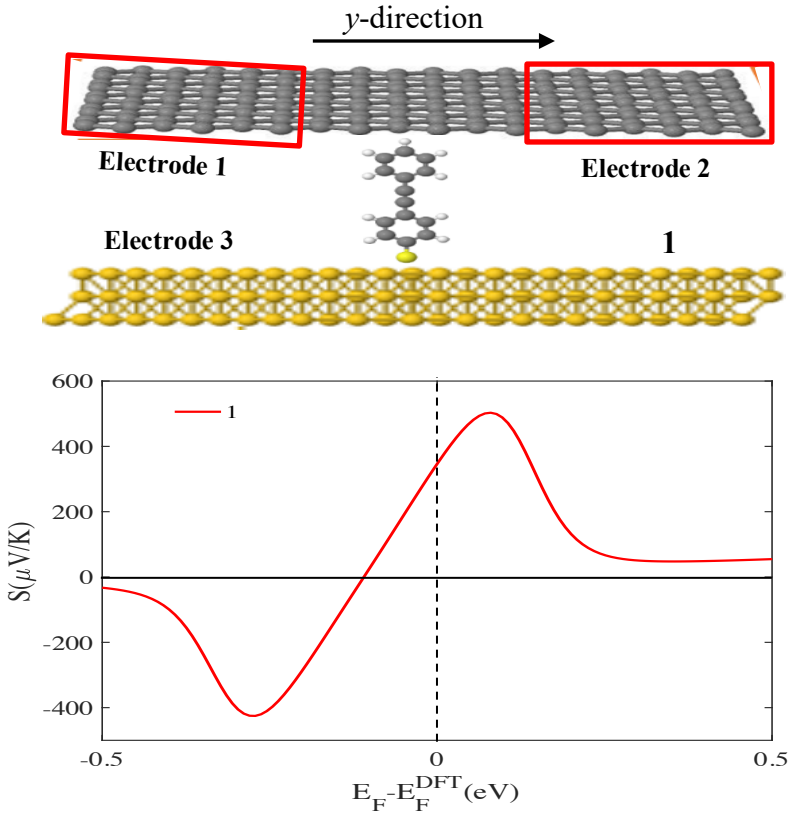

Fig. 5.1: Top panel: Schematic illustration of a three-terminal Au/**1**/SLG junction. The top contact is SLG, whereas the bottom contact is a flat Au. Bottom panel: the room-temperature Seebeck over a range of Fermi energies E_F relative to the DFT-predicted Fermi energy E^{DFT} for molecule **1**.

For molecule **2**, since this molecule has two junctions **2a** and **2b** (resulting from an inverting of molecule **2**) and possess HOMO dominated transmission curves as shown in Fig. 4.33, the Seebeck coefficients are positive at the DFT-predicted Fermi energy ($E\text{-}E_F^{DFT}= 0$ eV), as shown in Fig. 5.2.

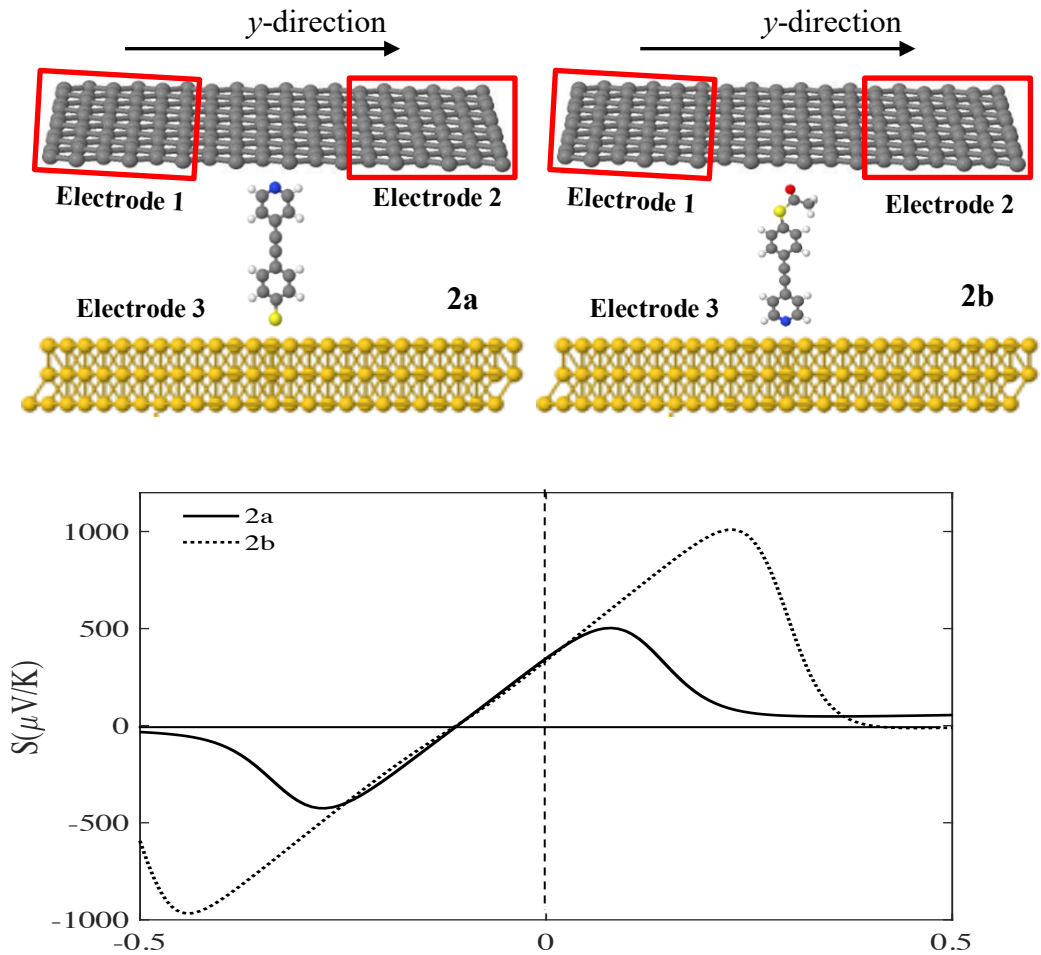

Fig. 5.2: Top panel: Schematic illustration of a three-terminal Au/**2a** or **2b**/SLG junction. The top contact is SLG, whereas the bottom contact is a flat Au. Bottom panel: the room-temperature Seebeck over a range of Fermi energies E_F relative to the DFT-predicted Fermi energy E^{DFT} for molecule **2**.

Similarly, as the HOMO resonances are closer to the DFT-predicted Fermi energy (E-E_F^{DFT}=0 eV) for junctions **3a** and **3b** (resulting from an inverting molecule **3**), as shown in Fig. 4.34, the Seebeck coefficients are positive in the vicinity of the DFT-predicted Fermi energy as shown in Fig. 5.3.

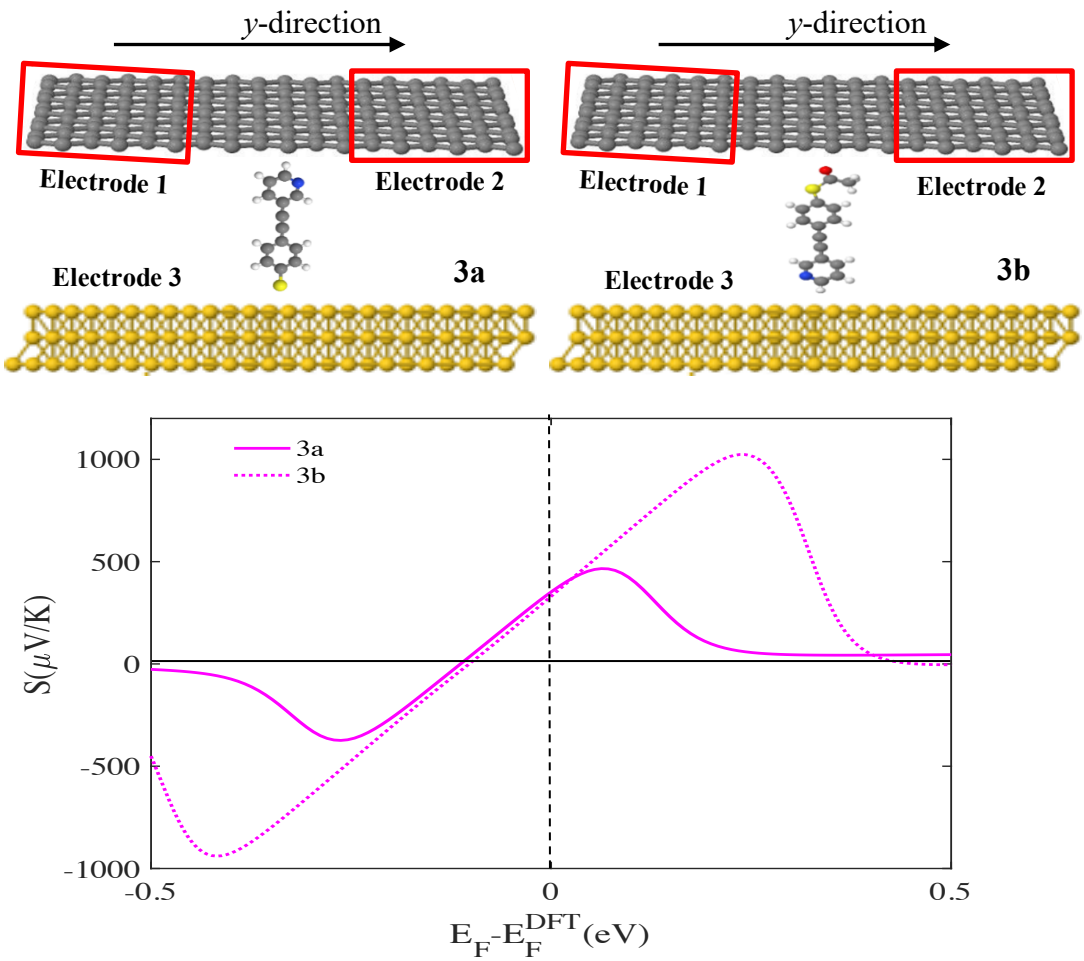

Fig. 5.3: Top panel: Schematic illustration of a three-terminal Au/**3a** or **3b**/SLG junction. The top contact is SLG, whereas the bottom contact is a flat Au. Bottom panel: the room-temperature Seebeck over a range of Fermi energies E_F relative to the DFT-predicted Fermi energy E^{DFT} for molecule **3**.

Again, molecule **4** is a HOMO-dominated due to the presence of thiol and thioacetate anchors, (see Fig. 4.35), which suggests that the Seebeck coefficient at the DFT-predicted Fermi energy ($E-E_F^{DFT}=0$ eV) is positive, as shown in Fig. 5.4.

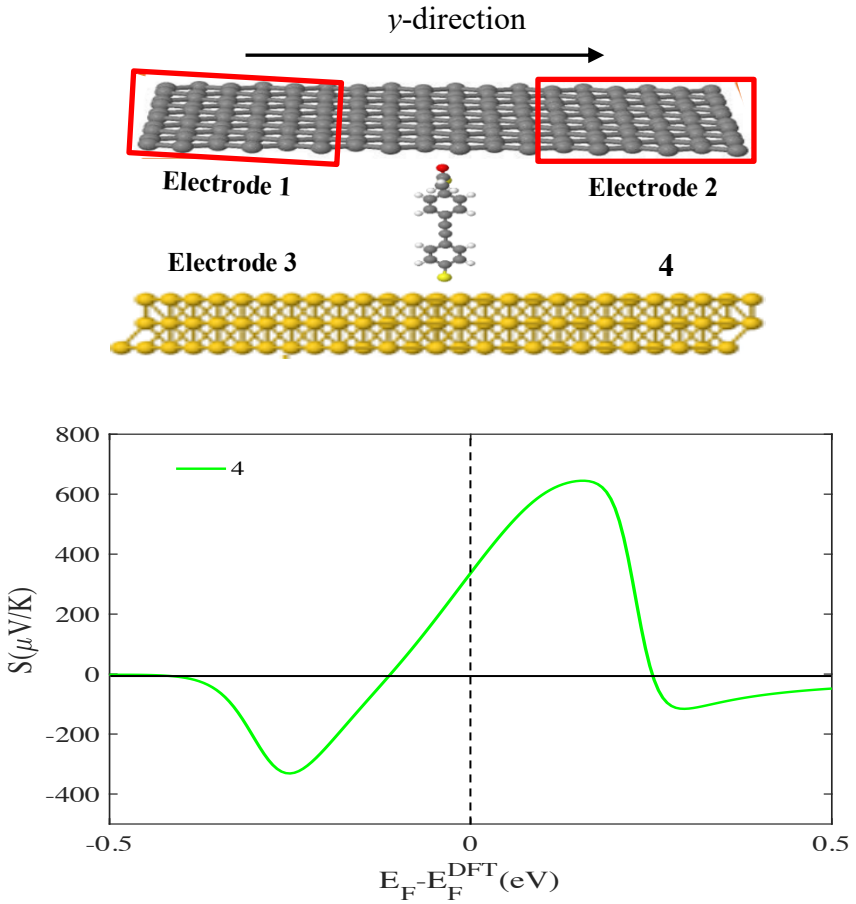

Fig. 5. 4: Top panel: Schematic illustration of a three-terminal Au/**4**/SLG junction. The top contact is SLG, whereas the bottom contact is a flat Au. Bottom panel: the room-temperature Seebeck over a range of Fermi energies E_F relative to the DFT-predicted Fermi energy E^{DFT} for molecule **4**.

Molecule **5,** which contains an additional PE repeat unit compared to molecule **4**, also has a HOMO-dominated transport (see Fig. 4.36)**,** leading to a positive Seebeck coefficient around the DFT-predicted Fermi energy as shown in Fig. 5.5.

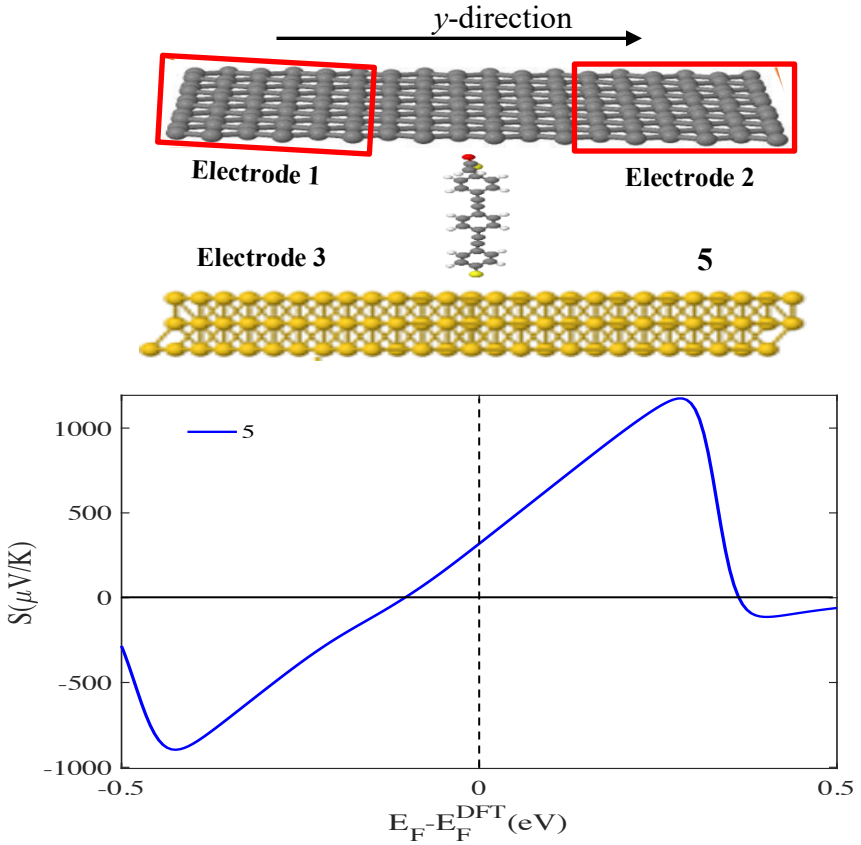

Fig. 5.5: Top panel: Schematic illustration of a three-terminal Au/**5**/SLG junction. The top contact is SLG, whereas the bottom contact is a flat Au. Bottom panel: the room-temperature Seebeck over a range of Fermi energies E_F relative to the DFT-predicted Fermi energy E^{DFT} for molecule **5.**

As discussed in chapter 4, molecule **6** is a LUMO dominated due to the presence of the four SMe and Py anchors, and since the sign of the Seebeck coefficient is determined by the slope of the transmission coefficient near the Fermi energy, the switching of the transport from HOMO to LUMO-dominated, as we move from **1-5** to **6**, causes a change in the sign of Seebeck coefficient (positive to negative) as shown in Fig. 5.6.

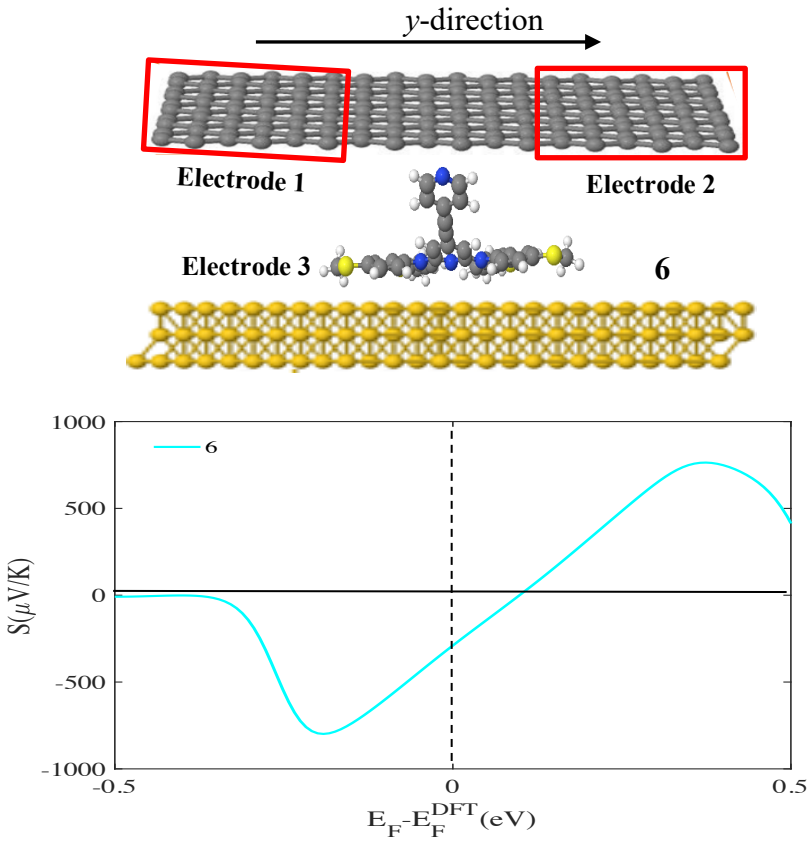

Fig. 5.6: Top panel: Schematic illustration of a three-terminal Au/**6**/SLG junction. The top contact is SLG, whereas the bottom contact is a flat Au. Bottom panel: the room-temperature Seebeck over a range of Fermi energies E_F relative to the DFT-predicted Fermi energy E^{DFT} for molecule **6.**

As discussed earlier in this chapter, the Seebeck coefficient for molecules **1-5** is found to be positive at DFT-predicted Fermi $E\text{-}E_F^{DFT}$=0 eV as shown in Fig. 5.7-a, due to the fact that these molecules are HOMO-dominated. In contrast, Fig. 5.7-b proves the Seebeck coefficient is negative at $E\text{-}E_F^{DFT}$=0 eV for molecule **6**, because it is a LUMO-dominated molecule.

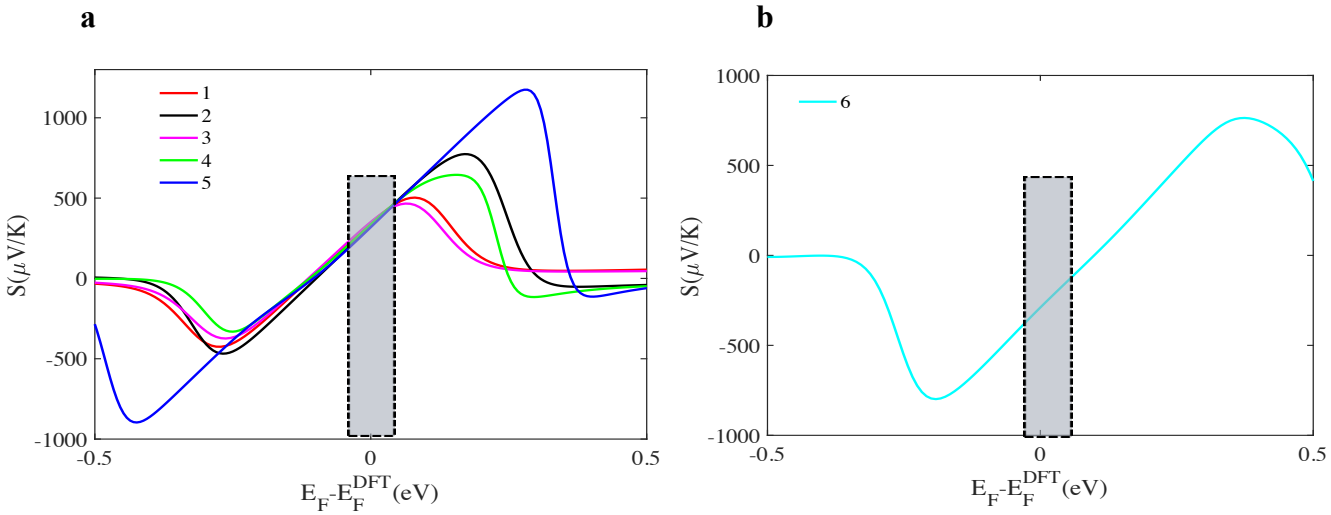

Fig. 5.7: **a:** Room-temperature Seebeck coefficients over a range of Fermi energies E_F relative to the DFT-predicted Fermi energy E^{DFT} of molecules **1-5**. A positive Seebeck coefficient is obtained at the DFT-predicted Fermi energy. **b:** Room-temperature Seebeck coefficient over a range of Fermi energies E_F relative to the DFT-predicted Fermi energy E^{DFT} of molecule **6**. A negative Seebeck coefficient is obtained at the DFT-predicted Fermi energy. (Note: Simulations here for a flat Au surface).

Table 5.1 shows the Seebeck coefficient values at DFT-predicted Fermi E-E_F^{DFT}= 0 eV for the six molecules which are positive and similar in the range between 318 and 346 $\mu V/K$ for **1**-**5**, while being negative, approximately $-157.8\ \mu V/K$, for molecule **6**.

Table 5. 1: Seebeck coefficient S at DFT-predicted Fermi E-E_F^{DFT}=0 eV for molecules **1**-**6**, which are bond to the flat Au and SLG.

Compound	$S\ (\mu V/K)$
1	+ 346.3
2	+ 331.3
3	+ 341.1
4	+ 336.9
5	+ 318.6
6	-157.8

5.4 Au-cluster

As it discussed in section 4.9.2, the shape of the Au electrode can affect the alignment of the HOMO and LUMO levels of the junction with respect to the Fermi level of the electrodes (i.e, molecules **2** and **3**), and since the sign of the Seebeck coefficient is dependent upon the position of the molecular energy levels (i.e., HOMO and LUMO) with respect to the Fermi level, the above Seebeck coefficient calculations were repeated, in which the molecules are bound to a gold atomic cluster rather than a flat Au substrate (see Figs. 5.8-5.13). As noted previously, molecule **1** remains HOMO-dominated after changing the shape of Au, in other words, molecule **1** is insensitive to the shape of the Au electrode, indicating that S remains positive at DFT-predicted Fermi, as shown in Fig. 5.8. In contrast, molecules **2** and **3** were found to be sensitive to the Au

shape. In other words, the Fermi level being closer to LUMO than to the HOMO (see Figs. 4.40, 4.41), leads to the switch of the sign of *S* from positive to negative at $E\text{-}E_F^{DFT}$=0 eV, as shown in Figs. 5.9 and 5.10. For molecules **4** and **5**, the transport remains HOMO-dominated (see Figs. 4.42, 4.43), which means the sign of *S* remains positive at $E\text{-}E_F^{DFT}$=0 eV, as shown in Figs. 5.11 and 5.12. Similarly, molecule **6** keeps unchanged in the two structures of Au (LUMO-dominated), meaning *S* is negative as shown in Fig. 4.13.

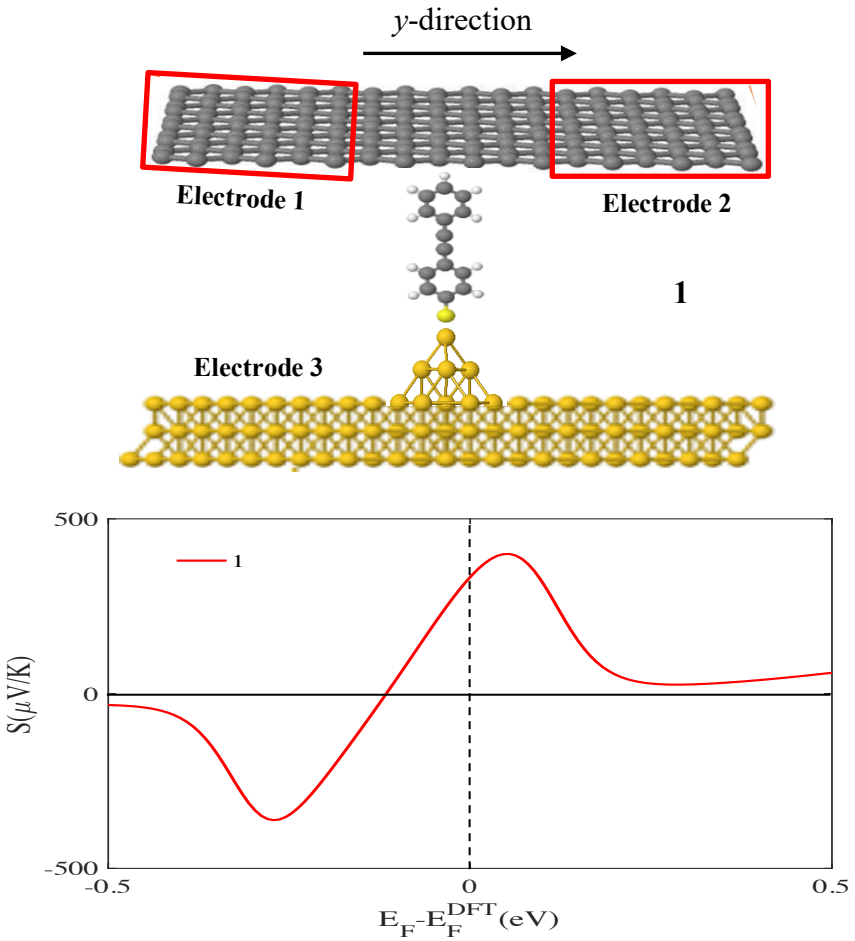

Fig. 5. 8: Top panel: Schematic illustration of a three-terminal Au/**1**/SLG junction. The top contact is SLG, whereas the bottom contact is an add-atom Au. Bottom panel: Room-temperature Seebeck over a range of Fermi energies E_F relative to the DFT-predicted Fermi energy E^{DFT} for molecule **1**

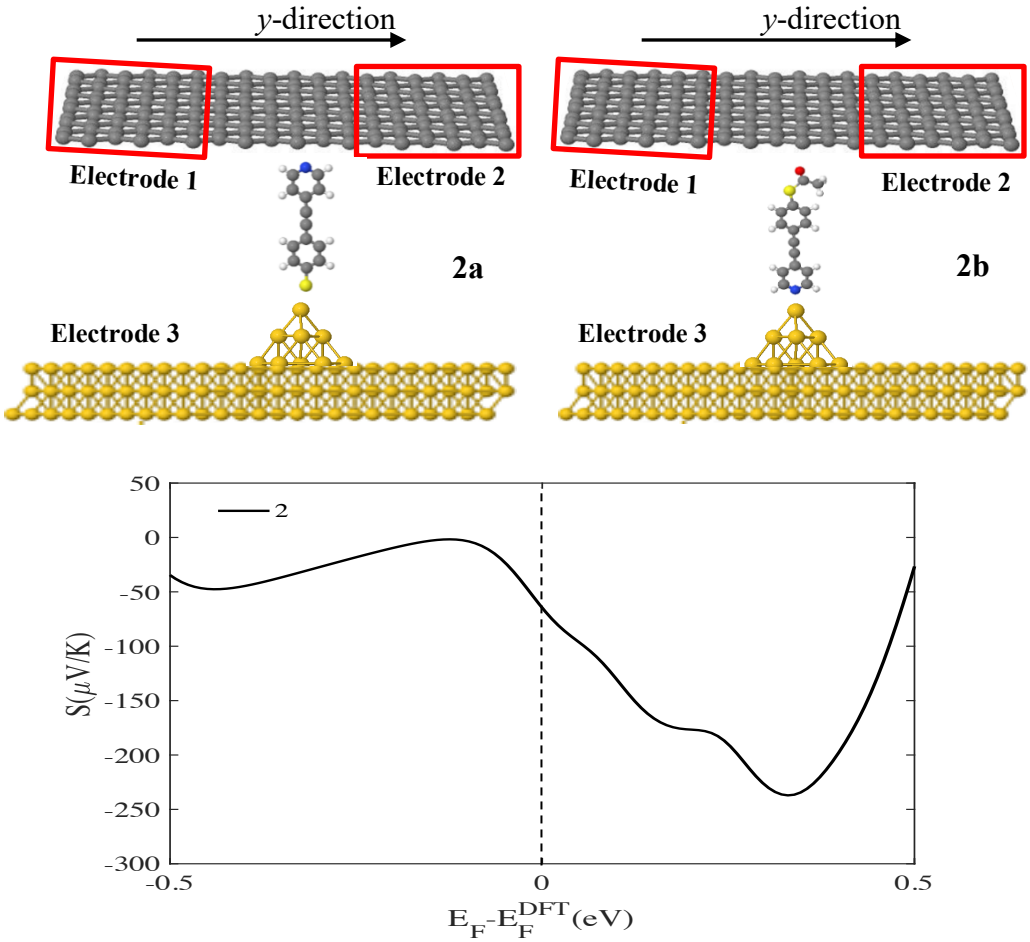

Fig. 5. 9 : Top panel: Schematic illustration of a three-terminal Au/**2**/SLG junction. The top contact is SLG, whereas the bottom contact is an add-atom Au. Bottom panel: the average room-temperature Seebeck over a range of Fermi energies E_F relative to the DFT-predicted Fermi energy E^{DFT} for molecule **2**.

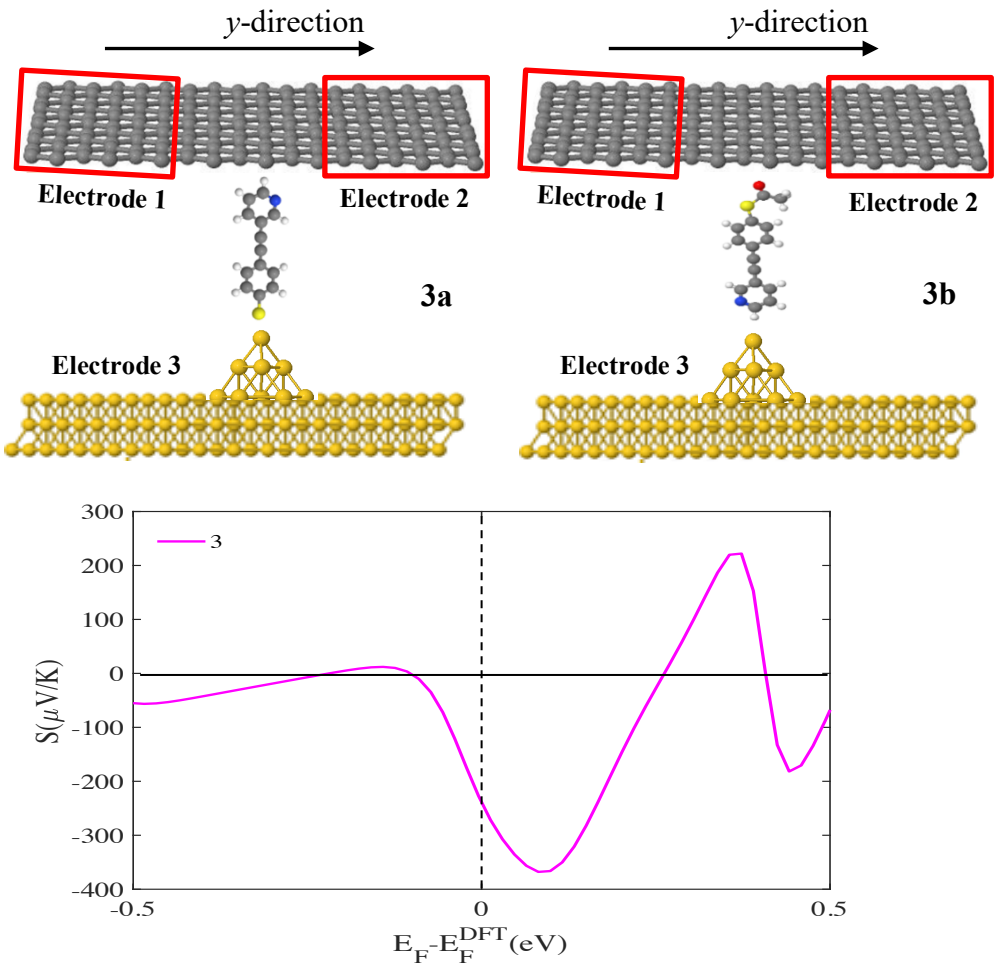

Fig. 5.10: Top panel: Schematic illustration of a three-terminal Au/**3**/SLG junction. The top contact is SLG, whereas the bottom contact is an add-atom Au. Bottom panel: the average room-temperature Seebeck over a range of Fermi energies E_F relative to the DFT-predicted Fermi energy E^{DFT} for molecule **3**.

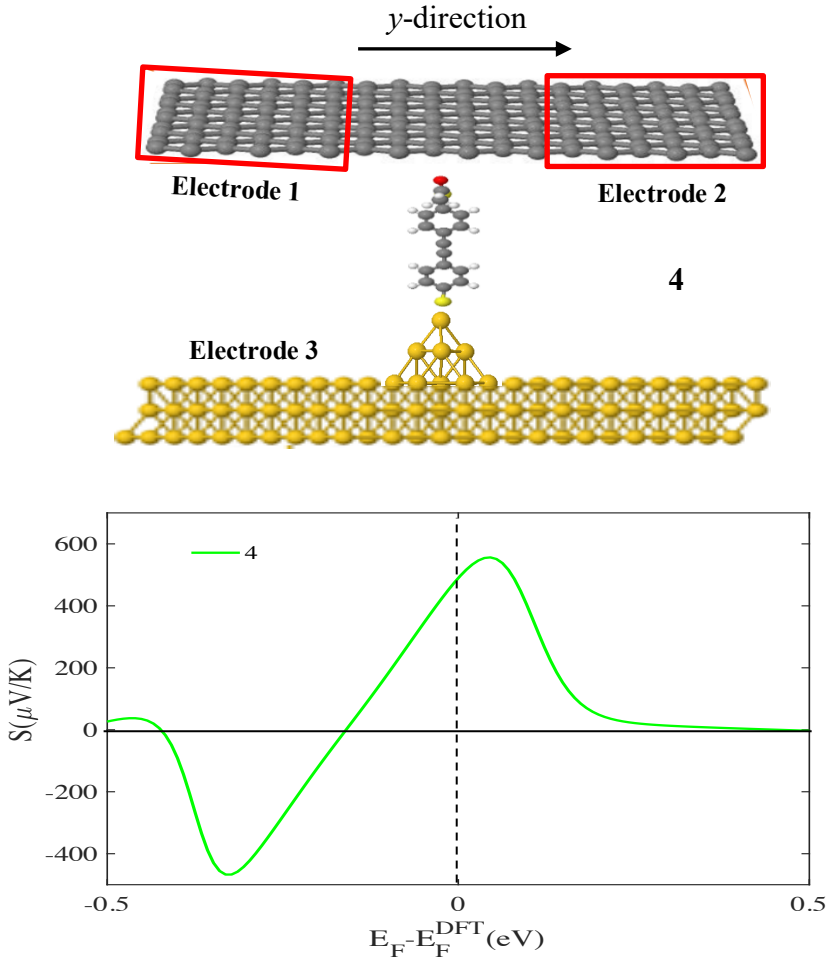

Fig. 5.11: Top panel: Schematic illustration of a three-terminal Au/**4**/SLG junction. The top contact is SLG, whereas the bottom contact is an add-atom Au. Bottom panel: Room-temperature Seebeck over a range of Fermi energies E_F relative to the DFT-predicted Fermi energy E^{DFT} for molecule **4**.

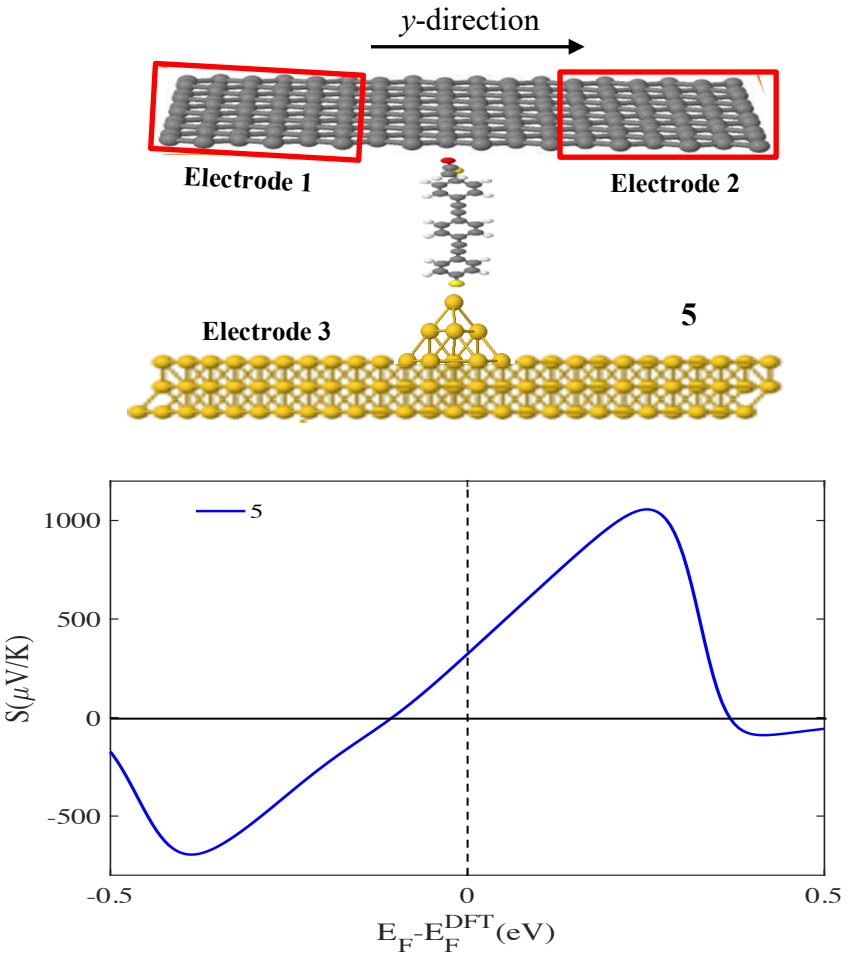

Fig. 5.12: Top panel: Schematic illustration of a three-terminal Au/**5**/SLG junction. The top contact is SLG, whereas the bottom contact is an add-atom Au. Bottom panel: Room-temperature Seebeck over a range of Fermi energies E_F relative to the DFT-predicted Fermi energy E^{DFT} for molecule **5**.

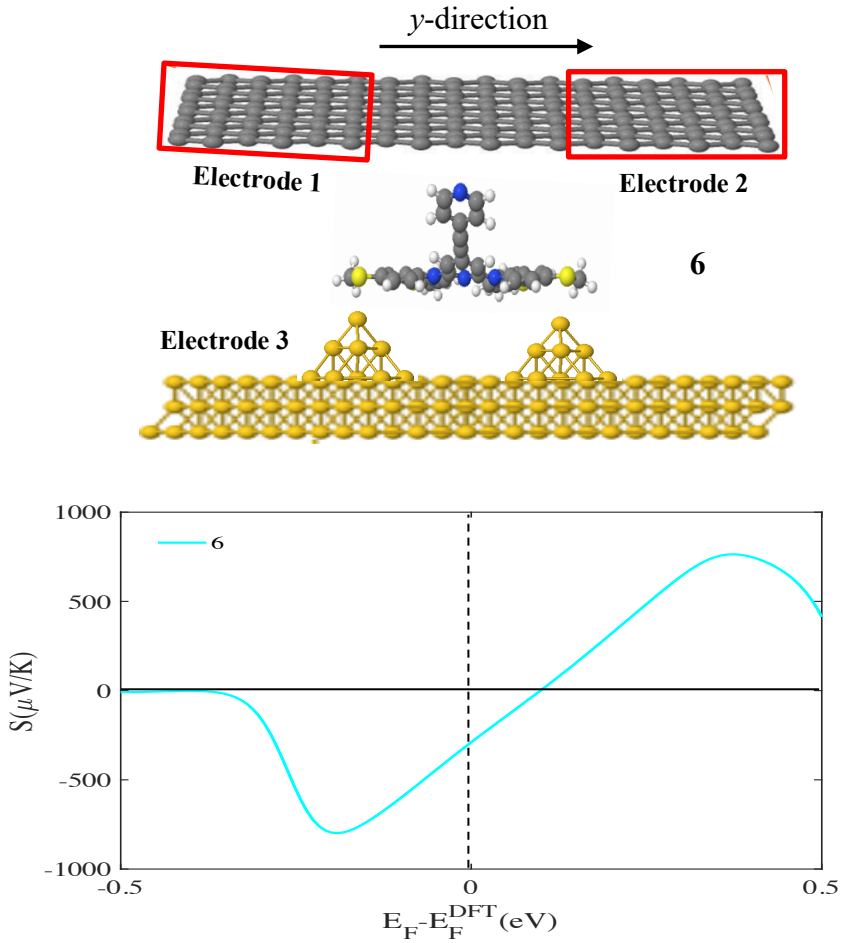

Fig. 5.13: Top panel: Schematic illustration of a three-terminal Au/**6**/SLG junction. The top contact is SLG, whereas the bottom contact is an add-atom Au. Bottom panel: Room-temperature Seebeck over a range of Fermi energies E_F relative to the DFT-predicted Fermi energy E^{DFT} for molecule **6**.

The above *S* calculations are summarized in Figs. 5.14-a and -b, which illustrate that the Seebeck coefficient is positive at the DFT-predict Fermi energy ($E-E_F^{DFT}=0$ eV) for molecules **1**,**4** and **5** owing to the fact that the transport takes place through the HOMO. Whereas molecules **2**, **3** and **6**

have a negative S and this suggests that the sign of Seebeck coefficients switched from positive to negative for molecules **2** and **3** by changing the shape of Au from flat to a cluster due to their switching from HOMO to LUMO dominated transport.

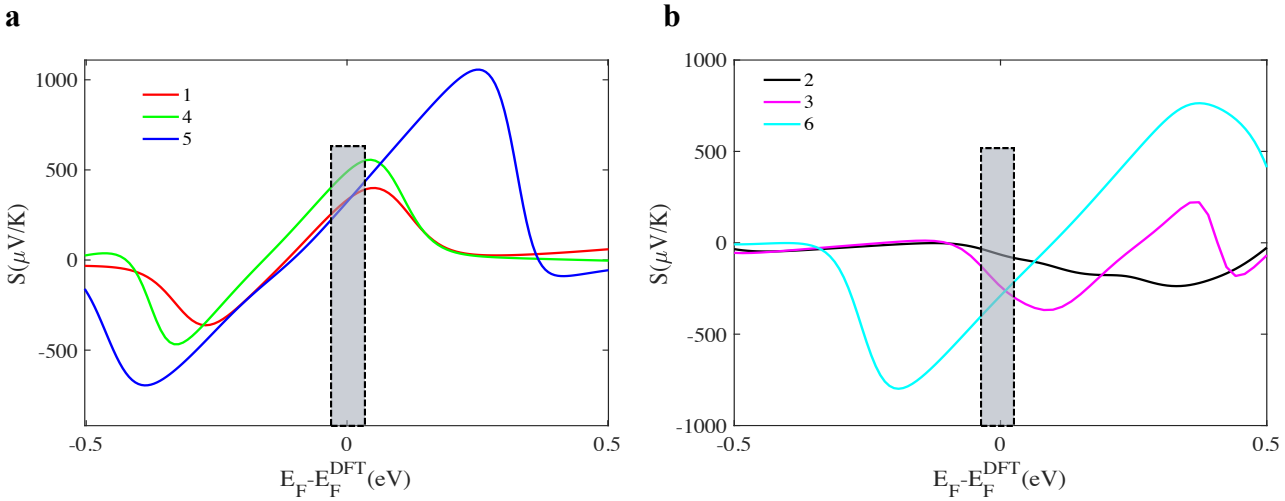

Fig. 5.14: **a:** Room-temperature Seebeck over a range of Fermi energies E_F relative to the DFT-predicted Fermi energy E^{DFT} of molecules **1, 4** and **5**. A positive Seebeck coefficient is obtained at the DFT-predicted Fermi energy. **b:** Room-temperature Seebeck over a range of Fermi energies E_F relative to the DFT-predicted Fermi energy E^{DFT} of molecules **2**, **3** and **6**. A negative Seebeck coefficient is obtained at the DFT-predicted Fermi energy. (Note: Simulations here for Au cluster).

Table 5.2 shows the Seebeck coefficient values at DFT-predicted Fermi $E\text{-}E_F^{DFT}$=0 eV for **1-6** molecules. As previously mentioned, the sign of S switched from positive to negative for molecules **2** and **3**, -64.7 and -238.5 $\mu V/K$ respectively.

Table 5. 2: Seebeck coefficient S at DFT-predicted Fermi E-E_F^{DFT}=0 eV for molecules **1-6**, which are bond to Au cluster and SLG.

Compound	$S\ (\mu V/K)$
1	+ 333
2	-64.7
3	-238.5
4	+489.5
5	+ 322
6	-289.5

As a comparison of Seebeck coefficients S, at the DFT-predicted Fermi E-E_F^{DFT}=0 eV, between flat Au and cluster for molecules **1-6,** table 5.3 shows the Seebeck coefficients transform from positive to negative for molecules **2 (**~ + 331.3 to - 64.7 $\mu V/K$) and **3 (**~ + 341.1 to -238.5 $\mu V/K$) by changing the shape of Au from a flat to cluster, while the sign of S does not change for the rest of molecules, and the magnitude of S is similar for molecules **1** and **5**, with significant improving for molecules **4 (**~ + 336.9 to +489.5 $\mu V/K$) and **6 (**~ -157.8 to -289.5 $\mu V/K$).

Table 5. 3: Comparison of Seebeck coefficients S between Au-flat and cluster at DFT-predicted Fermi E-E_F^{DFT}=0 eV for molecules **1**-**6**

	$S\ (\mu V/K)$	
Compound	**Au-flat**	**Au-cluster**
1	+ 346.3	+ 333
2	+ 331.3	-64.7
3	+ 341.1	-238.5
4	+ 336.9	+489.5
5	+ 318.6	+ 322
6	-157.8	-289.5

5.5 Conclusion

In summary, the room-temperature Seebeck coefficients of six OPE-based molecules have been investigated using two different shapes of Au electrode: flat and cluster. The results indicate that the Seebeck coefficient is positive for molecules **1-5** and negative for molecule **6** when the molecules are trapped between flat Au and SLG, and by changing the shape of Au from flat to cluster, the Seebeck coefficient is switched from positive to negative for molecules **2** and **3**. In other words, the relative position of E_F for molecules **2** and **3** can be determined by the shape of the gold surface, if it is flat or a gold cluster.

5.6 Bibliography

(1) Chen, H.; Sangtarash, S.; Li, G.; Gantenbein, M.; Cao, W.; Alqorashi, A.; Liu, J.; Zhang, C.; Zhang, Y.; Chen, L.; Chen, Y.; Olsen, G.; Sadeghi, H.; Bryce, M. R.; Lambert, C. J.; Hong, W. Exploring the Thermoelectric Properties of Oligo(Phenylene-Ethynylene) Derivatives. *Nanoscale* **2020**, *12* (28), 15150–15156.

(2) Cui, L.; Miao, R.; Jiang, C.; Meyhofer, E.; Reddy, P. Perspective: Thermal and Thermoelectric Transport in Molecular Junctions. *J. Chem. Phys.* **2017**, *146* (9), 092201.

(3) Rincón-García, L.; Evangeli, C.; Rubio-Bollinger, G.; Agraït, N. Thermopower Measurements in Molecular Junctions. *Chem. Soc. Rev.* **2016**, *45* (15), 4285–4306.

(4) Tan, A.; Balachandran, J.; Sadat, S.; Gavini, V.; Dunietz, B. D.; Jang, S.-Y.; Reddy, P. Effect of Length and Contact Chemistry on the Electronic Structure and Thermoelectric Properties of Molecular Junctions. *J. Am. Chem. Soc.* **2011**, *133* (23), 8838–8841.

(5) Hüser, F.; Solomon, G. C. From Chemistry to Functionality: Trends for the Length Dependence of the Thermopower in Molecular Junctions. *J. Phys. Chem. C* **2015**, *119* (25), 14056–14062.

(6) Malen, J. A.; Doak, P.; Baheti, K.; Tilley, T. D.; Segalman, R. A.; Majumdar, A. Identifying the Length Dependence of Orbital Alignment and Contact Coupling in Molecular Heterojunctions. *Nano Lett.* **2009**, *9* (3), 1164–1169.

(7) Akbarabadi, S. R.; Soleimani, H. R.; Tagani, M. B.; Golsanamlou, Z. Impact of Coupling Geometry on Thermoelectric Properties of Oligophenyl-Base Transistor. *Chin. Phys. B* **2017**, *26* (2), 027303.

(8) Golsanamlou, Z.; Tagani, M. B.; Soleimani, H. R. Thermoelectric Properties of Single Molecule Junction in Presence of Dephasing and Different Coupling Geometries. *Commun. Theor. Phys.* **2015**, *64* (3), 361–366.

(9) Ramezani Akbarabadi, S.; Rahimpour Soleimani, H.; Golsanamlou, Z.; Bagheri Tagani, M. Enhanced Thermoelectric Properties in Anthracene Molecular Device with Graphene Electrodes: The Role of Phononic Thermal Conductance. *Sci. Rep.* **2020**, *10* (1), 10922.

(10) Golsanamlou, Z.; Tagani, M. B.; Soleimani, H. R. Improvement of Thermoelectric Efficiency of the Polyaniline Molecular Junction by the Doping Process. *Phys. Chem. Chem. Phys.* **2015**, *17* (20), 13466–13471.

(11) Lambert, C. J. *Quantum Transport in Nanostructures and Molecules: An Introduction to Molecular Electronics*; IOP Publishing, 2021.

(12) Al-Galiby, Q. H.; Sadeghi, H.; Manrique, D. Z.; Lambert, C. J. Tuning the Seebeck Coefficient of Naphthalenediimide by Electrochemical Gating and Doping. *Nanoscale* **2017**, *9* (14), 4819–4825.

(13) Ismael, A. K.; Grace, I.; Lambert, C. J. Increasing the Thermopower of Crown-Ether-Bridged Anthraquinones. *Nanoscale* **2015**, *7* (41), 17338–17342.

(14) Alshammari, M.; Al-Jobory, A. A.; Alotaibi, T.; Lambert, C. J.; Ismael, A. Orientational Control of Molecular Scale Thermoelectricity. *Nanoscale Adv.* **2022**, *4* (21), 4635–4638.

(15) Sadeghi, H. Discriminating Seebeck Sensing of Molecules. *Phys. Chem. Chem. Phys.* **2019**, *21* (5), 2378–2381.

(16) Al-Khaykanee, M. K.; Ismael, A. K.; Grace, I.; Lambert, C. J. Oscillating Seebeck Coefficients in π-Stacked Molecular Junctions. *RSC Adv.* **2018**, *8* (44), 24711–24715.

(17) Widawsky, J. R.; Darancet, P.; Neaton, J. B.; Venkataraman, L. Simultaneous Determination of Conductance and Thermopower of Single Molecule Junctions. *Nano Lett.* **2012**, *12* (1), 354–358.

Chapter 6

6. Conclusion and Future Work

6.1 Conclusion

This thesis is composed of the following chapters:

Chapter 1 was a brief overview of molecular electronics and the thesis outlines.

Chapter 2 introduced general concepts of DFT and its implementation SIESTA code, which I have used in this thesis to calculate the electronic and thermoelectric properties of single-molecule junction.

Chapter 3 described the single particle theory based on the scattering theory and equilibrium Green's function, and relating topics such as Landauer formulism, with some examples of how to calculate the transmission coefficient for different systems using the Hamiltonian and Green's functions.

Chapter 4 presented the theoretical results of six oligo(phenylene-ethynylene) OPE-based molecules that were trapped between the single-layer graphene (SLG) and the gold electrode to form SLG/molecule/Au junction. I investigated six OPE-based molecules with different anchor groups including thiol, pyridine, thioether and thioacetate. To calculate the electronic and thermoelectric properties, I simulated a three-terminal junction, in which the top contact is single-layer graphene (SLG) and the bottom contact is gold to provide an asymmetric junction. The optimal binding distances between the contacts (i.e., Au and SLG) and the different anchor groups were obtained by calculating their binding energies as a function of distance, and the results reveal that thiol exhibits the strongest binding to the Au compared to the others due to its strong covalent bond. Regarding the surface material, calculations demonstrate that the studied anchors bind much

weakly to the Gr sheet than to Au due to their weak interactions with Gr (i.e., non-covalent bond). Furthermore, I also explored the electronic properties of six OPE-based molecules using two different shapes of Au electrode: flat and cluster. First, I studied the charge transport behaviour through a SLG/molecule/ Au-flat junction. I have shown the transmission coefficients for molecules **1-5** are dominated by a HOMO resonance in the vicinity of the DFT-predicted Fermi energy ($E\text{-}E_F^{DFT}$=0 eV). In contrast, the transmission through molecule **6** is dominated by a LUMO resonance (due to the presence of SMe and Py anchors). Secondly, I repeated the transmission function calculations, where the molecules were bound to a gold atomic cluster. The simulations suggest that molecules **1**, **4** and **5** remain HOMO-dominated at the DFT-predicted Fermi energy, whereas molecules **2**, **3** and **6** are a LUMO- dominated at the DFT-predicted Fermi energy. This hints that four molecules (i.e., **1**, **4**, **5** and **6**) are insensitive to the shape of the Au surface, whereas two are sensitive (i.e., **2** and **3**), due to their switching from HOMO to LUMO-dominated transport. In other words, the shape of the gold surface, whether it is flat or possesses a gold cluster at the molecule-gold contact, determines the relative position of E_F for molecules **2** and **3**.

Chapter 5 explored the thermoelectric properties of the studied molecules in chapter 4. The impact of the shape of the Au electrode (i.e., flat and cluster) on the sign of the Seebeck coefficient is also probed. With flat gold, the Seebeck coefficient is positive for molecules **1-5** and negative for molecule **6,** while it switches from positive to negative for molecules **2** and **3** by changing the gold electrode from flat to cluster.

6.2 Future Work

In this thesis I have investigated the electron transport of the self-assemble monolayer (SAMs) for the OPE- based molecules that trapped between the single-layer graphene (SLG) and the gold electrode to form SLG/molecule/Au junction. For the future, one can envisage extending this work in a number of directions. First it would be interesting to replace the asymmetry Au/molecule/graphene junction by symmetry such as graphene/molecule/graphene junction to explore how the results would change. One interesting study would be an assessment of transport properties when OPE-based molecules are terminated by other anchor groups such as amine (NH2), cyano (CN) and BDT. It would also be of interest to investigate the electronic properties of different molecules such as fullerene C_{60}[1] and porphyrin [2]. Recently, phonon transport properties in three-terminal systems have drawn increasing attention due to the potential applications in thermal devices[3]. Therefore, it would be worth to utilise methods for computing phonon transport through three-terminal system to obtain the contribution from phonon to thermal conductance. Another interesting aspect is utilizing alternative electrode material, including superconducting and semiconductor electrodes[4,5]. In addition, hybrid superconductor-semiconductor nanowire structures have recently become a topic of intense interest[6]. They have opened new research avenues in quantum transport, that may lead to new quantum effects. Finally, the spin transport in the presence of three ferromagnetic electrodes[7], as well as a combination of superconducting and ferromagnetic electrodes, may be worthy of investigation.

6.3 Bibliography

(1) Danilov, A. V.; Kubatkin, S. E.; Kafanov, S. G.; Bjørnholm, T. Strong Electronic Coupling between Single C $_{60}$ Molecules and Gold Electrodes Prepared by Quench Condensation at 4 K. A Single Molecule Three Terminal Device Study. *Faraday Discuss* **2006**, *131*, 337–345.

(2) Wu, Q.; Hou, S.; Sadeghi, H.; Lambert, C. J. A Single-Molecule Porphyrin-Based Switch for Graphene Nano-Gaps. *Nanoscale* **2018**, *10* (14), 6524–6530.

(3) Zhang, L.; Wang, J.-S.; Li, B. Ballistic Thermal Rectification in Nanoscale Three-Terminal Junctions. *Phys. Rev. B* **2010**, *81* (10), 100301.

(4) McCaughan, A. N.; Berggren, K. K. A Superconducting-Nanowire Three-Terminal Electrothermal Device. *Nano Lett.* **2014**, *14* (10), 5748–5753.

(5) Pepe, G. P.; Scaldaferri, R.; Parlato, L.; Peluso, G.; Granata, C.; Russo, M.; Rotoli, G.; Booth, N. E. Low- T_c Three-Terminal Structures for New Superconducting Devices. *Supercond. Sci. Technol.* **2001**, *14* (12), 987–993.

(6) Ménard, G. C.; Anselmetti, G. L. R.; Martinez, E. A.; Puglia, D.; Malinowski, F. K.; Lee, J. S.; Choi, S.; Pendharkar, M.; Palmstrøm, C. J.; Flensberg, K.; Marcus, C. M.; Casparis, L.; Higginbotham, A. P. Conductance-Matrix Symmetries of a Three-Terminal Hybrid Device. *Phys. Rev. Lett.* **2020**, *124* (3), 036802.

(7) Yue, Z.; Prestgard, M. C.; Tiwari, A.; Raikh, M. E. Resonant Magnetotunneling between Normal and Ferromagnetic Electrodes in Relation to the Three-Terminal Spin Transport. *Phys. Rev. B* **2015**, *91* (19), 195316.